AN ABSTRACT OF THE THESIS OF

Dennis F. Petersen for the degree of Master of Science in Chemical Engineering presented on March 3, 2016.

Title: Density Functional Theory Investigation of CH Coupling and CH Hydrogenation Reactions on Different Cobalt Surface Facets and Fischer-Tropsch Temperature Swing Reactor Optimization

Abstract approved: _____

Líney Árnadóttir

Abstract: Fischer-Tropsh Synthesis is a chemical process that converts CO and H_2 (syngas) into long stable hydrocarbon chains to use as fuel. This process suffers from large product distribution that requires expensive post processing. In this study, the reaction mechanism of hydrocarbon chain growth on Co is investigated on different surface facets of Co in order to study their effects on the rate-limiting reaction steps. Fischer-Tropsch is a complex multi-step process so a microkinetic model for the carbide chain growth mechanism, available literature data, and the degree of rate control analysis was used to determine the rate-limiting steps for hydrocarbon chain production, CO utilization, and minimization of CH_4 production. The CH-CH carbon coupling and CH hydrogenation were determined to be the critical steps in chain growth, CH_4 formation, and CO utilization based on the degree of rate control analysis of the microkinetic model. Density Functional Theory (DFT) was used to investigate these reaction steps on cobalt catalyst to understand how different surface facets affect these reaction steps. The calculated energy landscape, reaction and activation energies for the two reaction paths are initially compared on two different Co facets ((001) and (110)) and used to determine the most effective surface structure for CH-CH carbon coupling, which leads to chain growth, and the least effective surface structure for CH hydrogenation, which leads to CH_4 formation. Other surface facets under investigation include (111) and (101). The forward activation barrier for the CH coupling reaction showed little sensitivity to cobalt surface structure ($\Delta E_{001,F} = 1.01$ eV, $\Delta E_{110,F} = 1.08$ eV) as opposed to the CH hydrogenation reaction where forward activation barriers ranged between 0.29 eV and 0.96 eV on the (001) and (101) facets respectively. This study is a part of a larger initiative to design and

optimize a FTS micro-reactor for commercial use which combines atomistic DFT calculations, multiphysics modeling (mass, heat and fluid transport), experimental catalyst design, and micro-reactor design.

Density Functional Theory Investigation of CH Coupling and CH Hydrogenation Reactions on Different Cobalt Surface Facets and Fischer-Tropsch Temperature Swing Reactor Optimization

by

Dennis F. Petersen

A THESIS

submitted to

Oregon State University

in partial fulfillment of
the requirements for the
degree of

Master of Science

Presented March 3, 2016
Commencement June 2016

Master of Science thesis of <u>Dennis F. Petersen</u> presented on <u>March 3, 2016</u>

APPROVED:

_____

Major Professor, representing Chemical Engineering

_____

Head of the School of Chemical, Biological, and Environmental Engineering

_____

Dean of the Graduate School

I understand that my thesis will become part of the permanent collection of Oregon State University libraries. My signature below authorizes release of my thesis to any reader upon request.

_____

Dennis F. Petersen, Author

ACKNOWLEDGEMENTS

TABLE OF CONTENTS

TABLE OF CONTENTS (Continued)

LIST OF FIGURES

LIST OF FIGURES (Continued)

LIST OF FIGURES (Continued)

LIST OF TABLES

LIST OF SYMBOLS

Symbol	Units	Property
*	-	catalyst active site
(001)	-	miller plane identification (hcp lattice)
α	-	chain growth probability
θ (theta)	-	catalyst active site
τ	1/hr	gas hourly space velocity
A*	-	species "A" adsorbed on catalyst active site
C	-	carbon atom
C_{x+}	-	hydrocarbon species with x number of carbons
E_{ads}	eV	adsorption energy
H	-	hydrogen atom
k_b	eV/K	Boltzmann Constant
$k_{f,r}$	1/sec or 1/bar*sec	forward (k_f) and reverse (k_r) reaction rate constants
n	carbon atoms	number of carbons in a hydrocarbon chain
N_A	molecules/mol	Avogadro's number
O	-	oxygen atom
P_A	bar	partial pressure of species A
R	-	hydrocarbon species of variable chain length
r_A	mol/sec	reaction rate of species A
RT	bar*L/mol	Ideal Gas Constant multiplied by Temperature
V_r	L	reactor volume
W_n	-	weight percentage carbon

1. Introduction

Since the beginning of the Industrial Revolution, humankind has used fossil fuels as a primary power source for machinery of all purposes. Having entered the 21st century, our dependence on fossil fuel in the form of coal and oil has continued at a steady pace. While many green technologies are currently available, they are still unable to compete with the energy density, transportability, and accessibility of fossil fuels. These qualities have allowed humankind to become greatly dependent on fossil fuel over the last century with the advantage of greatly boosting our productivity and mobility. Although humankind has greatly prospered from these fuels, the environment has begun to suffer from the byproducts of their usage. Carbon release into the atmosphere from burning natural gas, coal, and oil has been contributing to the warming of our global climate. Until mankind completely switches from fossil fuel to renewable green energy, we will continue to release carbon into the atmosphere at an unnatural rate.

While the ultimate goal of completely replacing fossil fuel with green renewable energy is being worked on, another way to combat excessive carbon release from fossil fuel is to minimize the amount of carbon release from current fuels. This can be done by increasing the efficiency of machinery that burns fossil fuels or capturing the carbon before it is released into the atmosphere. An issue that is currently plaguing the petroleum industry is the release of natural gas from remote oil wells. Due to the great distances between the wells and their parent refineries, capture and transportation of natural gas in a cryogenic state is extremely expensive and overrides the value of the gas produced. Natural gas is primarily composed of methane which is an extremely potent greenhouse gas. The current method for combatting the release of methane into the atmosphere is burning or "flaring" to produce a less harmful greenhouse gas known as carbon dioxide.

Other than shutting down an oil well that is flaring natural gas, an alternative measure is to transform released gas into a stable liquid compound that greatly reduces the cost of transportation. This gives petroleum companies incentive to harvest the natural gas as opposed to flaring it. Since World War II, a process that involves steam reforming of natural gas into carbon monoxide and hydrogen with the subsequent chain growing reactions of those reactants into stable hydrocarbon fuel has been heavily researched and utilized. The latter part of this process is known as Fischer-Tropsch Synthesis (FTS).

Even though FTS has been heavily researched and utilized at large petroleum processing refineries, the incentive to utilize this process at remote locations has been hindered by the size and subsequent capital costs and cost of operation. The feasibility of utilizing this process at remote well sites depends heavily on the mobility, size, efficiency, and maintenance of the FTS process. To design a compact FTS process that is still cost efficient, the efficiency of product output and conversion of natural gas must be greatly increased. Currently, the FT reaction generates many unwanted byproducts including light alkane gasses and heavy paraffin waxes. Extensive research over the last 100 years has been focused on reducing methane selectivity and narrowing the range of produced alkanes to specific compounds such as octane[5, 6]. Most of this research has involved the optimization of FT catalysts to achieve this goal[7].

FT catalyst research lies at the heart of most FT studies that have been performed in the last 100 years. Before the age of computers, large sums of money were invested in experimental catalyst research that involved parameter optimization of operation conditions and catalyst explorations. Early reaction modeling allowed for some insights to be gained into the complex FT reaction network but the presence of extremely unstable intermediate surface species made it extremely challenging to make progress in understanding the reaction mechanisms involved in FTS at the atomic level. Recent development of first principle quantum mechanics and computational analysis provided the means to probe the complex intermediate reactions of FTS.

Density Functional Theory (DFT) was developed as a means to simplify first principle investigations of molecular systems. It greatly reduced the computational time required to calculate the electronic structure of a given molecular system. DFT has been used extensively to investigate FTS from identifying primary reaction steps to studying the effect of catalyst at the molecular level. Even with a powerful tool like DFT, finding a catalyst with the perfect composition and structure that yields specific hydrocarbons of desired chain length has yet to be accomplished.

In this study, DFT is used to investigate the effect of catalyst surface structure on the chain producing rate-limiting reaction steps of FTS identified by a microkinetic model of the reaction mechanism at the flat terrace. Previous studies have shown that the surface structure of a catalyst can have a large impact on the reaction kinetics of FTS[8-10]. The purpose of this study is to observe the effect of low-index surface facets of hexagonal closed-packed (hcp) cobalt on FT chain growth

and methane formation. A facet ideal for catalyst optimization will hinder methane formation while simultaneously enhancing chain growth.

This is a part of a collaborative effort between industry and academia to move the FTS process onto a micro reactor platform. The team has built a test platform to test different catalyst and process operating conditions as well as designed catalyst deposition methods. Presented herein, is a combination of theoretical calculations and microkinetic modeling used to guide the experiments and catalyst synthesis. Two microkinetic models, based on previously published data, were used to determine an optimal process temperature range to optimize selectivity towards larger hydrocarbons and to determine desorption temperature and optimized on-catalyst residence time for a non-steady state temperature swing reactor design. A detailed microkinetic model combined with the method of degree of rate control was used to determine the critical steps of hydrocarbon growth which helps us concentrate our computational efforts.

Using the microkinetic models, we have found that 229 ^{o}C is the optimal temperature for promoting selectivity towards C_{2+} hydrocarbon chain production and identified the two rate-limiting reaction steps, CH* + CH* $\longleftrightarrow$ C_2H_2** and CH* + H* $\longleftrightarrow$ CH_2*, for C_{2+} chain production. Microkinetic modelling also served as a tool to identify an optimal temperature swing from 220°C to 450°C over 6.0 seconds for octane production in a temperature swing reactor. A thorough DFT investigation of the rate-limiting reaction steps on various low-index cobalt facets showed that CH* coupling was insensitive (0.3 eV forward activation barrier range) to the surface structure of cobalt in comparison to CH* hydrogenation which showed dramatic sensitivity (0.7 eV forward activation barrier range) to cobalt surface structure. Based on this observation, it is possible that the structural influence of cobalt catalyst on FT chain formation is induced not by the alteration of CH* coupling kinetics but the hindrance of CH* hydrogenation that potentially leads to methane formation. This will guide future developments of catalyst for more selective FTS processes by designing catalyst with an emphasis on hindering CH* hydrogenation.

1.1. Motivation

There are many sources that contribute to the current state of global carbon emission with vehicular exhaust and coal burning being a couple of the largest culprits. Another source, that is less known by the general public, is the carbon release from oil wells. Natural gas is released when oil is brought up to the surface during oil extraction. Current industrial practice is to capture this

natural gas and send it to the refinery when oil wells are within short distances of the refinery. This is not the case for remote wells, located far inland or out at sea, were it is not cost effective to captured natural gas due to the high price of on-site conversion to liquid natural gas (LNG) and volatile materials transportation. This solution not only wastes non-renewable natural gas but also contributes to global carbon emission. A good example of industrial methane flaring can be found in North Dakota where the Bakken Oil Fields are located (**Figure 1.1**). Over one billion dollars of natural gas was flared in 2012 at the Bakken Fields which is approximate to one million cars worth of CO_2 being released over a year[11]. This amount has been predicted to increase as the Bakkan oil fields reach peak production.
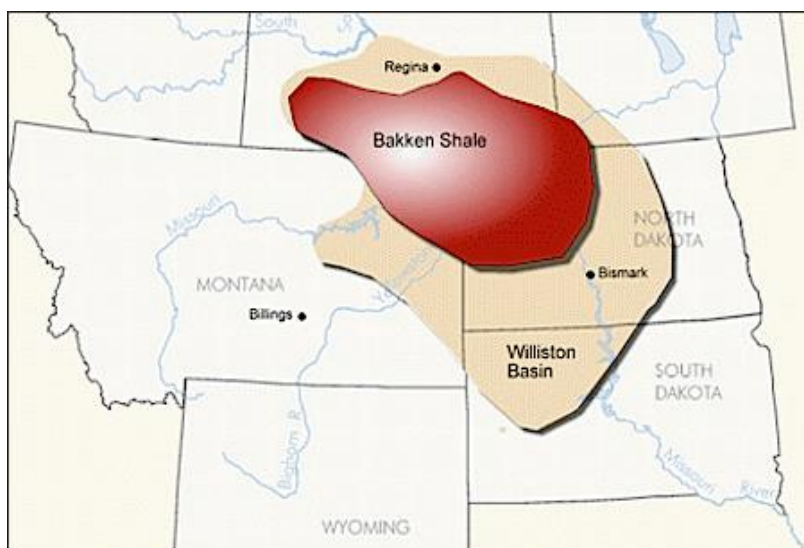
Figure 1.1. The Bakken oil fields extend from North Dakota into Montana and Canada. At night, the area is illuminated by thousands of drilling sites that makes the brightness of the area resemble that of a small city.[4]

One solution to add value to remote oil well natural gas and lower their CO_2 emissions is on-site conversion to stable liquid hydrocarbon fuel. By converting natural gas into liquid fuels, that are stable at transportation conditions, the cost of transportation can be dramatically decreased. This can be achieved by using "Gas to Liquid" technology. Gas to liquid technology has been heavily researched since the 1920's when FTS was first developed[12] by Franz Fischer and Hans Tropsch. They discovered that certain catalysts such as platinum, cobalt, and iron could convert carbon monoxide and hydrogen gas into paraffin and olefin hydrocarbon chains under specific reaction conditions. This process has been used for almost a century, in series with methane reforming, to convert natural gas into liquid hydrocarbon fuel. Even with a centuries worth of

research focused on this particular catalytic reaction, much effort is still being made in optimizing this reaction for higher selectivity towards desired hydrocarbon products and higher material utilization.

1.2. Fischer-Tropsch Synthesis

FTS is the catalytic formation of paraffin and olefin hydrocarbon species through the activation of adsorbed hydrogen and carbon monoxide gas (syngas). Other products of FTS include water, carbon dioxide, alcohols, aromatic carbons, and trace amounts of other oxygenated hydrocarbons. FTS can be broken down into six proposed steps[13, 14]: Reactant adsorption, hydrocarbon chain initiation, hydrocarbon chain propagation, hydrocarbon chain termination, product desorption, and readsorption of olefin products. The FT reaction starts with the adsorption of CO and H_2 gas on the surface of an active FT catalyst (Co, Fe, and Pt). CO has been proposed to dissociate either through direct dissociation[15] (equation 1.1) or hydrogen-assisted dissociation[16] (equations 1.2) and H_2 has been proposed go through quasi-equilibrated adsorption[17] (equation 1.3). Direct CO dissociation can be described with a single equation, however hydrogen-assisted CO dissociation involves a handful of possible pathways that leads to the formation of hydrocarbon chain monomers ($CH_{1-3}*$).

$$CO^* + {}^* \leftrightarrow C^* + O^* \tag{1.1}$$

$$CO^* + 2H^* \leftrightarrow HCOH^{**} \leftrightarrow CH^* + OH^* \tag{1.2}$$

$$H_{2(g)} + 2^* \leftrightarrow 2H^* \tag{1.3}$$

The second phase of FTS is the chain initiation phase where CH_x* monomers couple to form small ethane paraffins and olefins. The exact major route by which chain initiation occurs has been the subject of much debate [8, 18-26] and no consensus has been reached about the exact mechanism (equations 1.4 and equation 1.5)[15] by which it occurs.

$$CH_{x,(1-3)}{}^* + CH_{y,(1-3)}{}^* \leftrightarrow C_2H_{x+y}{}^* \quad (x + y \leq 6) \tag{1.4}$$

$$CH_{x,(1-3)}{}^* + CO^* \leftrightarrow C_2H_xO^* \quad (x < 4) \tag{1.5}$$
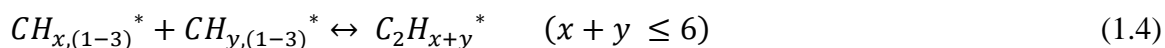
The final phase in the FT progression toward producing large hydrocarbon chains from adsorbed C_2 species involves the propagation and termination of these species on the catalyst surface. The propagation mechanism involves the addition of carbon monomers to growing C_{2+} hydrocarbon chains that further increase their chain length. There are currently two proposed mechanisms that describes this process by which hydrocarbon chains grow during the FT process: the carbide mechanism (equation 1.6)[5, 20] and the CO insertion mechanism (equation 1.7)[27].

$$RCH_{x,(1-3)}{}^* + CH_{y,(1-3)}{}^* \leftrightarrow RC_2H_{x+y}{}^* \qquad (x+y \le 6) \qquad (1.6)$$

$$RCH_x{}^* + CO^* \leftrightarrow RC_2H_xO^* \qquad (x < 4) \qquad (1.7)$$

A study by Chang et al.[1] showed the $RCH_2 + C$ and $RCH + CH_2$ coupling reactions to be dominant reaction pathways for FTS chain propagation on cobalt. These reaction pathways are further supported by Brady et al.[28] who analyzed three possible chain propagation mechanisms for FTS on Co surfaces. Of the three mechanisms investigated (Fischer-Tropsch mechanism, Anderson and Emmett mechanism, and Pichler and Schultz mechanism)[28] the Fischer-Tropsch Chain Propagation[29] was found to be the primary mechanism (**Figure 1.2**). Currently, there has been no conclusion reached on the primary mechanism for FT chain propagation. There is evidence to suggest that either the carbide or CO insertion mechanism plays the primary role in chain growth as shown in the previous studies mentioned.
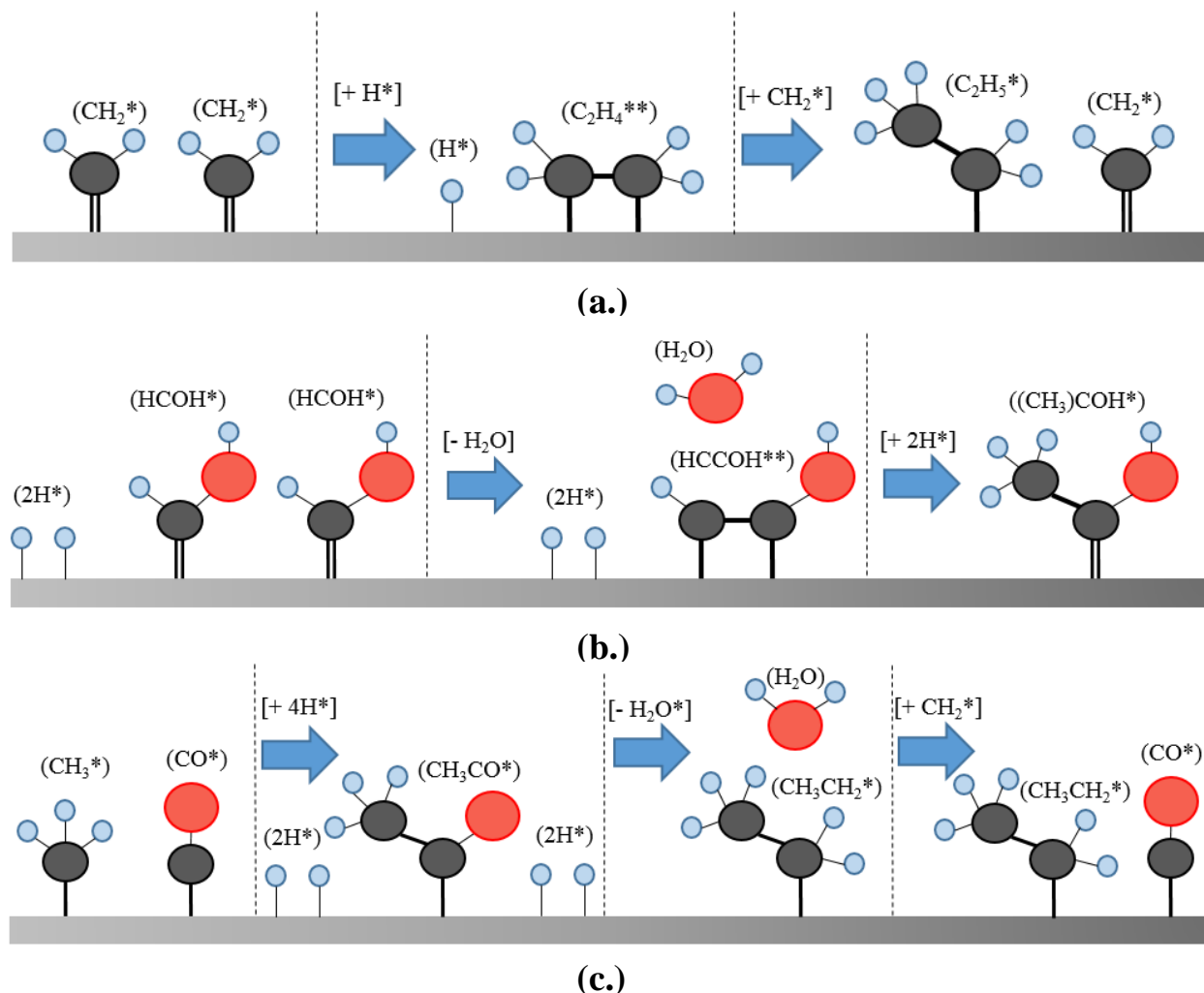
Figure 1.2. Proposed chain propagation mechanism by **(a.)** Fischer and Tropsch involving the direct coupling of CH_x^* monomers **(b.)** Anderson and Emmett involving the coupling of hydroxy methylene groups **(c.)** Pichler and Shultz involving the direct coupling of CO* adsorbates with growing carbon chains.

The alternative reaction pathway to chain propagation for hydrocarbon chains involves the termination (desorption) of the chains from the catalyst surface. One of the proposed reaction pathways for chain termination is that of a hydrocarbon chain becoming saturated through β-hydrogen abstraction (equation 1.8 or 1.9) before desorbing from the catalyst surface.

$$(CH_3)(CH_2)CH^* + H^* \leftrightarrow C_3H_{7(g)} \tag{1.8}$$

$$(CH_3)(CH_2)CH_2^* + H^* \leftrightarrow C_3H_{8(g)} \tag{1.9}$$

It is important to note that FT reaction mechanisms are dependent on the type of catalyst on which they occur. For example, for the two most common FT catalysts, cobalt and iron, catalyst the FT CO activation, chain initiation, and chain propagation/termination are proposed to go through different reaction pathways.

1.3. FT Catalyst

There are many catalysts that exhibit FT activity under different reaction conditions. A FT catalyst is considered to be any catalyst that activates CO and creates hydrocarbons. Some FT catalysts have a high selectivity towards methane like (nickel[30]) or produce alcohol groups like (copper[31]). Cobalt and iron are FT catalysts that exhibit the highest production of long hydrocarbon chains under specific reaction conditions. Industrial FT processes are dominated by these two catalysts for their own unique properties that will be explained in the following paragraphs. FT catalysts are rarely used in their elemental form and come in the form of an alloy to optimize their reactivity and/or increase their vitality. **Appendix D.1** and **D.3** shows the various Co and Fe FT reactors and catalysts configurations along with process parameters that can be found in various studies performed on these catalysts. Common additions to FT catalyst include potassium, copper, and boron. Industrial iron FT catalysts almost always include a combination of these elements in trace amounts. A FT catalyst is almost always used in tandem with a support. Supports metals such as Al_2O_3 are used as a medium for FT catalyst to adhere to and can increase the surface area available for a catalytic reaction by preventing particle sintering and helping minimize the effect of deactivation.

Cobalt is a common FTS catalyst used in many commercial FTS processes. It achieves high selectivity for high average molecular weight carbon chains at low to moderate FTS reactor temperatures (180^oC to 250^oC). In a literary review performed by Valero et al.[7], Co catalyst life-time integrity and optimal operation parameters were explored. According to their review, Co is more resistant to deactivation and requires a lower temperature range for optimal FTS reactions, (225^oC) as opposed to iron (340^oC).

Iron (Fe) is another common FTS catalyst used in industry and research. Unlike cobalt, Fe is much cheaper and can operate at more flexible ranges of temperature (higher temperature ranges than Co when no promoters are present). It is a unique FTS catalyst because it starts off as an iron oxide precursor (Fe_2O_3) and reduces to form an iron carbide layer before reaching peak FTS

reaction levels[32]. Un-promoted Fe catalyst cannot function optimally at low reaction temperatures that are otherwise optimal for Co catalyzed FTS processes. However, Li et al.[33] performed a study with promoted Fe catalyst with the goal of getting a high α-olefin and C_{5+} selectivity at temperatures (225°C) near the optimal cobalt catalyst temperature. Their study focused on the following promoted Fe catalysts: Fe-Zn, Fe-Zn-K_x-Cu_x, and Fe-Zn-K_x-Ru_x. The results of their study showed that Cu is a heavy influencer on the properties of Fe catalyst when accompanied by K. The best promoter combination found, that had the greatest positive effect on α-olefin and C_{5+} selectivity (along with a decrease in CH_4 selectivity), were the Fe-Zn-K_4-Cu_2 catalyst.

1.4. FT Optimization

One of the biggest challenges of FT catalyst research has been to increase the selectivity towards specific hydrocarbon products. The product distribution of FTS extends over a wide range of hydrocarbons that can extend from methane to C_{50+} paraffin waxes. In 1951, the ideal distribution of FT hydrocarbon products known as the Anderson-Shulz-Flory (ASF) equation (equation 1.10) was proposed to model the kinetics of the FT chain polymerization. The equation shows that the weight percentage (W_n) of a product containing n number of carbon atoms is controlled by a chain growth probability (α) term (equation 1.11)

$$W_n = n(1-\alpha)^2 \alpha^{n-1} \tag{1.10}$$

$$\alpha_n = \frac{(Rate\ of\ Chain\ Growth)}{(Rate\ of\ Chain\ Growth) + (Rate\ of\ Chain\ Termination)} \tag{1.11}$$

The basis of the ASF model stems from the proposal that FTS is kinetically controlled by stepwise chain growth and the polymerization of $CH_{x,(1-3)}$ groups on the catalyst surface. Based on this, polymerization rates can be assumed to be independent of the products formed leaving the probability of chain growth to be dependent on chain propagation versus chain termination[3]. **Figure 1.3** graphically represents the weight fraction of products versus the chain growth probability from the ASF model. The chain growth probability term is dependent on many factors ranging from catalyst properties (structure, composition, support, particle size) to reaction conditions (temperature, pressure, feed composition)[7, 10, 34-36].
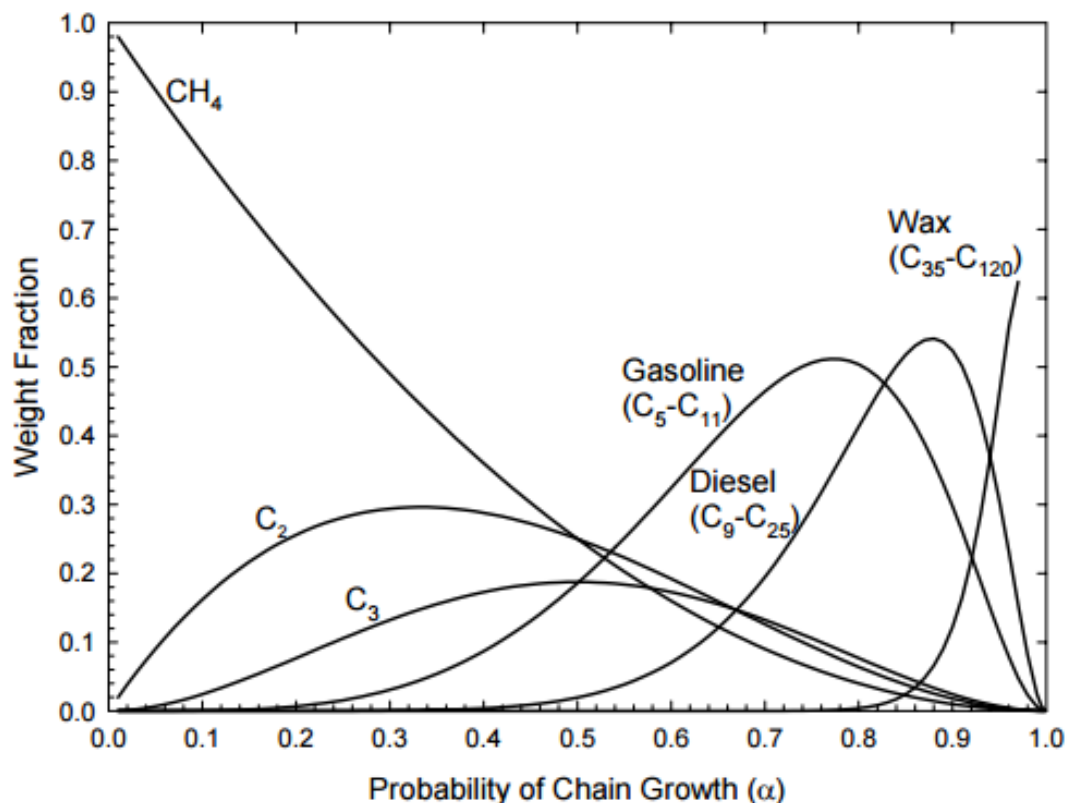
Figure 1.3. Ideal Anderson-Shulz-Flory Distribution[3]

FT catalyst properties and operational parameters have been heavily researched to maximize selectivity towards a single hydrocarbon product such as octane and narrow the ASF distribution to cut down on unwanted byproducts (various Co and Fe FT studies can be found in **Appendix D.2** and **D.4**). In the case of methane conversion to stable liquid fuel, the reduction of syngas conversion to methane is a primary concern of FT research. When dealing with natural gas conversion to large chain hydrocarbons, natural gas must first be converted into syngas through a process known as steam reforming. Steam reforming takes place between 800°C and 1200°C and is an energy intensive process, therefore any production of methane from the FT process represents wasted efficiency of the entire process, even if recycled. Production of methane vs higher hydrocarbons (C_{2+}) is dependent on the chain initiation and propagation phase where single carbon monomers ($CH_{1-3}*$) either begin the growth of a chain or continue the growth of a developing chain. CH* monomers that undergo hydrogenation before coupling with another monomer or growing chain consequentially form methane due to the irreversibility of CH_3* hydrogenation.

Through optimization of specific catalyst characteristics, these mechanisms can potentially be altered in a way that mitigates methane production and increases the rate of chain growth.

Research (*in situ* and *ab initio*) has shown that the surface characteristics of Co catalyst plays a crucial role in FTS reaction kinetics, particularly the chain propagation step. A study performed by Cheng J et al.[1] provides DFT derived adsorption energies for all reactants and reaction intermediates for the FTS reaction mechanisms on flat and stepped Co (001) surface based on the carbide initiation step. They performed activation energy analysis on all possible $C_1 + C_1$, $C_2 + C_1$, and $C_3 + C_1$ coupling reaction pathways on the catalyst surface (here the numbers correspond to amount of $C - C$ bonds present in the species) as well as the reversible hydration reactions ($CH_x + H$). The resulting activation energy barriers showed that stepped surfaces are favored over flat surfaces on Co for the majority of carbon chain coupling reactions (**Figure 1.4**). According to the study, the forward activation barriers for the coupling reactions on the flat surface are lower than for the reactions on the stepped surface. However, the lower adsorption energies of the initial and transition states of the stepped surface in comparison to the flat surface shows that the coupling
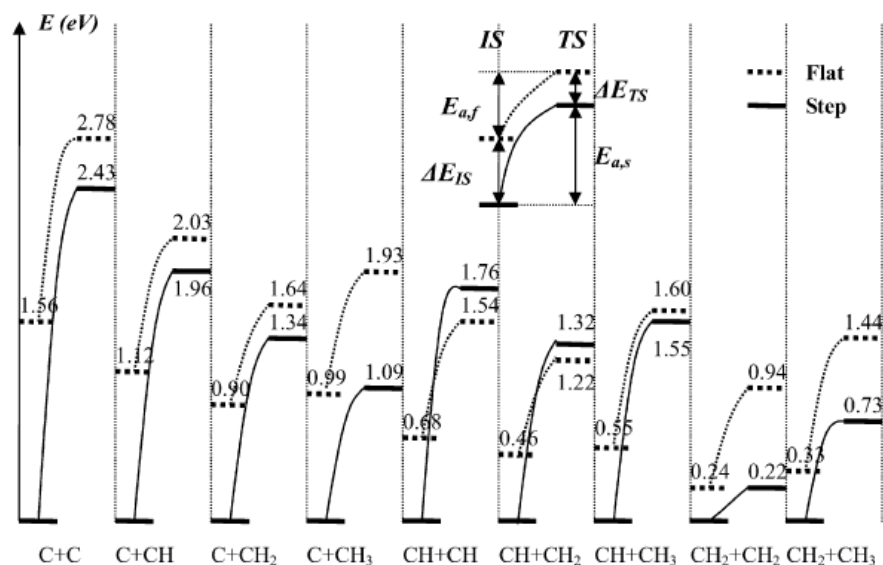
Figure 1.4. Carbon coupling reactions on flat (dashed line) and stepped (solid line) hcp Co (001). In this study by Cheng and his group[1], they found that most of the carbon coupling reactions on the stepped surface were more stable (lower adsorption energies for the initial and transition states) than the flat surface.

reactions are more stable on a stepped surface. Maximizing the presence of defect sites such as steps could therefore potentially enhance FT chain growth.

1.5. Crystalline Surface Structure

Studies have shown that FTS on a cobalt catalyst is sensitive to molecular surface structures[9, 10, 37, 38]. As mentioned in the last section, step sites have been shown by DFT calculations to affect the reaction rates of proposed primary FT reaction steps[1, 10, 22, 37]. Populating the Co catalyst surface with defects, which favor hydrocarbon chain production, would therefore theoretically increase chain growth and decrease methane production. In this case, a cobalt catalyst with high surface area of desired defects would be optimal for increasing hydrocarbon chain selectivity. One method of maximizing the surface density of a desired surface defect would be to expose a specific cobalt surface facet that has structural properties similar to that of the defect or by introducing a stable particle shape that has proportionally high ratios of defect sites. This could be done through size selective nanoparticle synthesis. An example of surface with high density of steps sites is the hcp Co (104) surface facet shown in **Figure 1.5**.
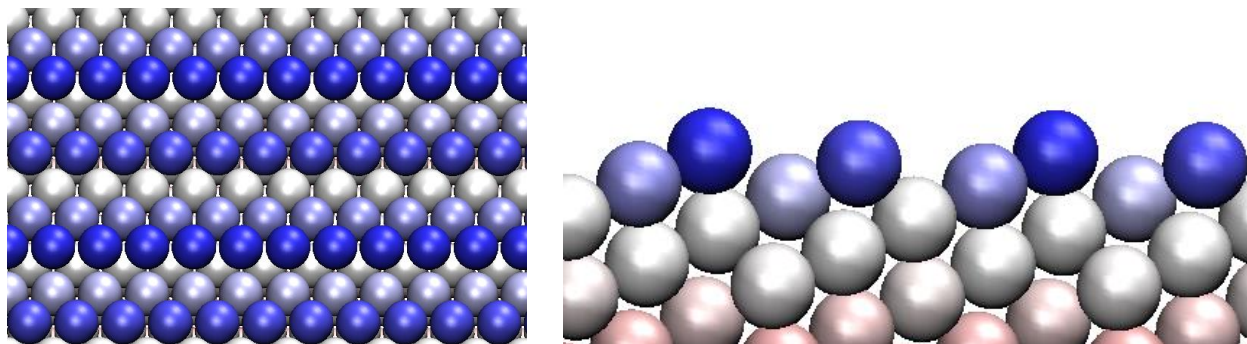
Figure 1.5. (left) Overhead view of a hcp Co (104) surface facet. (right) Side view of the hcp Co (104) surface showing the stepped structure repeated on the entire surface slab. The z-axis of the slab is represented by a dark blue color on the top of the surface that gradually turns to white and then red as you penetrate the surface.

Cobalt, like all metals, has a crystal structure when in the solid phase. Below 450°C, the crystalline structure of cobalt takes on a hexagonal-closed packed (hcp) lattice configuration. A martensitic transformation occurs above this temperature as cobalt's crystal lattice structure rearranges from an hcp lattice to a face-centered cubic (fcc) lattice structure[39] (**Figure 1.6**). Therefore, cobalt maintains an hcp crystal lattice structure at typical FT reaction conditions (180 – 250°C).
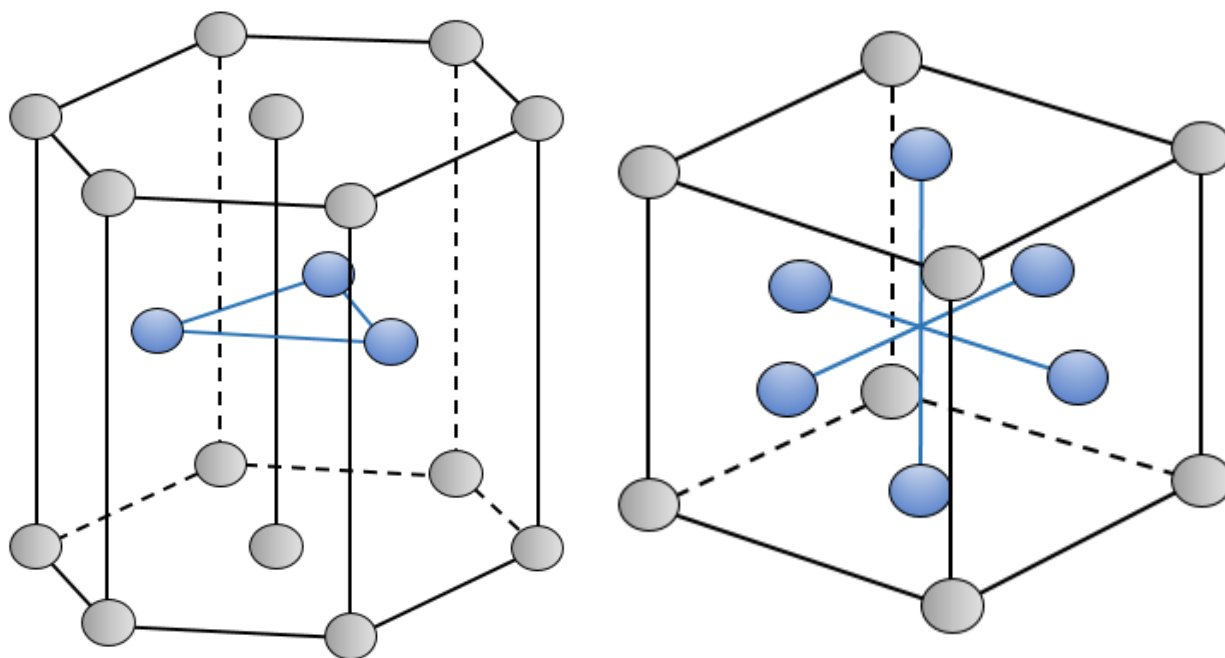
Figure 1.6. (left) Hexagonal Closed-Packed (hcp) lattice structure and (right) a face-centered cubic (fcc) lattice structure.

The surface of a cobalt catalyst takes on the formation of one of many vector planes of the bulk hcp lattice structure. These exposed planes or slices are known as facets. When a crystal lattice structure is sliced along a specific plane a specific facet is exposed. The vector orientation of the slice is known as the Miller Index and the plane is called the Miller Plane. Miller Planes are defined by the discrete points at which the plane intersects the axis of the defined unit cell. Two examples of hcp facets, (001) and (110), are shown in **Figure 1.7**. The (001) hcp facet is the most thermodynamically stable surface[40] and shows a hexagonal configuration which is deemed in some studies as being relatively flat[1, 37], especially when compared to the trench structure of a (110) surface facet. There are many different facets of hcp cobalt that range from the relatively flat (001) surface to the "zig-zag" trench like (110) surface (see **Appendix A.6**).
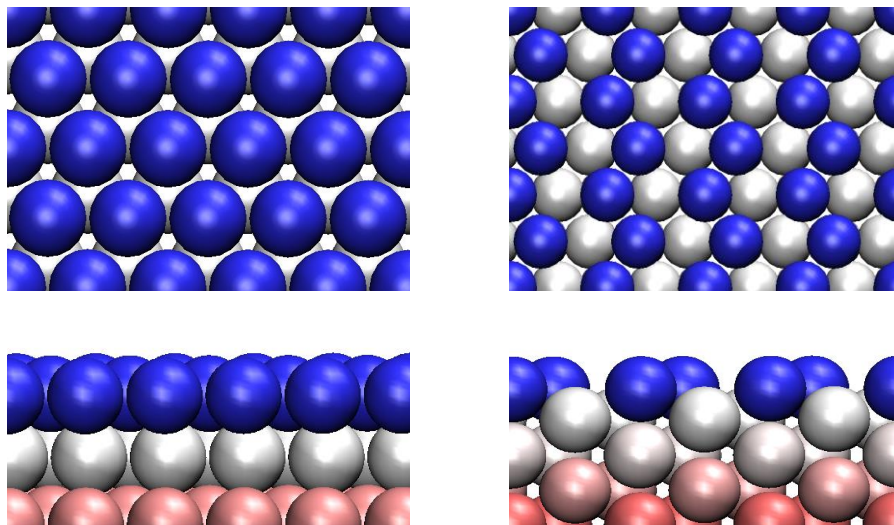
Figure 1.7. (left) Top and side view of a Co (001) surface and (right) top and side view of a Co (110) surface. The blue color represents the proximity of the atoms to the surface with a change from blue to white to red as you go further into the bulk. The Co (001) surface is considered flat in many DFT studies compared to "trench-like" surfaces such as Co (110).

Six low-index surface facets were investigated in this study. The six facets investigated were hcp Co (001), (100), (101)A, (101)B, (111)A, and (111) B. The (100)A and (100)B facets were also investigated, however due to computational complications (100)A and (100)B data has been excluded from this study. The difference between a facet indicated with an A and a B is the top layer. The top layer of (101)A, when removed, reveals the top layer of the (101)B surface. Continued removal of another layer would reveal the (101)A surface again. The (001) and (110) hcp facets are the only surfaces that have the same surface configuration regardless of the amount of layers that are removed. As mentioned in the last paragraph, Co (001) is the most stable hcp surface facet and will account for the majority of a Co catalyst's surface density until a high enough temperature causes the lattice to rearrange into an fcc configuration. This rearrangement will occur for the less stable surface layer of an (xxx)A and an (xxx)B. In the case of the low-index surfaces investigated in this study, the B configuration is the more thermodynamically stable surface[40] and any surface facet with an A configuration may stabilize to its B counterpart under the proper conditions.

1.6.   Objectives

The overall objective of this study is to contribute data to the scientific community that allows for further improvement of FTS product selectivity towards desired hydrocarbons (C_{5-12}). As a collaboration between industry and academia, atomic level modeling of key FT reaction steps

was performed to find optimal catalysts configurations (composition and structure) as well as optimal operation conditions that improve FT product selectivity. The reaction model in this study also serves as a surface boundary condition in larger "multiscale" reactor models including mass and momentum transfer as well as creating a starting point for FT optimization parameters sweeps.

Past studies have shown that cobalt surface structure can alter the kinetics of the FT reaction[1, 7, 37, 38, 41-44]. The objective of this study is to identify the important reaction steps for FT chain initiation/growth and investigate the effects of various low-index cobalt facets on the identified reaction steps using first principle calculations. If specific structures, such as kinks and steps, enhance FT chain growth reactions then surface facets that periodically replicate these structures should maximize the surface area of these desired structures and alter the overall reaction kinetics to favor chain growth and minimize methane selectivity.

As part of a collaboration between academia and industry, a novel, temperature swing reactor has been proposed for the purpose of theoretically increasing selectivity toward desired hydrocarbon products such as octane and lowering the selectivity of larger chain hydrocarbons (paraffin waxes). The second objective of this study is to probe and analyze a microkinetic model from the literature to calculate the upper and lower bounds of the temperature swing that must occur at the calculated time when the catalyst surface reaches maximum coverage of desired hydrocarbon. The ultimate objective is to calculate these parameters and determine whether or not the time and temperatures are feasible with current technology.

2. Theoretical Background

A typical FT industrial reactor using cobalt catalyst operates at over $200^{\circ}C$ and anywhere between 10 and 20 bars of pressure. At these conditions, the intermediate reactions involved in the FT process at the catalyst surface occur with turnover rates[1] between 10^{-8} and 10^{-16} sec^{-1}. This makes it challenging to directly observe and confidently conclude which are the most important reaction steps that influence CO activation and chain initiation/growth. With a limitation on experimental observation, many FT researchers have turned to first principle calculation methods to model the reactions that cannot be observed in situ[7]. Density Functional Theory and microkinetic modeling are two methods based on first principles that allow us to probe the mechanisms of reactions like FTS.

2.1. Density Functional Theory

Density Functional Theory (DFT) is a method for finding the approximate solution of the Schrödinger equation for a many-body atomic system. As opposed to the many-body electron wave function, that takes into account every individual electron and nucleus in a system, DFT investigates the electronic structure of molecules using functionals (functions of another function) of the electron density as illustrated in **Figure 2.1**. Once the ground state of the system is known, a complete description of the molecular properties of a chemical system can be determined such as molecular structures, vibrational frequencies, atomization energies, ionization energies, etc.
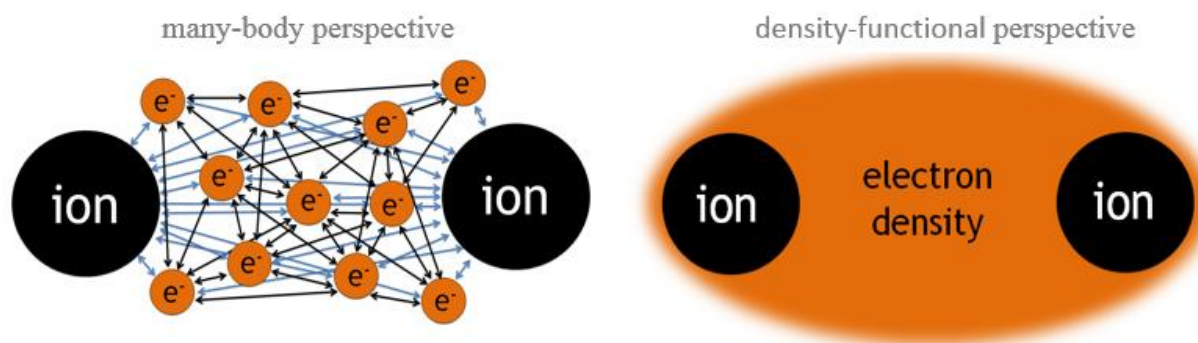
Figure 2.1. (left) The many-body perspective for investigating the electronic structure of an atomic system involves calculating the interactions between every particle (electron and nucleus) involved in the simulation as opposed to the density-functional perspective (**right**) that looks at the density of the electrons involved.

Equation 2.1 shows the general, time-dependent Schrodinger equation where í is the imaginery unit, $\hbar$ is the Planck constant divided by 2π and $\hat{H}$ is the Hamiltonian operator. Equation 2.2 shows the Hamiltonian for the Schrodinger equation when applied to a system of electrons and nuclei where m_e is the mass of an electron, M_I is the mass of the nucleus, R and r are positions of the nuclei and electrons, respectively, e is the electron charge, and Z represents the charge of the nuclei. The first term in equation 2.2 represents the kinetic energy of the electrons in the system and the second term is the potential energy of the electron-nuclei, coulombic attraction. The third term is similar to the second term, but represents the coulombic repulsion between nuclei. The last two parts of the Hamiltonian represent the kinetic energy of the nuclei and the potential energy of the electron-electron coulombic repulsion, respectively.

$$i\hbar \frac{\partial}{\partial t} \psi(r,t) = \hat{H}\psi(r,t) \tag{2.1}$$

$$\widehat{H} = -\frac{\hbar^2}{2m_e}\sum_i \nabla_i^2 - \sum_{i,I}\frac{Z_I e^2}{|r_i - R_I|} + \frac{1}{2}\sum_{i \neq j}\frac{e^2}{|r_i - r_j|} - \sum_I \frac{\hbar^2}{2M_I}\nabla_I^2 + \frac{1}{2}\sum_{I \neq J}\frac{Z_I Z_J e^2}{|R_I - R_J|} \qquad (2.2)$$

DFT is based on two theorems developed by Hohenberg and Kohn in 1964.[45] They showed that all properties of a system can be found from the ground state electron density, which in turn can be found by minimizing the expectation value of the Hamiltonian as a functional of the density. The process required for calculating equation 2.1 as a function of density starts with the Born-Oppenheimer approximation[46] which decouples the electronic and nuclear motions in the Hamiltonian. This approximation allows us to decouple the movement of the nuclei and the electrons, so for electron movement, the kinetic energy of the nuclei is assumed to be zero and the potential energy of the coulombic repulsion between nuclei terms is constant due to the extremely low mass of the electrons in comparison to nuclei. The electrons move instantaneously to any given nuclei displacement which allows the electrons to be considered to be moving in a potential generated by the nuclei. The application of the Born-Oppenheimer approximation results in the electronic Hamiltonian (equation 2.3). The first, second, and third terms represent the electron kinetic energy, potential of the nuclei acting on the electrons, and the electron-electron interactions, respectively.

$$\widehat{H}_e = \widehat{T}_e + \widehat{V}_{ext} + \widehat{V}_{int} \qquad (2.3)$$

The two theorems developed by Hohenberg and Kohn[45] were applied to a system of interacting particles in an external potential as shown in Equation 2.3. The theorems were written as follows by Hohenberg and Kohn:

Theorem 1 – "For any system of interacting particles in an external potential $\widehat{V}_{ext}(r)$, the potential $\widehat{V}_{ext}(r)$ is determined uniquely, except for a constant, by the ground state particle density $\rho_0(r)$".

Theorem 2 – "A universal functional of the energy E[n] in terms of the density n(r) be defined, valid for any external potential $\widehat{V}_{ext}(r)$. For any particular value of $\widehat{V}_{ext}(r)$, the exact ground state energy of the system is the global minimum value of this functional, and the density $\rho(r)$ that minimizes the functional is the exact ground state density $\rho_0(r)$".

These two theorems did not lay out the procedure for solving the Hamiltonian for a many electron system. Kohn and Sham[47] developed a method for calculating the ground state density which eventually became the basis for all modern DFT codes. Two major assumptions were made in Kohn and Sham's approach which allowed for them to convert the interacting many particle Hamiltonian to a system of non-interacting electrons and nuclei with an effective potential including exchange-correlation effects for a real interacting system. Equation 2.4 is used to define the density functional by converting equation 2.3 from being a function of individual electron positions to a function of overall electron density. The resulting application of equation 2.4 to equation 2.3 results in the Kohn-Sham modified Hohenberg-Kohn equation for solving ground state energy for a many body system as a function of electron density (equation 2.5) where ρ represents electron density, V_{ext} is the external potential (from the surrounding electron density), T is the kinetic energy term, and E_{xc} is the exchange-correlation energy.

$$\rho(r) = N \int |\psi|^2 (r, r_2, \dots, r_n) dr_2 \dots dr_n \tag{2.4}$$

$$E(\rho) = T(\rho) + \int \rho\, V_{ext} + \frac{1}{2} \iint \frac{\rho(r_1)\rho(r_2)}{|r_1 - r_2|} + E_{xc}(\rho) \tag{2.5}$$

The last term in equation 2.5 is the exchange-correlation potential that accounts for all the many body effects of exchange and correlation. There is no exact form for the exchange correlation potential which is dependent on the nature of the system under investigation. The first developed approximation was the local density approximation (LDA)[48] where the electronic system is approximated as a homogenous electron gas over the whole investigated space (equation 2.6).

$$E_{xc}^{LDA}[\rho \uparrow, \rho \downarrow] = \int d^3 r \rho(r)\, \varepsilon_{xc}^{hom}(\rho \uparrow (r), \rho \downarrow (r)) \tag{2.6}$$

Another exchange-correlation potential (used in this study) is the generalized gradient approximation (GGA)[49]. It is an improved version of LDA that has the ε_{xc}^{hom} term as a function of both the electron density and the electron density gradient as shown in equation 2.7.

$$E_{xc}^{GGA}[\rho \uparrow, \rho \downarrow] = \int d^3 r \rho(r)\, \varepsilon_{xc}^{hom}(\rho \uparrow (r), \rho \downarrow (r), \nabla\uparrow, \nabla\downarrow) \tag{2.7}$$

There are variations of the LDA and GGA exchange-correlation potentials that have been proposed. In 1991, Perdew and Wang developed a commonly used approximation known as PW91[50] that was later improved by Perdew, Burke, and Ernzerhof (PBE).[24] Other commonly used GGA exchange-correlation potentials are the rev-PBE[51] functional and R-PBE[52] functional.

2.2.   Vienna Ab Initio Simulation Package

A large amount of computational power and software tools are required to perform the necessary DFT calculations for this investigation. A group led by Jürgen Hafner, Georg Kresse, and Jürgen Furthmüller developed the Vienna Ab Initio Simulation package (VASP)[53] that computes an approximate solution to the many-body Schrödinger equation, either within DFT, solving the Kohn-Sham equations, or within the Hartree-Fock (HF) approximation, solving the Roothaan equations. As stated on their website, "In VASP, central quantities, like the one-electron orbitals, the electronic charge density, and the local potential are expressed in plane wave basis sets. The interactions between the electrons and ions are described using norm-conserving or ultrasoft pseudopotentials, or the projector-augmented-wave method[54]". VASP is a software tool that can be used to make a vast array of different calculations ranging from simple ground state energy calculations of an O_2 molecule to the transition state search of a hydrocarbon coupling reaction on a Pt (111) surface. VASP also includes a vast library of different pseudopotentials and electronic data for individual atoms and molecules. Along with the extensive calculations and data libraries comes an informative website that includes a manual for setting up desired calculations and an extensive user community for trouble shooting and information sharing. In VASP the local potential is expressed in plane waves. This is a natural choice to calculate extended periodic system such as metal surfaces and leads to periodic boundary conditions. **Figure 2.2** shows a unit cell for a 4-layer Co (001) repeated to a 3x3 supercell with 1 ML of CH* on the surface included with a 10 Å vacuum layer in the z direction.
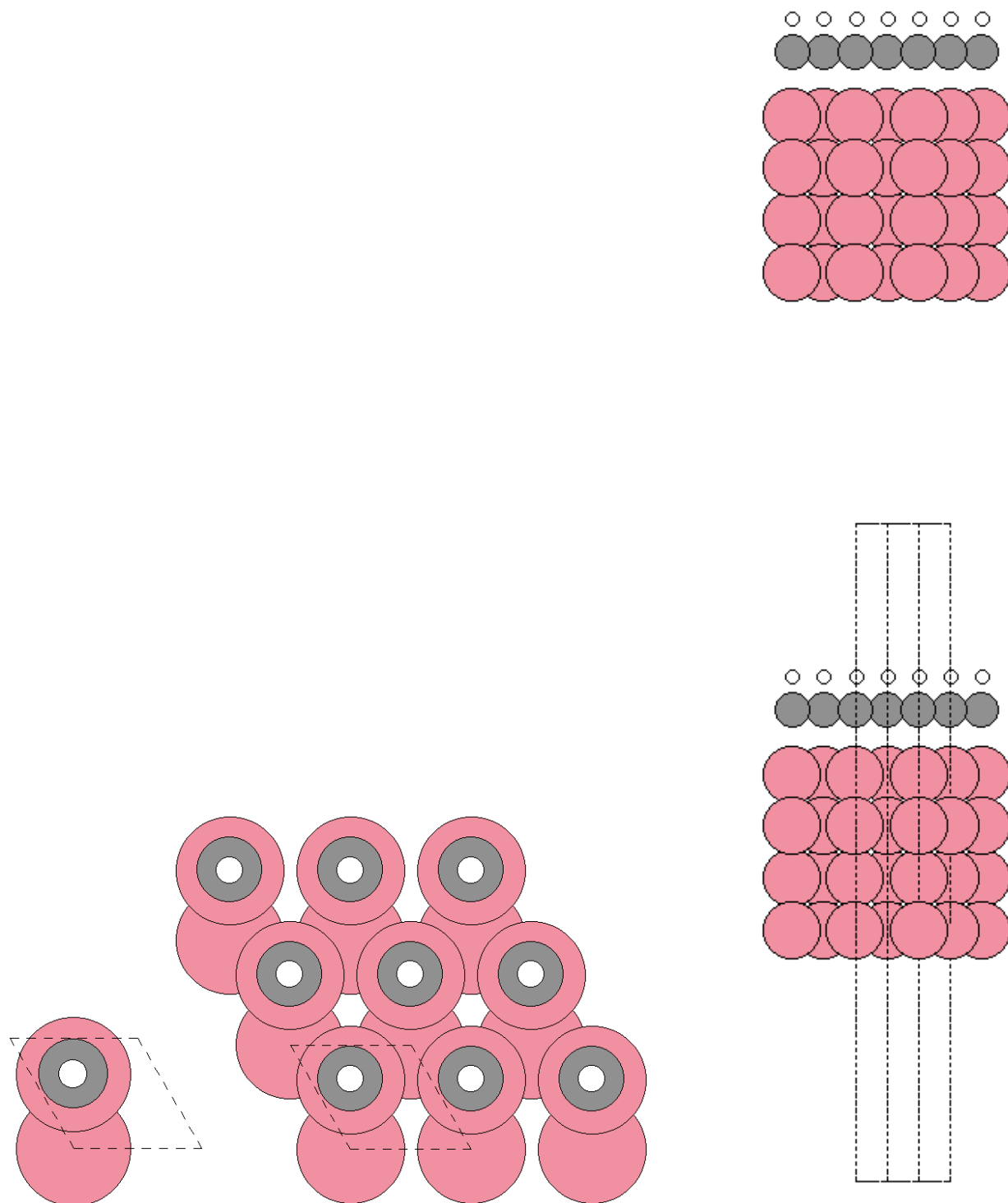
Figure 2.2. Illustration of how VASP can simulate an infinite slab by repeating the periodic boundary of a smaller unit cell. This figure shows a Co (001) surface being repeated in the x and y directions of a coordinate plane with a CH* adsorbate (grey/white circles) also being repeated on the surface (left and middle images). The image on the right shows the 3x3 slab being repeated in the z direction. The space between the slabs is known as the vacuum layer.

2.3.   Nudge Elastic Band

Climbing image nudged elastic band (CI-NEB)[55] calculations are performed in this study in order to locate transition states and calculate forward and reverse activation barriers. This specific calculation is implemented through VASP and uses stable initial and final states of reactions. In order to implement this calculation, images showing the progression of a reaction between the initial and the final states are created by interpolating between the two states and are relaxed to converge to the path of minimum energy. The transition state image is the image with the highest relative minimum energy at the saddle point in the potential energy surface. The relative difference between the initial state energy and the transition state energy is the forward activation energy barrier (Ea_f) for the investigated reaction. The difference between the final state energy and transition state energy is the reverse activation energy barrier (Ea_r) and the difference between the initial and final state energies is the reaction energy (ΔE_r). These different energies are illustrated in **Figure 2.3.**
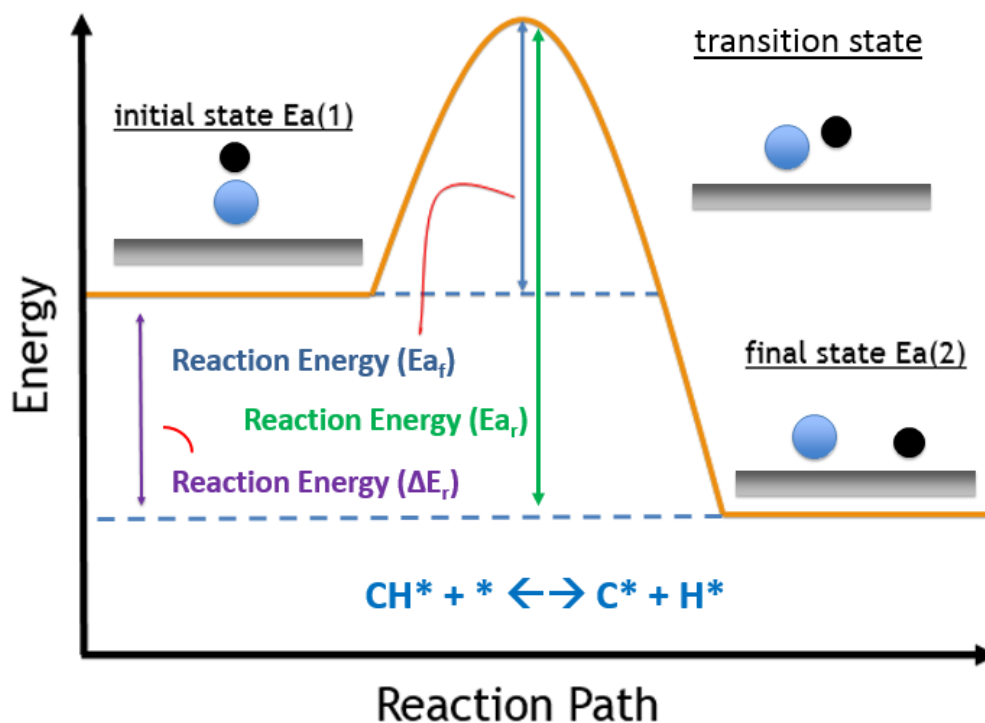
Figure 2.3. Cartoon illustration showing the forward and reverse activation barriers for a general reaction diagram. A specific amount of energy is required for the CH* monomer to dissociate (forward activation barrier). The transition state is at the saddle point in the minima energy landscape and is where the reaction can either recombine or fully dissociate into C* and H* monomers. The energy required for recombination is the reverse activation barrier (or formation barrier) and the difference in energy between the Initial and Final state is the reaction energy.

3. Computational Approach

FT production of C_1 and C_2 hydrocarbons was simulated using a microkinetic model from the literature[15]. This microkinetic model served as a base tool to focus our computational efforts through further analysis with a degree of rate control method[56]. Upon determining the rate-limiting reaction steps for C_2 chain production, the effect of surface structure on these reactions were calculated on low-index cobalt facets. Periodic DFT code (implemented via VASP) was used to calculate the bulk cobalt crystal lattice and to simulate a surface as an infinite slab. The surface models was converged for different computational criteria such as vacuum and slab thickness and the number of relaxed and fixed molecular layers, all of which were investigated and converged to maximize model accuracy and integrity.

3.1. Microkinetic Model

A microkinetic model is a tool used for the mechanistic study of a reaction network where a reaction mechanism and the molecular properties of reactants and intermediates are used to simulate the reaction kinetics and the effects of various operational parameters, T, P etc., at more microscopic levels[57]. The foundation of the model can be based of first principles derived from DFT calculations, on experimental data, or both. The microkinetic model discussed below is based on DFT calculations. The microkinetic model consists of basic reactor inputs (PFR kinetics), feed inputs, number of active surface sites, operating condition inputs (Temperature, Pressure, H_2/CO, and Gas Hourly Space Velocity (GHSV)), and the reactions of interest. The model yields surface adsorbates, unconverted feed gas, and gaseous products/byproducts as well as countless other details. A microkinetic model can also serve as the second step in formulating an overall integrated reactor model. Its purpose can be to serve as the surface boundary condition for a larger scale, microfluidic model. **Figure 3.1** illustrates where a microkinetic model can be applied (the reactions on the catalyst surface) in conjunction with a microfluidic model that investigates overall bulk fluid in the reactor (concentration, temperature, and flow data).
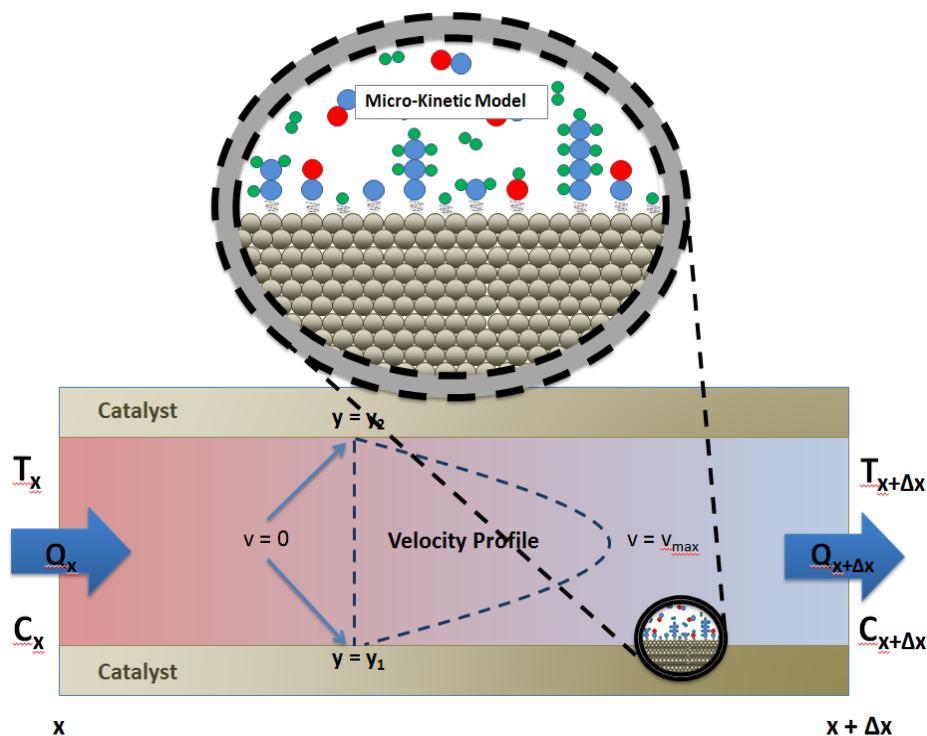
Figure 3.1. The above diagram shows how the micro-kinetic model fits into a microfluidic reactor model. Information and analysis performed on the micro-kinetic model is fed into the surface boundary conditions of the micro-fluidic model.

The two models would interact through the boundary conditions in the microfluidic model. The microfluidic model is a critical piece of the collaborative effort towards a new reactor design and will function as an interface between the DFT calculations and the experimental measurements. The kinetic part of this model will be discussed herein but the coupling of the microkinetic model and the fluidic model will be discussed in A.C.Traverso thesis (expected defense in 2019).

Two microkinetic models were recreated from literature for this study. The model used to characterize our temperature-swing reactor system was recreated from a study by Kraft et al[16]. His group used DFT kinetic parameters from the literature to seed a model for a spinning basket cobalt FT Reactor. Mass diffusion limitations were assumed to be negligible and their model looked at hydrocarbon chain production for C_1 to C_{30} hydrocarbon chains.

The other microkinetic model, from a study done by Holmen et al[15], was recreated for the purposes of investigating the FTS reaction on a 001 hcp cobalt surface, and served as a tool to identify the rate-limiting reaction steps for hydrocarbon chain formation, as well as an interface between the DFT calculations and the experimental measurements for Co catalysts testing (also to

be discussed in A. C. Traverso thesis). The model developed by Holmen and his group looked at C_1 and C_2 hydrocarbon chain growth and included many of the intermediate steps involved in the process. The purpose of their study was to identify the primary mechanism(s) involved in chain formation (carbide mechanism, CO insertion mechanism, or a hybrid of the two) and CO activation (CO hydrogenation and hydrogen-assisted CO dissociation). A microkinetic model for each of the two proposed CO activation mechanisms was developed and a third microkinetic model was developed as a combination of the two including the water-gas shift reaction.

3.1.1. Activation Barriers, Pre-exponential Factors, and Reaction Rates

Rate constants were calculated using the Arrhenius Equation (equation 3.1) in conjunction with activation energies (ΔEa) and preexponential Factors (A) from the literature[15]. Temperature dependence of the adsorption preexponential factors was determined using the Hertz-Knudsen equation for the flux of incident molecules (equation 3.2). Desorption and surface reaction preexponential factors had temperature dependence determined by equation 3.3 which was part of the calculation used in the literature[15] to determine the preexponential factors for the surface and desorption reactions.. The temperature used to determine the rate constant parameters in the literature (T_{lit}) was 483 K. Units for the activation energies from the literature were given in [kJ/mol]. Preexponential factors for adsorption and desorption were given in [1/bar*sec] and [1/sec], respectively.

$$k = A \times exp^{\left(\frac{-\Delta E_a}{RT}\right)} \tag{3.1}$$

$$A = \frac{P}{(2\pi m k_b T)^{\frac{1}{2}}} \sim T^{-\frac{1}{2}} \tag{3.2}$$

$$A = \frac{k_b T}{h} \sim T \tag{3.3}$$

Reaction rates were determined from the network of surface reactions for the production of water, carbon dioxide, methane, ethene, ethane, and ethyne using the carbide mechanism. The reactions used in the model along with their rate equations can be found in **Appendix A.1.** The

rate equations (based on equation 3.4 and 3.5) given in Appendix A.1 were used to calculate the rates of production for each surface species and gaseous reactants.

$$A + B \leftrightarrow C + D \tag{3.4}$$

$$r_A = \frac{\partial A}{\partial t} = k_r[C][D] - k_f[A][B] \tag{3.5}$$

The reaction rate equations were solved using a Matlab ODE solver (Ode23s) to solve the model. Ode23s is based on a 2nd order modified Rosenbrock formula and is a one-step solver designed to solve stiff ODEs. The complexity and extremely fast reaction rates present in the microkinetic model caused normal implicit solvers like Ode45 to crash. The table in **Appendix A.2** shows the equations used for the overall rates of the surface species (equation 3.4) and the table in **Appendix A.3** shows the equations used from the overall rates of the gaseous reactants and products. To account for the gaseous reactants in a plug flow configuration, a mass and site balance was performed in the solver. Plug-flow kinetics was used to account for the mass balance of gaseous reactants (In – Out + Generation = Accumulation). Inputs and outputs of gaseous reactants had units of partial pressure and equation 3.5 was used to account for reactor kinetics using theoretical reactor volume (Vr), gas hourly space velocity (τ), ideal gas constant (R), temperature (T), and Avogadro's number (N_A).

$$\frac{d\theta_A}{dt} = \pm r_{x1} \pm r_{x2} \pm r_{x3} \pm \cdots \tag{3.6}$$

$$\frac{dC_A}{dt} = \frac{(P_{A,0} - P_A)\tau}{RT} + \frac{(r_{x1} \pm r_{x2} \pm \cdots)}{N_A V_R} \tag{3.7}$$

3.1.2. Model Evaluation

A recreation of the microkinetic model found in the literature was developed using Matlab. Operational parameters such as pressure, temperature, and H_2/CO ratio were programmed based on the model conditions (1.85 bar, 483 K, and 10 respectively) for matching surface coverage of the model created in this study with that of the model found from the literature. **Table 3.1** shows a comparison between the surface coverage of reaction adsorbates from the literature model and the recreated model for this study. It is important to note that the activation barriers and

preexponential factors were used from the literature model but the mechanisms for the two models differed (literature model used CO insertion mechanism whereas this study's model used the carbide mechanism). Due to this discrepancy, reasonable comparison could only be made between the resulting surface coverages of the two models.

Table 3.1. Comparison of surface coverages between the model developed in literature (based off the CO Insertion Mechanism) and the model based off the same rate constants (Carbide Mechanism). Note: Due to the difference in mechanisms, reasonable comparison can only be made between the surface coverages of hydrogen and carbon monoxide. Both models are tested at P = 1.85 bar, T = 210°C, and $H_2/CO = 10$.

Surface Species	Surface Coverage (Literature)	Surface Coverage (Model)
CO	3.2×10^{-1}	3.0×10^{-1}
H	5.9×10^{-1}	6.3×10^{-1}
Active Sites (left)	8.5×10^{-2}	6.5×10^{-2}

Since the objective of this study is to improve FT selectivity, the microkinetic model was tuned to conditions that optimized chain growth before looking at catalyst optimization. FTS is very temperature sensitive so a temperature parameter sweep for optimal C_2 hydrocarbon production was performed between 180°C and 300°C as shown in **Figure 3.2**. The figure shows the steady state production of C_2 gaseous products and methane (normalized so they could fit on the same graph). The green line shows the ratio of methane production rate to C_2 production rate which has also been normalized to fit on the same graph. The optimal temperature for C_2 production was found to be 229°C which falls into the literature range[13, 58-61] for optimal cobalt FT chain growth at the specified operational conditions. A local maximum production rate for methane was found at 250°C and the production rate of methane overtakes the production rate of C_2 hydrocarbons (green line) at roughly 280°C.
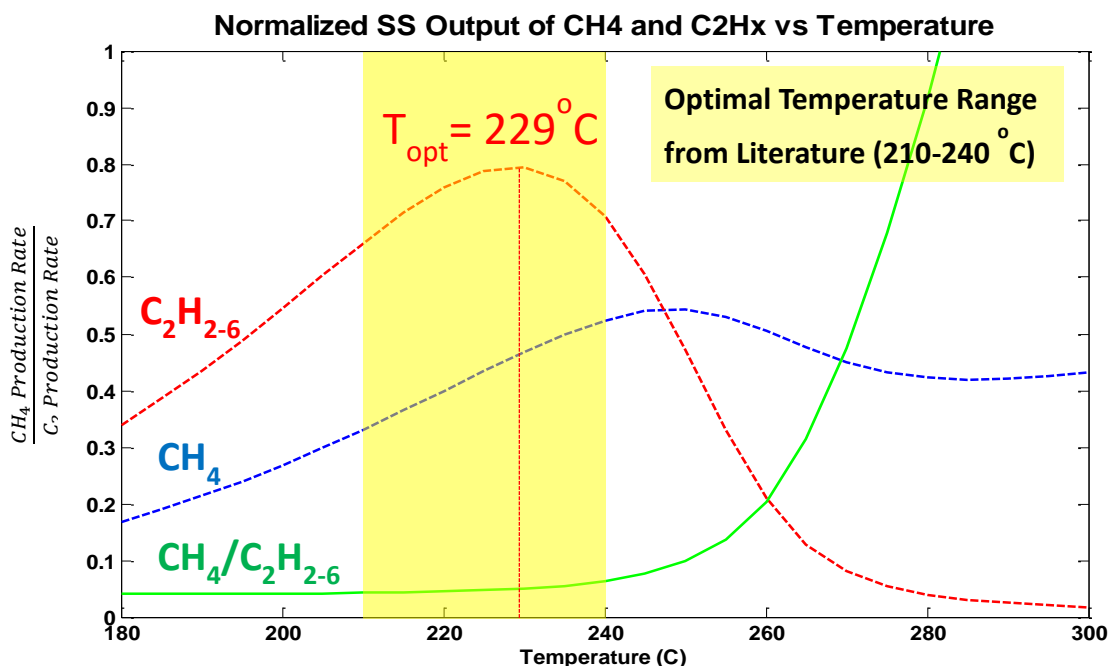
Figure 3.2. Graph of steady-state output of CH_4 and C_cH_{2-6} vs. reaction temperature. Temperatures range from 180°C to 300°C. The red and blue lines represent normalized production rate data. The purpose of this graph is to show the temperature where maximum CH_4 and C_2 production occurs.

3.1.3. Degree of Rate Control

A degree of rate control analysis (DRC)[56, 62] was performed on the microkinetic model to determine the rate-limiting reaction steps for FT chain initiation and growth at reactor operational conditions. DRC works by altering the rate constant of each elemental reaction step individually by 1% while leaving all other rate constants for the other reactions unchanged. Equilibrium rate constants (k_r/k_f) were held constant for all reactions. This is performed on each reaction step and the effects on overall rate and selectivity are monitored. The overall affects of each step is summarized in equations 3.6 and 3.7 and are used to find the Degree of Rate Control (X_{rc}). The larger the value of X_{rc}, the greater influence the reaction has on the output condition under investigation (in our case, steady-state $C_2H_{2-6(g)}$ production). This analysis can be performed in conjunction with operating condition parametric sweeps to show how the rate-limiting reaction steps' influence changes over an operating condition range such as temperature. **Figure 3.3** shows a graphical example of DRC results. The figure shows the influence of key reaction steps over a temperature range.

$$X_{rc,i} = \frac{k_i}{R_i}\left(\frac{dR}{dk}\right) \tag{3.6}$$

$$\sum X_{rc,i} = 0 \tag{3.7}$$
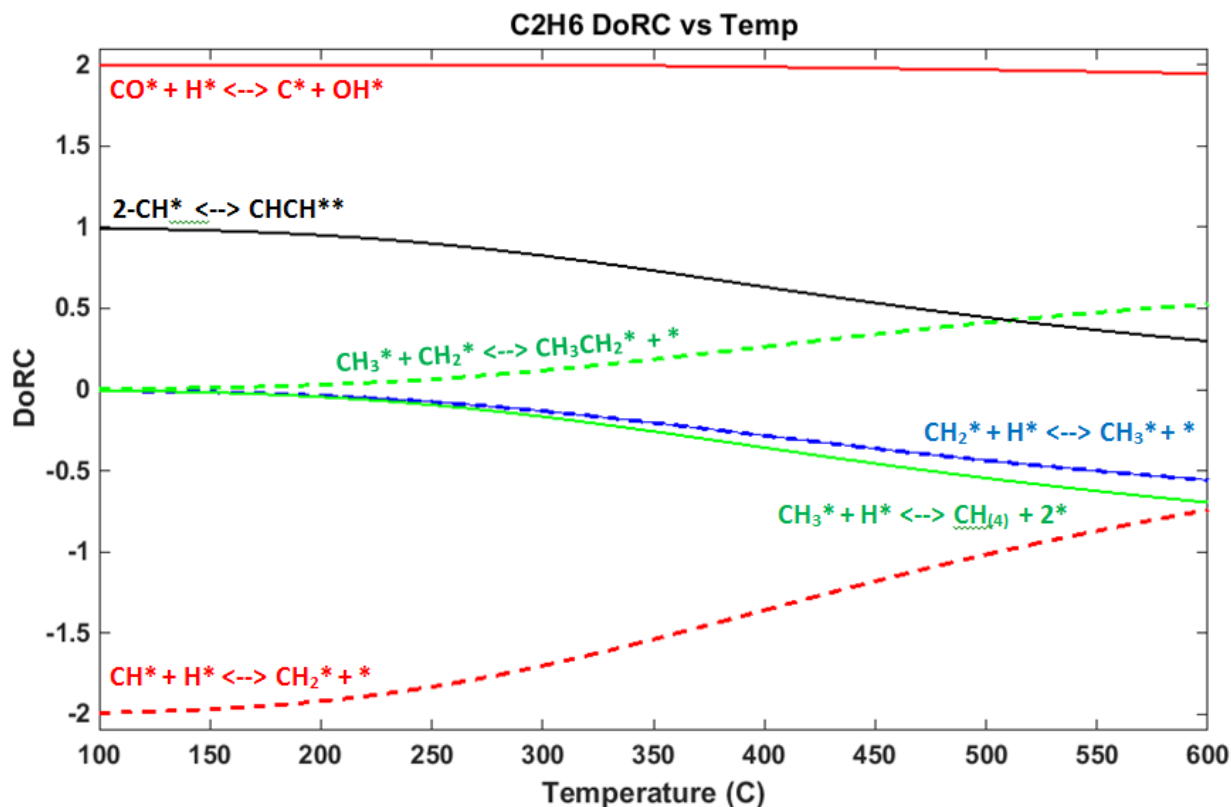
Figure 3.3. A Degree of Rate Control graph in conjunction with a temperature sensitivity analysis. Values close to zero mean that the reaction has little effect on the output being investigated. In large reaction systems, many of the reactions have DoRC values very close to zero and can be left off the graph.

3.2. Surface Slab Setup

Eight cobalt surface slabs, two for each facet with an A and B form, were simulated with four to six layers depending on the complexity of the surface structure. The periodic images are separated by 10 Å vacuum layer in z-direction. A 10 Å vacuum layer above the surface is standard common vacuum thickness used in DFT studies[22, 37, 63-70] based on the convergence of adsorbate adsorption energies near 10 Å of thickness. **Figure 3.4** shows the top view of each low-index hcp surface slab created for the study that had all required calculations performed. The Co (001) surface was used as a verification model for comparison to past studies done on Co (001) as well as serve as a reference for the other models to be compared too. Considered in most studies to be flat, the Co (001) surface has been the most heavily researched Co surface facet[1, 37, 64, 71]. The Co
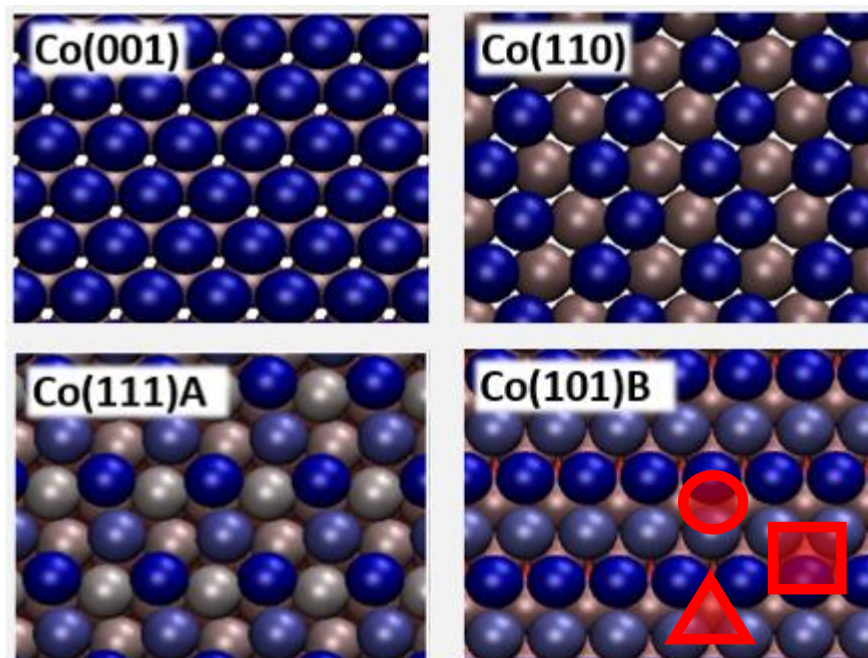
Figure 3.4. Top view of four of the eight surfaces modeled for this study. The surface structure varies wildly between the surfaces. On the (101)B surface, the square highlights the 5-fold site, the circle highlights the 4-fold site, and the circle highlights the 3-fold site

(110) surface has also been shown to be the second most thermodynamically stable surface facet[40] after (001) and exhibits a well-defined "trench-like" surface structure that is shown in blue in parallel "zig-zag" formations. The (111)A surface exhibits a less-defined "trench-like" surface structure and the (101)B surface is almost as flat as the Co (001) surface but with 5-fold sites included as opposed to the 3-fold sites present on Co (001). **Appendix B.2** and **B.3** shows the top views of all six surfaces modeled.

The goal of this study is to compare the effects of various surface facets so all models parameters are kept consistent. All slabs have either eight or nine surface atoms. Surface dimensions in the x and y coordinates varied for each surface facet to maintain consistent surface coverage (0.1 to 0.25 ML) during adsorption and reaction modeling while incorporating all unique features of each particular facet. Facets such as the (101)B facet, require large slab sizes to include two possible minimum adsorption energy active sites for the modeling of initial states for the rate-limiting reactions. Active sites are locations on a catalyst surface with lowest potential energy of adsorbate surface interactions and where adsorbates prefer to bind. The location of an active site is dependent on the adsorbate in question. **Figure 3.5** shows the different active sites available on an hcp (001) cobalt surface slab. A CH* monomer can occupy all the shown active sites but has a preference for the site that yields the lowest potential energy configuration. This lowest potential energy site

can change depending on the coverage. A CO* adsorbate on hcp (001) cobalt prefers a 4-fold site at low coverages but at higher coverages (0.8 -1.0 ML) prefers top-site[2].
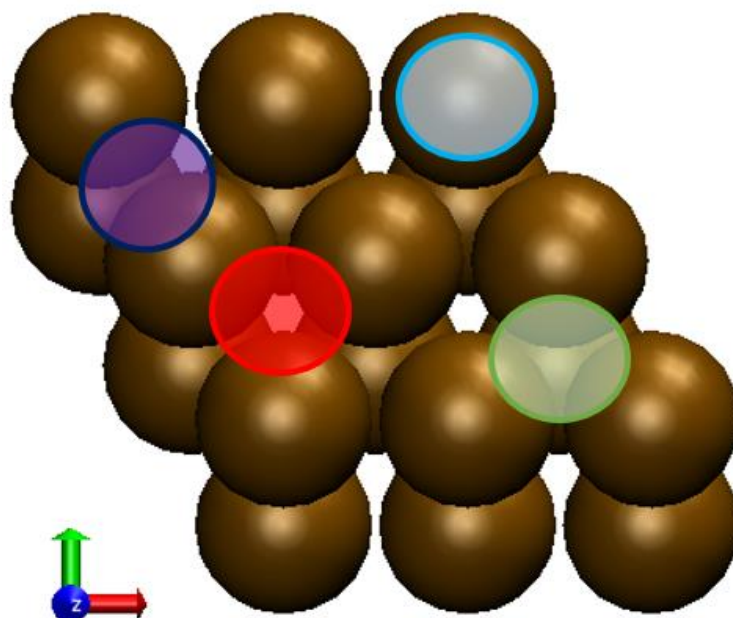
Figure 3.5. This figure shows the top of an hcp Co (001) (3x3) slab. There are four different possible sites for an adsorbate to occupy; (blue) top site, (red) 3-fold site, (green) 4-fold site, and (purple) a bridge site.

3.3. DFT Computational Details

All calculations were done using the Vienna Ab Initio Simulation Package (VASP) program. The exchange and correlation energies were included by using the Perdew-Wang generalized-gradient approximation (GGA-PW91). Ionic cores were described by ultrasoft pseudopotential (USSP) and spin polarization was included to account for the magnetic nature of the cobalt system. The surfaces were tested for computational and physical convergence over various parameters as shown in **Appendix A.5**. A bulk model was made and the adsorption energy for CH* on a Co surface slab of each low-index facet was calculated for increasing k-point meshes until the adsorption energies converged within 0.1 eV. The k-points used were dependent on slab geometry. A k-point calculator[72] that specifies the correct k-points specific to the geometry of the model in question was used for each low-index surface slab model.

Other tested parameters included slab thickness, number of relaxed layers, and energy cutoff (ENCUT: 250 and 400 eV)). Computational and physical convergence testing showed that a p(3x3), four layer thick (top two relaxed) model was appropriate for a Co (001) surface. An energy

cutoff off of 400 eV was found to be appropriate for all the models. The calculated lattice constants of the Co primary cell were a = 2.48 Å and c = 4.08 Å in good agreement with experiments, a = 2.51 Å and c = 4.07 Å.[1] **Appendix A.5** shows the results of the convergence testing of each of the mentioned computational properties.

3.4.   Surface and Adsorption Models

The formation of the surface slabs from a bulk crystal structure was performed while maintaining 2-D periodicity. 3D periodicity was also maintained with a 10 Å vacuum layer between each slab in the z direction to reduce slab interaction in the z direction to negligible levels. The incorporation of a vacuum layer breaks symmetry in the z direction which under-coordinates the surface layer in comparison to the bulk crystal layers. This under-coordination causes the relaxation of the surface atoms as they stabilize. In the presence of an ad-atom, under-coordinated surface atoms will share electrons with the adsorbate and bind them to the surface. The energy of this bond is known as the binding or adsorption energy. It can be quantitated by comparing the ground state energy of the atom or molecules by itself in a vacuum ($E_{molecule}$), the energy of the total system (adsorbate and slab, E_{sys}), and the energy of the surface slab (E_{slab}) as shown in equation 3.6.

$$E_{ads} = E_{sys} + (E_{slab} - E_{molecule}) \tag{3.8}$$

When multiple adsorbates are present on the surface the total adsorption energy is found by subtracting the energy of each individual adsorbate ($E_{molecule,n}$). An interaction is also present between adsorbates when two or more are present on a surface. This binding energy is converted to bond energy as adsorbates become closer to each other. This bonding energy is assumed to be negligible when surface adsorbates are separated by a large enough distance. A visual representation of the binding energy calculation is shown in **Figure 3.6**.
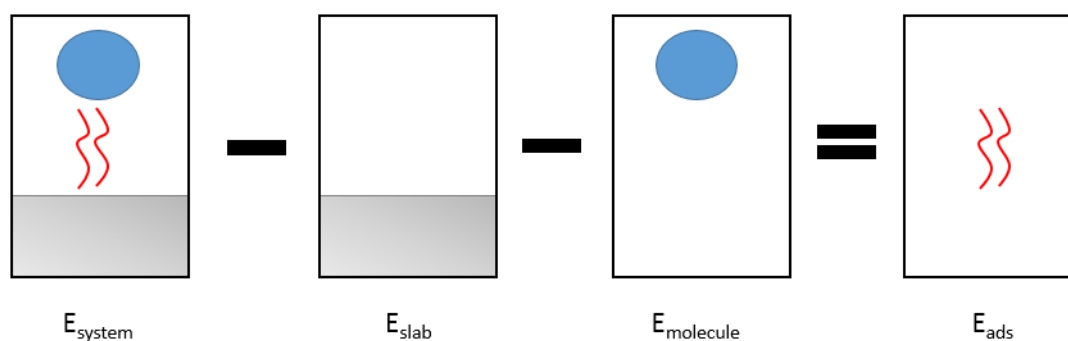
Figure 3.6. Visualization of finding the adsorption energy of a single atom on a modelled surface slab. The total energy for the slab (by itself) and the atom (by itself) is subtracted from the total energy of the overall system to find the left over binding energy of the atom to the surface.

A Co (001) hcp surface slab was used as a reference slab for the facet comparison study as well as a verification slab for achieving a CH* adsorption energy comparable to the literature[1, 2, 19, 64]. **Table 3.2** compares the CH* binding energy found in this study to four other studies performed in the last 15 years. Experimental data for CH* adsorption on Co (001) is not currently available due to the unstable nature of CH* radicals. The adsorption of CH* on Co(001) has been investigated with DFT in many studies and has been found to occupy a 4-fold site with an adsorption energy between -5.85 and -6.54 eV. The adsorption energy for CH* on a Co (001) 4-fold site was calculated to be -6.21 eV in this study.

Table 3.2 Table comparing literature data for CH* adsorption on a hcp Co (001) surface at a 4-fold active site

	CH* ads (eV)	**Model Details**	**Ref.**
This Study	-6.21	USSP-GGA-PW91; 3x3x4 Slab; k-points 5x5x1	
Literature	-6.31	USSP-GGA-PW91; 2x2x5 Slab; k-points 5x5x1	[19]
Literature	-5.99	USSP-GGA-PW91; 4x2x4 Slab; k-points 3x3x1	[64]
Literature	-6.54	DZP-GGA-PBE; 2x2x4 Slab; k-points 3x3x1	[1]
Literature	-6.14	USSP-GGA-PW91; 2x2x4 Slab; k-points 5x5x1	[2]

4. Chain Growth Rate-Limiting Reaction Steps

FTS chemistry is a complicated network of reactions involving multiple reaction mechanisms from CO and H_2 adsorption to C_{2+} hydrocarbon chain propagation/production. To

better understand what controls the reaction rate and the selectivity of FT synthesis a microkinetic model of FTS on hcp (001) cobalt, based on previously published work from the literature, was used. A Degree of Rate Control Analysis was performed on the microkinetic model to identify the rate-limiting reaction steps for C_2 hydrocarbon production. The rate-limiting reaction steps found from the analysis were further scrutinized until two rate-limiting reaction steps were chosen for further analysis on low-index cobalt surfaces using DFT methods discussed earlier.

4.1. Microkinetic Model

A microkinetic model of FTS on hcp (001) cobalt was developed to identify the rate-limiting reaction steps of C_2 hydrocarbon production. The model is based on the carbide mechanism and was discussed in more detail previously in section 3.1. Due to the complexity of the FTS reaction system, the reaction model only includes carbon chain growth up to C_2H_{2-6} hydrocarbons. **Figure 4.1** illustrates the complexity of the model. The formation of water and carbon dioxide byproducts are also included in the model. The current overall reaction system includes 38 reaction steps and is shown in **Appendix A.1**.
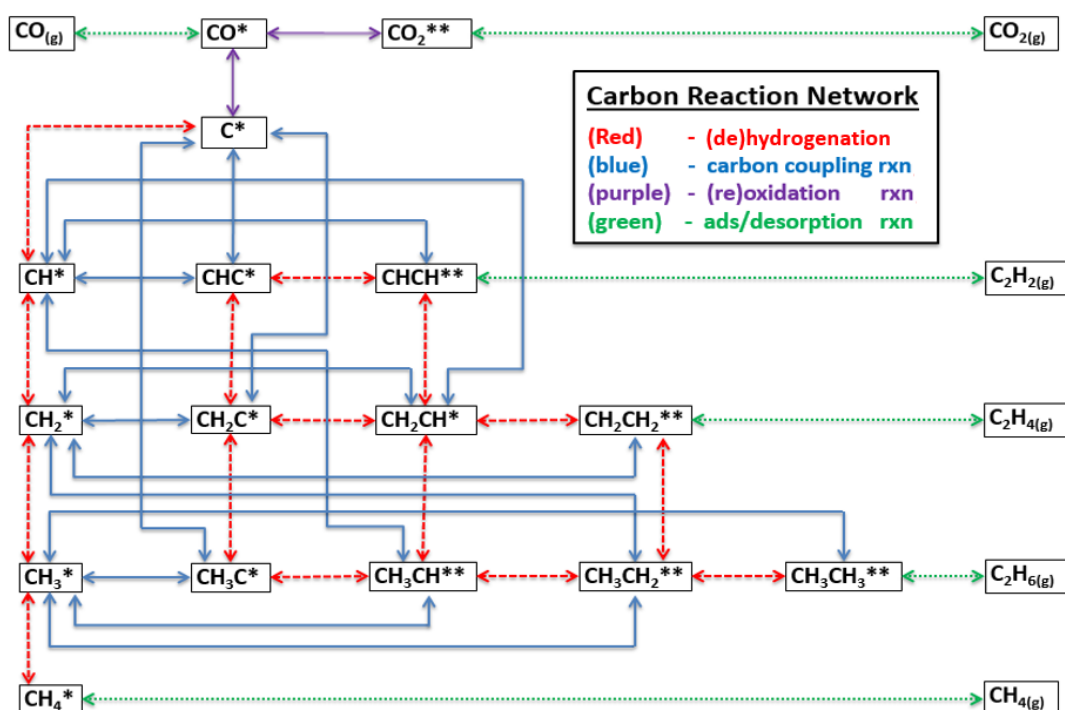

Figure 4.1. Illustration of the microkinetic model used in this study. The lines between each species represents the type of reversible reaction occurring. Reactions involving water and hydroxyl groups are not included in this diagram.

Kinetic data for creation of the base model was obtained from a literature article by Sølvi Storsaetar et al.[15] Their paper used kinetic data from DFT calculations on carbon, oxygen, and hydrogen adsorbates on cobalt to later calculate preexponential factors and activation barriers for the reversible reactions in their models. Rate constants were calculated using the activation energy and pre-exponential data collected from the paper mentioned above using the methods mentioned in section 3.1.1. To tune the model for operating condition analysis, temperature was extrapolated from the literature data and added to the model.

A temperature sensitivity analysis was performed on the microkinetic model for the purpose of finding the optimal operating temperature for chain growth (maximum C_2H_{2-6} production). The model was tested for accuracy by comparing the optimal temperature found to the optimal temperature used in past experiments found in the literature. FTS over cobalt is active from 180^oC to 300^oC. A parametric sweep over this range was performed on the microkinetic model and CH_4 and C_2H_{2-6} steady-state outputs were analyzed. **Figure 3.2** from section 3.1.2 showed a graph of the effect of temperature on the steady-state output of CH_4 and C_2H_{2-6} from the microkinetic model. An optimal temperature for C_2H_{2-6} growth was found to be at 229^oC which falls into the literature range between 210^oC and 240^oC. [13, 59-61, 73]

4.2. Degree of Rate Control

A sensitivity analysis (degree of rate control) was performed on the microkinetic model to identify the rate-limiting reaction steps for hydrocarbon chain growth and byproduct formation. The goal of this analysis was to find which of the many reaction steps of Fischer-Tropsch synthesis has the largest influence (positive or negative) on the production rate of hydrocarbon chains (C_{2+}) in the microkinetic model. Identifying the rate-limiting reaction steps allows us to focus our investigation on one or two reversible reactions out of the 38 reactions in the network.

The sensitivity analysis of the microkinetic model earlier was performed by increasing the reaction rate constant by 1% for each reversible reaction in the model (38 reversible reactions) while holding all other reaction rate constants constant. The effect of increasing the reaction rate constant for all 38 reversible reactions, one at a time, on the rate of chain production was calculated. This was also repeated for different temperatures to observe changes in the rate-limiting reaction steps with temperature. **Figure 4.2** shows the most critical rate-limiting reaction steps for

C_2 chain production from $100^\circ C$ to $600^\circ C$. The other 31 reaction steps had negligible influence on chain production. The three most influential rate-limiting reaction steps found were

$$CO* + H* \longleftrightarrow C* + OH* \quad \text{(promotes chain growth)}$$

$$CH* + CH* \longleftrightarrow CHCH** \quad \text{(promotes chain growth)}$$

$$CH* + H* \longleftrightarrow CH_2* \quad \text{(hinders chain growth)}$$

These three reaction steps had the most influence on C_2 hydrocarbon production at the optimal temperature of $229^\circ C$. The other reactions had an insignificant effect. The hydrogen-assisted CO dissociation reaction ($CO* + H* \longleftrightarrow C* + OH*$) had a profoundly positive influence on C_2 chain growth, however this reaction was found to have a profoundly positive influence on the production of all products including $CH_{4(g)}$ and $CO_{2(g)}$ as shown in **Appendix B.1**. The remaining rate-limiting reaction steps chosen for investigation on various low-index surface facets were CH* coupling ($CH* + CH* \longleftrightarrow CHCH**$) and CH* hydrogenation ($CH* + H* \longleftrightarrow CH_2*$).
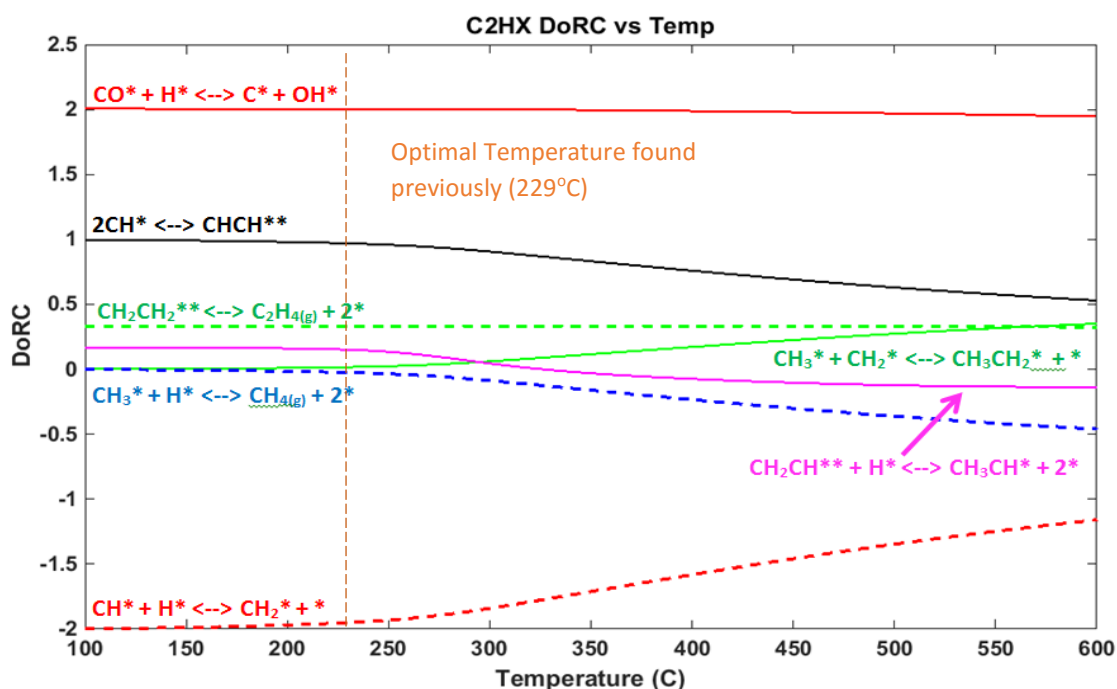
Figure 4.2. Results of the sensitivity analysis over a temperature range between $100^\circ C$ and $600^\circ C$. The analysis was performed over a temperature range to gather insight on the temperature dependence of rate-limiting reaction step influence. Reaction steps with influence between 0.5 and -0.5 were ruled out as insignificant.

Figure 4.2 also looks at the effect of temperature on the influence of reaction steps on C_2 production. As the temperature increases from $240^\circ C$ to $600^\circ C$, the CH* hydrogenation and CH*

coupling reactions become less rate-limiting whereas other reactions such as CH_3^* hydrogenation and methane desorption start to becoming more rate-limiting.

Having narrowed down the complex model to two reaction steps as opposed to 38 reaction steps (**Figure 4.3**) allowed for a computationally expensive investigations (DFT) to be performed on the two rate-limiting reaction steps with respect to different Co surface facets. As can be seen in figure 4.3, hydrogen-assisted CO dissociation still plays a critical role in the reaction mechanims, however it is neglected in the final DFT study due to its positive effect on all products. Future studies may focus on enhancing this reaction for the purpose of increasing CO utilization or turnover frequency. After a CH* monomer is formed from CO dissociation, it can either be hydrogenated to a CH_2^* monomer which is assumed to fully hydrogenate into methane or couple with another CH* monomer to eventually form a C_2 hydrocarbon product.

Figure 4.3. Simplified version of the microkinetic model showing the two rate-limiting reaction steps found by the Degree of Rate Control analysis. The third rate-limiting reaction step, (CO* + H* $\leftarrow\rightarrow$ C* + OH*, is embedded in the CO* activation steps (purple) and contributes to CO utilization.

5. Investigation of Rate-Limiting Reaction Steps on Low-Index Co Surfaces

The structure of a catalyst's surface plays a huge role in the reactivity of chemical reactions[9, 10]. Many surface facets are present on a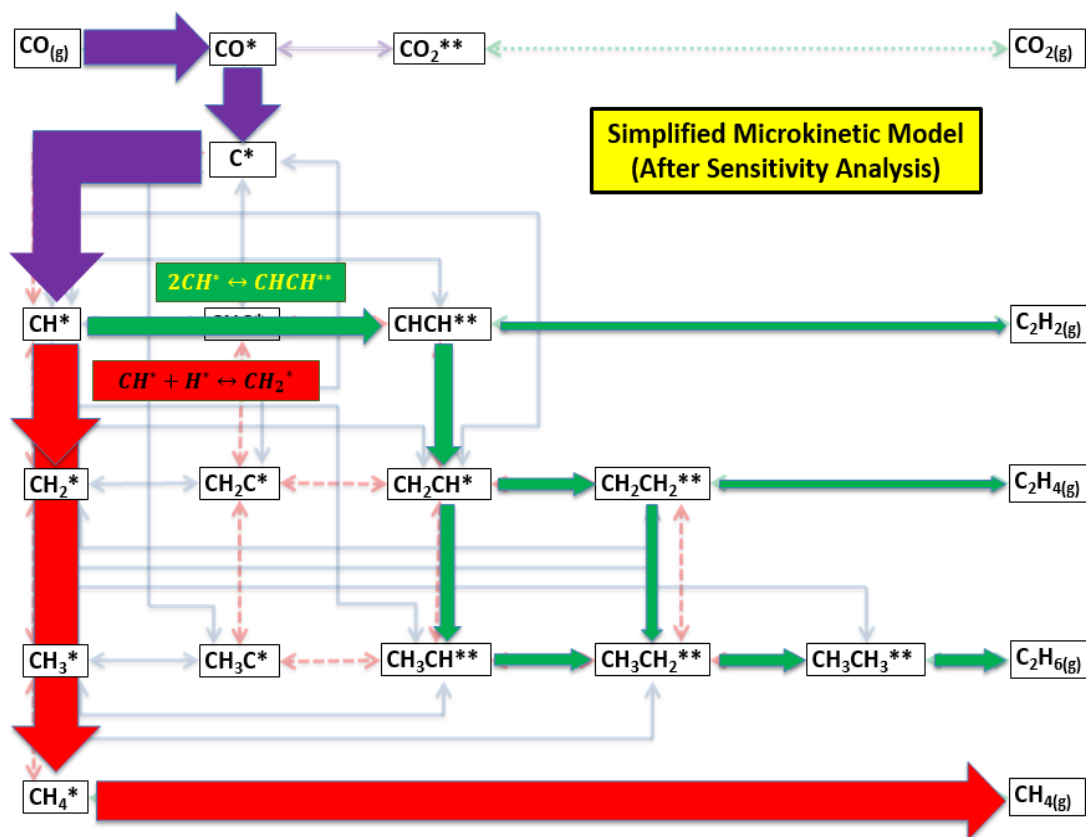 single catalyst's surface in different proportions.[74] Now that the critical steps for chain growth and methane formation have been determined we investigate which facet or surface structure is the most active for these reaction steps. By investigating the rate-limiting reaction steps on these different facets we can determine the structure sensitivity of these reactions and then look for ways to enhance the reaction sites that increases the CH* coupling reaction and/or look for ways to hinder the CH* hydrogenation reaction. The binding energies and activation energies for the two reactions were calculated using DFT on eight specific low-index hcp Co facets. After the initial and final states of the rate-limiting reaction steps (the adsorption sites of H*, CH*, CH_2*, and C_2H_2**) have been determined, a nudge-elastic band (NEB) calculation is performed. The NEB calculation is used to find the energy barriers of formation (Ea_f) and decomposition (Ea_d) (interchangeable with forward activation barrier (Ea_f) and backwards activation barrier (Ea_b)) as well as the reaction energies (ΔE_r).

5.1. CH* Coupling Reaction (CH* + CH* ←→ C_2H_2**)

5.1.1. Co (001) and (110) and other low-index hcp facets

The initial state for the CH* coupling reaction on Co (001) (CH* + CH*) was found with both CH* monomers sitting at a 4-fold site (E_{ads}= -12.5 eV) and the final state (C_2H_2**) was found occupying a bridge site between a 3-fold and 4-fold site (E_{ads} = -2.3 eV) (**Figure 5.1**). The initial/final state configurations and adsorption energies for the CH* coupling reaction on hcp Co (001) was in agreement with a DFT study from the literature[2]. The initial state and final state configurations for the CH* coupling reaction on Co (110) are shown in **Figure 5.2**. The CH* monomers in the initial state had the strongest binding energy (E_{ads} = -13.0 eV) when located on a valley top site as shown in the figure. The C_2H_2** species was found to prefer a valley bridge site (E_{ads} = -2.0 eV).
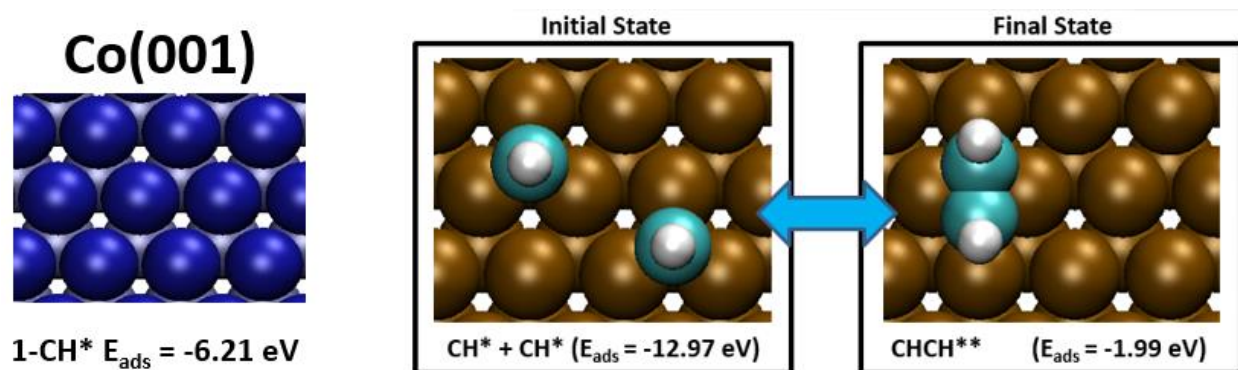
Figure 5.1. Initial and final state positions for CH* + CH* ⟷ C_2H_2** reaction on hcp Co (001). The adsorption energy for a single CH* monomer at its most stable position (4-fold site) was found to be -6.21 eV. The initial state (CH* + CH*) adsorption energy was found to be -12.97 eV with both CH* monomers occupying 4-fold sites. The final state (C_2H_2**) adsorption energy was found to be -1.99 eV occupying a bridge site.
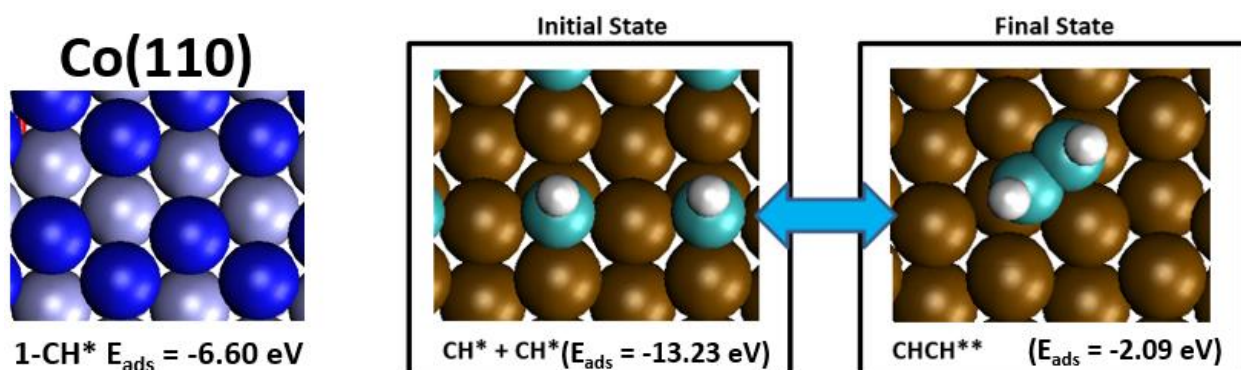
Figure 5.2. Initial and final state positions for CH* + CH* ⟷ C_2H_2** reaction on hcp Co(110). The adsorption energy for a single CH* monomer at its most stable position (trench top-site) was found to be -6.60 eV. The initial state (CH* + CH*) adsorption energy was found to be -13.23 eV with both CH* monomers occupying trench top-sites. The final state (C_2H_2**) adsorption energy was found to be -2.09 eV occupying a bridge site inside the trench.

The CH* coupling reaction was also investigated on six other low-index hcp Co surfaces (100A, 100B, 101A, 101B, 111A, and 111B). The initial and final state configurations of the CH* coupling reaction on all studied surfaces are shown in **Appendix B.2** and the corresponding adsorption energies for these states are listed in a table in **Appendix B.4.** The initial state adsorption energies calculated were -11.8, -14.0, -12.8 , and -12.9 eV for the Co (101)A, (101)B, (111)A, and (111)B surfaces, respectively. Final state adsorption energies had a smaller range and were calculated to be -1.8, -2.6, -2.0, and -2.2 eV for the same respective surfaces.

The low-index surfaces facets modeled in this study exhibited trench-like surface characteristics with exception of Co (001) and Co (101)B which could be categorized as "flat" surfaces. The initial and final states for the rate-limiting reaction steps followed a trend with CH*

monomers preferring to occupy sites in the valleys of "trench-like" surfaces. At the low coverage of 2/8 ML (2/9 ML for Co (001)), CH* monomers shared the same type of active sites. The C_2H_2** species showed site preferences that were similar or in close proximity to the site preferences of the CH* monomers with an exception on the (101)A and (101)B facets.

The adsorption energies for single CH* monomers varied little between the six surfaces (-6.1 to -6.6 eV). When a second CH* monomer was added to the models (CH* coupling initial state) the overall adsorption energy for the two monomers was more negative than two single CH* adsorption energies combined. This was the case for all of the surfaces except the Co (101)A surface which experienced a less negative overall adsorption energy at a higher CH* coverage (2/8 ML) suggesting a repulsive interaction of 0.4 eV between the two adsorbates. The other surfaces had CH* monomers experiencing an attractive interaction at a higher coverage (2/8 ML) ranging from 0.1 to 1.2 eV and stabilized at higher coverages of 2/9 and 2/8 ML. This is likely due to a more optimized distance between the two adsorbates on the Co (101)A surface where the CH-CH distance was 5.1 Å but 4.3 Å on average for the other surfaces. The slight change in binding configuration with coverage is also seen in the different Co-C bond length. CH* monomers on all surfaces experienced an increase in Co-C bond length by 0.1 Å except for the Co (101)A surface which experiences a shortening in Co-C bond length by 0.1 Å.

5.1.2. Activation Energies

After finding the initial and final states for the rate-limiting reaction steps, a nudge-elastic band (NEB) calculation was performed to find the formation and dissociation energy barriers for the reaction on Co (001), Co (110), and Co (101)B. The formation activation barriers for the CH* coupling reaction on the (001) and (110) surfaces came within a margin of error of each other with the reaction having a 1.08 eV formation barrier on Co (001) and a 1.01 eV on Co (110). The formation activation barrier on the Co (101)B surface was slightly higher at 1.25 eV. The reaction pathway data is shown in **Appendix B.5**. Although the Co (001) and (110) surfaces are very different structure-wise (Co (001) can be considered a flat facet whereas Co (110) exhibits defined trench like structures with a repeating and parallel zig-zag pattern) the formation barriers for CH* coupling are almost identical. A comparison of the reaction energy diagrams for Co (001), Co (110), and Co (101)B is shown in **Figure 5.3**. The dissociation barriers and reaction energies are dramatically different between the Co (001) and Co (110)/Co (101)B surfaces.
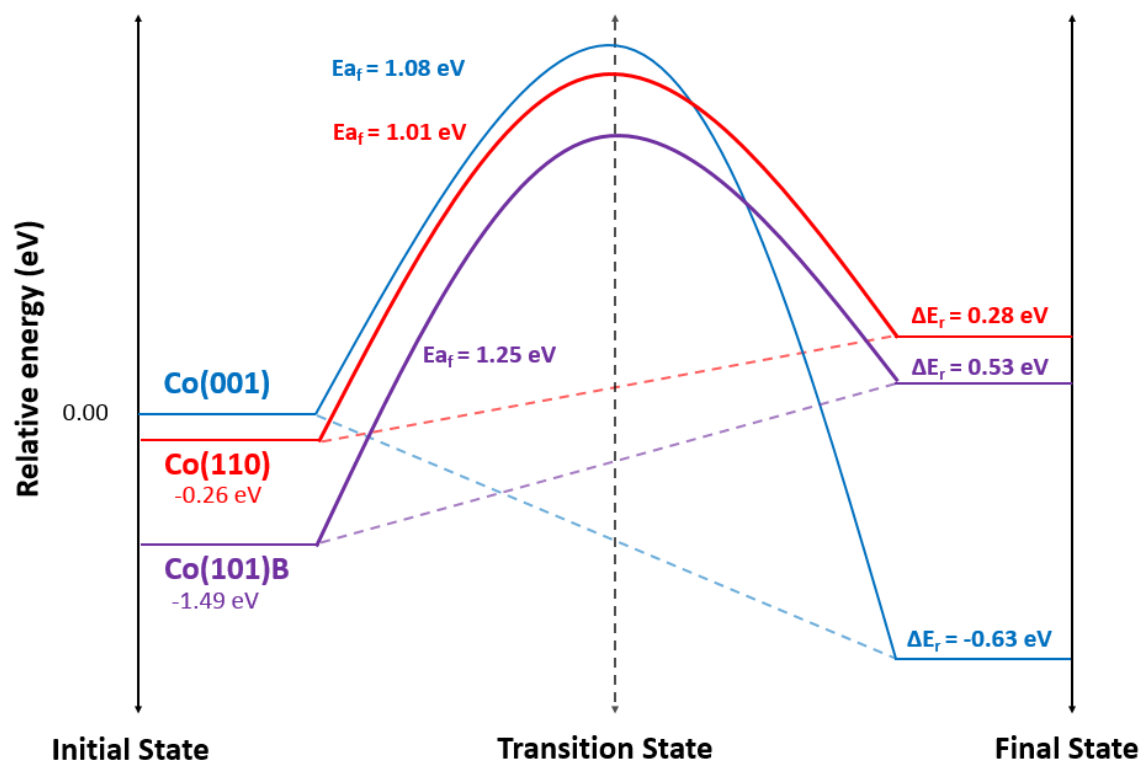
Figure 5.3. Reaction energy diagram relative to the adsorption energy of CH* + CH* on Co (001) (set to zero as the reference point). The formation activation barriers (Ea$_f$), initial state adsorption energies with respect to Co (001), and reaction energies (ΔE$_r$) are shown. The formation activation barriers differ at most by 0.24 eV (between Co (110) and Co (101)B.

The CH* coupling reaction was found to have an exothermic reaction energy of -0.63 eV on a Co (001) surface whereas the reaction energy was found to be an endothermic 0.28 eV on Co (110) and 0.53 eV on Co (101)B. A trend was noticed in the forward activation barriers relative to the binding energies of the CH* + CH* monomers for the three surfaces. **Appendix B.6** shows a graph of activation barriers vs. binding energy. The activation barriers were shown to rise 0.23 eV per eV of CH* binding energy. The results pertaining to the Co (001) surface are a bit higher than those found in the literature, however due to the low coverage and size of the modeled slabs, higher barrier and reaction energies are to be expected. When surface diffusion between the two CH* monomers is not taken into account on the Co (001) surface, the formation barrier and reaction energies effectively become 0.68 eV and -0.96 eV, respectively. **Figure 5.4** shows the reaction energy diagram for Co (001). The purple arrows indicate the formation activation barrier and reaction energy when the CH* monomers occupy adjacent 4-fold active sites. These two values match up closely with a study[2] that looked at the CH* coupling reaction at a higher coverage

(smaller surface model) that found an initial state where CH* monomers occupied adjacent 4-fold sites.
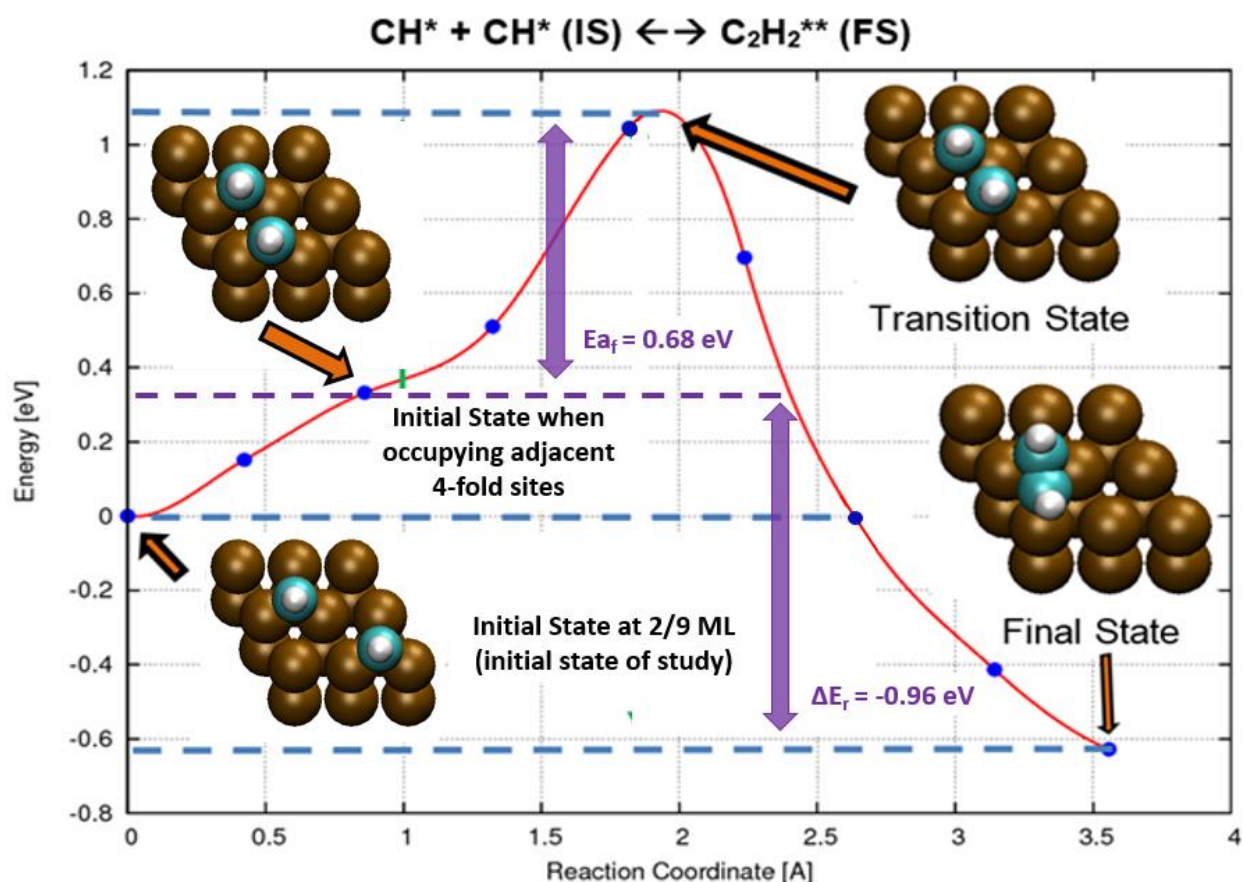
Figure 5.4. Reaction energy diagram for CH* + CH* ⟷ C_2H_2** on Co (001). The formation activation barrier and reaction energy when looking at an initial state with two CH* monomer occupying adjacent 4-fold sites are similar to a study performed with a 0.5 ML coverage and similar initial state configuration[2].

5.2.   CH* Hydrogenation

5.2.1. Co (001) and (110) and other low-index hcp facets

The initial state for the CH* hydrogenation reaction on Co (001) was found with a CH* monomer sitting in a 4-fold site and an H* radical occupying a 3-fold site (E_{ads}= -9.0 eV). The final state (CH_2*) was found occupying a 4-fold site (E_{ads} = -2.3 eV) (**Figure 5.5**). Initial/final state configurations and adsorption energies for the CH* hydrogenation reaction on hcp Co (001) was also in agreement with the literature[2].
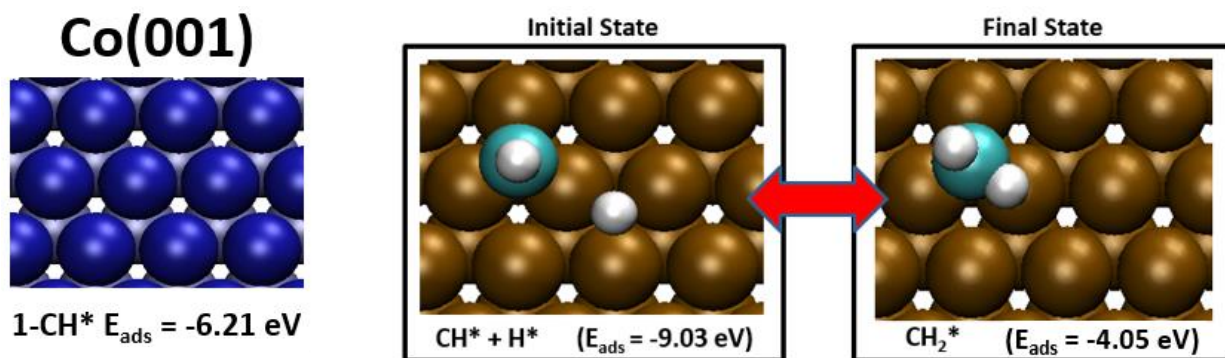
Figure 5.5. Initial and final state positions for CH* + H* ←→ CH$_2$* reaction on hcp Co(001). The initial state (CH* + H*) adsorption energy was found to be -9.03 eV with a CH* monomers occupying a 4-fold site and an H* monomer occupying a 3-fold site. The final state (CH$_2$*) adsorption energy was found to be -4.05 eV occupying a 4-fold site.

Initial state and final state configurations for the CH* hydrogenation reaction on Co (110) are shown in **Figure 5.6.** The CH* monomer in the initial state had the strongest binding energy when located on a trench top-site like the CH* monomer from the CH* coupling reaction initial state. H* preferred to occupy a bridge-site located on the wall of the Co(110) slab and the total binding energy for the initial state configuration was found to be -9.1 eV. The CH$_2$* species for the final state preferred the same location as the CH* monomer in the initial state (E$_{ads}$ = -4.1 eV).
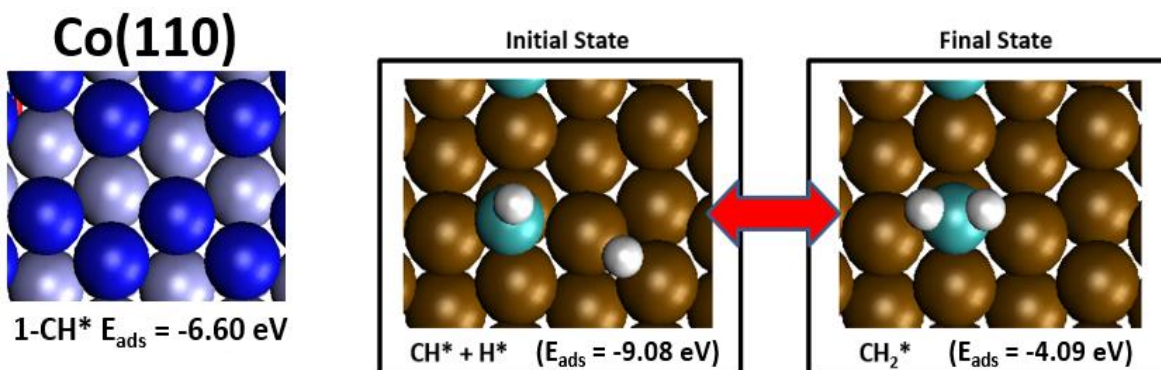
Figure 5.6. Initial and final state positions for CH* + H* ←→ CH$_2$* reaction on hcp Co (001). The initial state (CH* + H*) adsorption energy was found to be -9.08 eV with a CH* monomers occupying a trench top-site and an H* monomer occupying a wall bridge-site. The final state (CH$_2$*) adsorption energy was found to be -4.09 eV occupying a trench top-site.

The CH* hydrogenation reaction was also investigated on the six other low-index hcp Co surfaces. The initial and final state configurations of the CH* hydrogenation reaction and corresponding adsorption energies for these states are shown in **Appendix B.3** and **Appendix B.4**

for all surfaces investigated in this study. All initial state adsorption energies fell between -9.9 and -8.9 eV, with Co (101)B and Co (111)A showing the strongest and weakest binding energies, respectively. Final state adsorption energies fell between -4.4 and -4.0 eV, with CH_2* having the strongest and weakest binding energy on the Co (101)B and Co (001), respectively.

All surfaces, excluding (111)B, showed attractive interactions between the CH* and H* monomers. Although surface coverage remained low at 2/8 ML, the distances between the CH* monomers and the H* radicals was less than 2.7 Å (diameter of a cobalt atom). The adsorption energies for the CH* hydrogenation species differed at most by 0.6 eV with the 3-fold and 5-fold sites on the (101)B surface being the strongest active site configuration of the six surfaces. The bond length between CH* monomers and their nearest cobalt atom on the surface did not change in the presence of hydrogen on any of the surfaces. This was also true for the bond lengths between H* radicals and their nearest cobalt neighbors.

5.2.2. Activation Energies

A NEB calculation was performed using the initial and final states of the CH* hydrogenation reaction from the Co (001), (110), (111)A, and (101)B surface models. For the Co (001) surface a formation barrier of 0.3 eV was found for the CH* hydrogenation reaction along with an endothermic reaction energy of 0.05 eV. **Figure 5.7** compares the reaction energy diagrams for the four surfaces mentioned. Reaction pathway data included in **Appendix B.5.** The formation barriers vary widely between the four surfaces with the lowest formation barrier found on Co (001) at 0.29 eV and the highest formation barrier found on Co (101)B at 0.96 eV. Unlike the CH* coupling reaction formation barriers on Co (001) and (110) that only differed at most by 0.24 eV, the formation barriers for CH* hydrogenation showed a large variation between the four surfaces with a minimal difference of over 1.2 eV and a maximum difference of 0.96 eV.
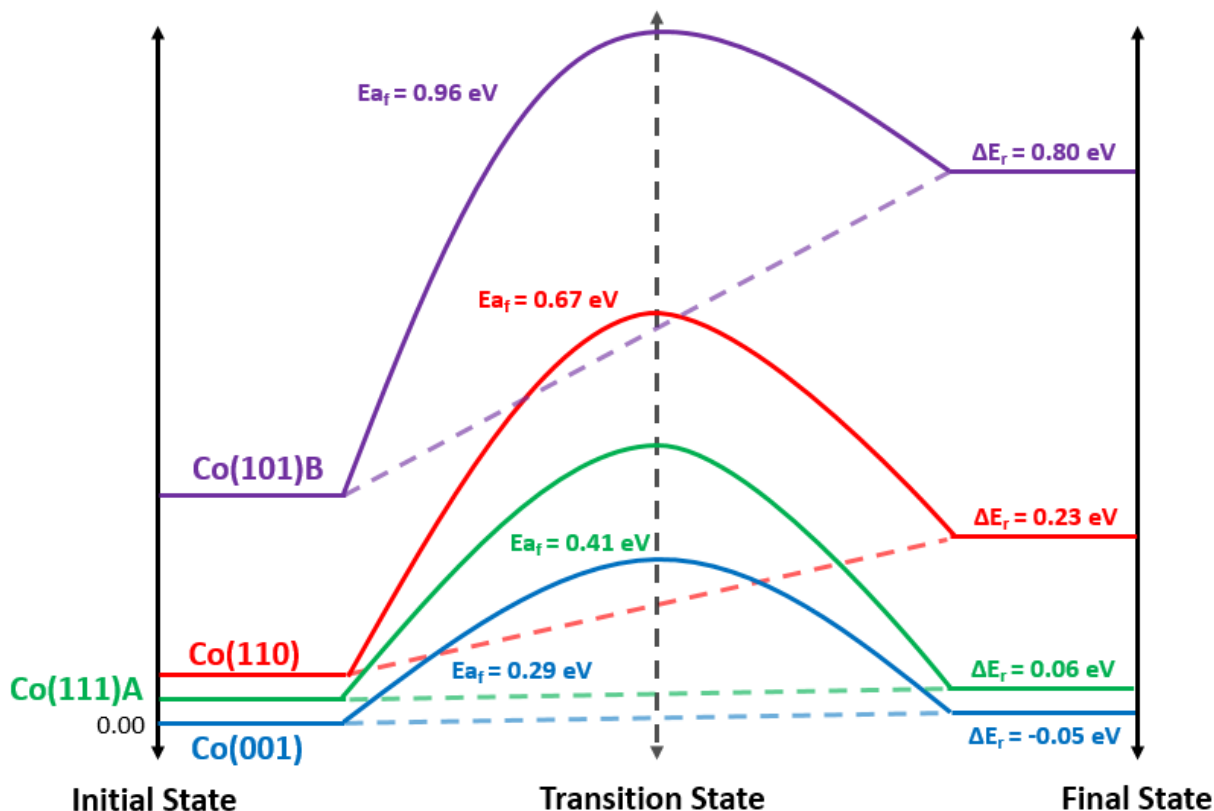
Figure 5.7. Reaction energy diagram relative to the adsorption energy of CH* + H* on Co (001) (set to zero as the reference point). The formation activation barriers (Ea$_f$), initial state adsorption energies with respect to Co (001), and reaction energies (ΔE_r) are shown. The formation activation barriers widely differ between the surfaces with the largest difference of 0.63 eV between Co (001) and Co (101)B.

As with the CH* coupling reaction, the low coverage conditions deviated the results from those found in the literature. Literature results with a 0.5 ML coverage show the formation activation barrier for CH* hydrogenation ranging between 0.37 eV and 0.66 eV[1, 2, 8, 15, 19, 64]. The formation activation barrier for CH* hydrogenation Co (001) calculated in this study was 0.08 eV lower than a barrier found in one of the literature articles[19] that included a 0.5 ML of CO. A replication of this study at a higher coverage would be beneficial for comparing values to the literature.

6. Temperature Swing Reactor Optimization

This project was part of a collaborative effort between industry and academia to move the FTS process onto a micro reactor platform. The team has built a test platform to test different catalyst and process operating conditions as well as designed catalyst deposition methods. A novel non-steady state temperature swing reactor has been designed and is currently under development. The goal of this reactor is to minimize the amount of large chain hydrocarbons (C$_{8+}$) produced from

FTS by performing an acute temperature increase when the FT catalysts reaches maximum coverage of the desired chain. The time for maximum coverage to be reached is determined by an on-catalyst residence time specific to a desired alkane. After the temperature has reached a set maximum level, when the hydrocarbon chain desorption rate is 100 times larger than the chain production rate, the system is lowered back to optimal chain growth conditions. **Figure 6.1** illustrates the release of hydrocarbon chains during each temperature cycle from the lower temperature (T_L) to the higher temperature (T_H). The spike in temperature is performed when max surface coverage is reached (t_{max}). These three parameters were calculated using another microkinetic model from the literature[16] (Model details in **Appendix C.1** and **C.2**) to determine if these temperatures and timing could be feasibly achieved for producing C_8 hydrocarbons with current reactor technology.
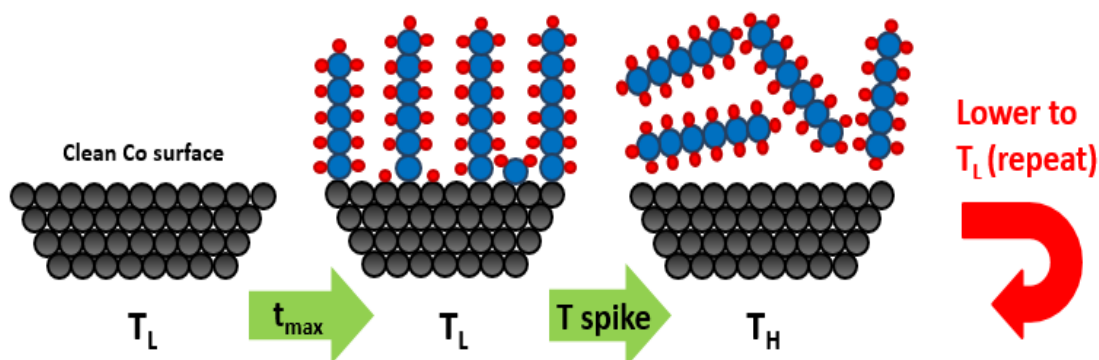
Figure 6.1. Illustration of chains growing on a Co surface to a max coverage at temperature (T_L) before being spiked to a hotter temperature (T_H) and releasing chains of desired length. The plan is to repeat this cycle at intervals that maximize selectivity towards hydrocarbon chains of desired length.

6.1. Temperature Swing

A temperature sweep of C_{2-9} hydrocarbons on a Co surface was performed on the microkinetic model to find the maximum coverage of C_{2-9} hydrocarbons between 150°C and 400°C. **Figure 6.2** and **Figure 6.3** shows the maximum coverage achieved for C_{2-9} hydrocarbons when the model was ran at the specified temperatures. The black line in the figure represents the maximum coverage of total C_{2-9} hydrocarbons during a run at the specified temperature. They achieve a maximum coverage of 230°C. This is also the temperature that was found to have the highest hydrocarbon chain production rate from the previous microkinetic model study.
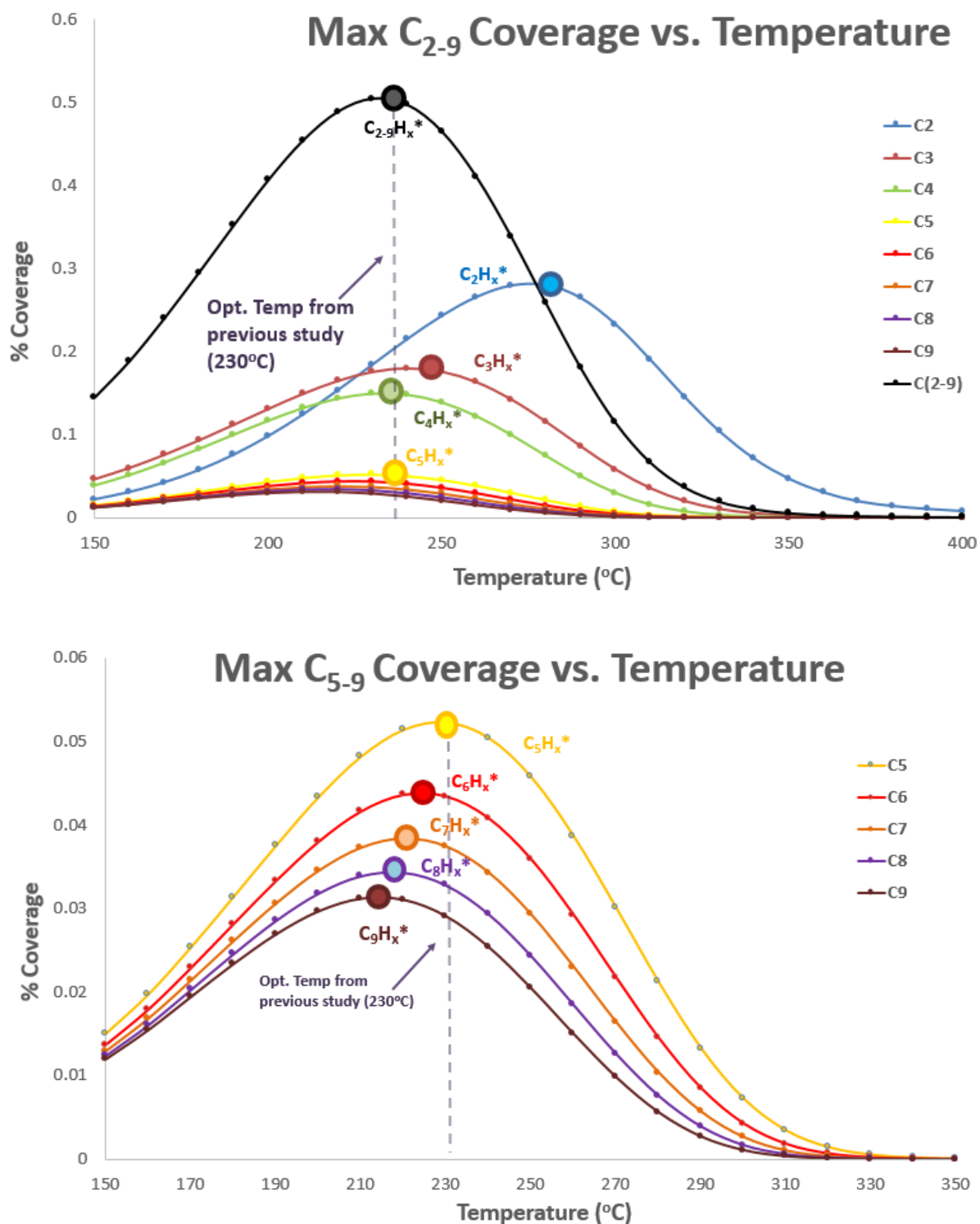
Figure 6.2. Modeled coverage of C_{2-9} hydrocarbon chains on a Co catalysts between 150°C and 400°C. The dashed black line represents the optimal temperature found previously in this study. The (lower) graph is blown up to show C_{5-9} chains. It can be seen that the maximum coverage point appears at lower temperatures for higher chain lengths.

The C_8 hydrocarbon chain reached a maximum coverage at 220°C. **Figure 6.3** shows the temperature where each C_{2-9} hydrocarbon chain achieves its maximum surface coverage. Using the approximated trend from **Figure 6.3**, a maximum coverage for C_{9+} hydrocarbons could potentially be found.
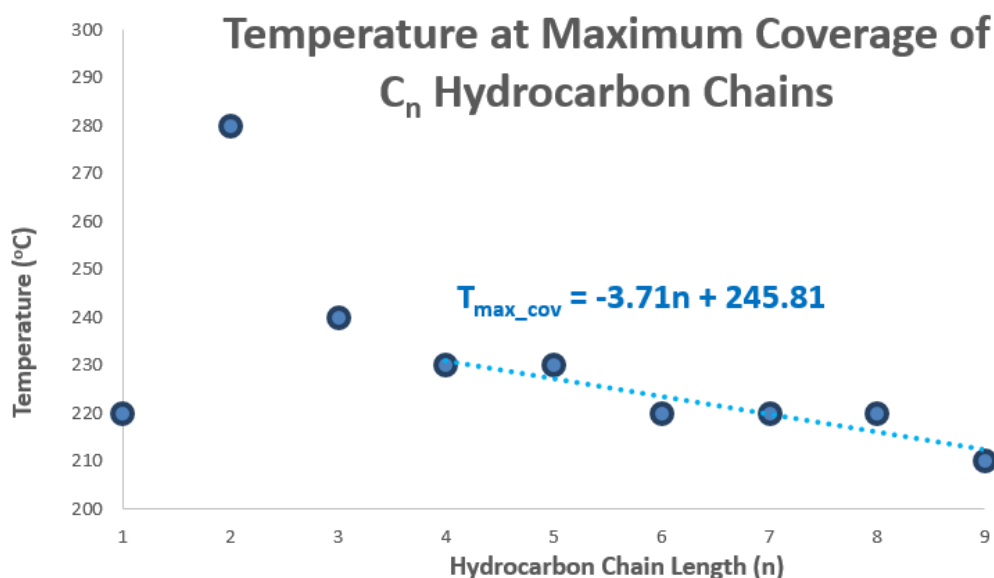
Figure 6.3. Graph showing the temperature where hydrocarbons of chain length (n) achieve maximum surface coverage. The temperature for maximum coverage of C_{9+} hydrocarbons could potentially be extrapolated from this data if the trend seen for C_{4+} hydrocarbons holds true.

From the lower temperature where chain growth is maximized, the temperature swing reactor will undergo an almost instantaneous temperature increase (limited by catalysts thermal conductivity). The upper limit of the temperature will be where the hydrocarbon chain desorption rate is 100 times larger than the chain production rate. At this higher temperature, all hydrocarbon chains that populated the catalysts surface at the lower temperature will theoretically be released from the surface. **Figure 6.4** shows a graph of the chain growth probability of the hydrocarbon chains from 100°C to 550°C as determined by a temperature sweep of the microkinetic model. At 450°C, the microkinetic model showed a chain termination probability of 99%. It should be noted that the turnover frequency of CO is extremely low below 200°C. Even though the chain growth probability is high below these temperatures the overall FT reaction rates are extremely slow.
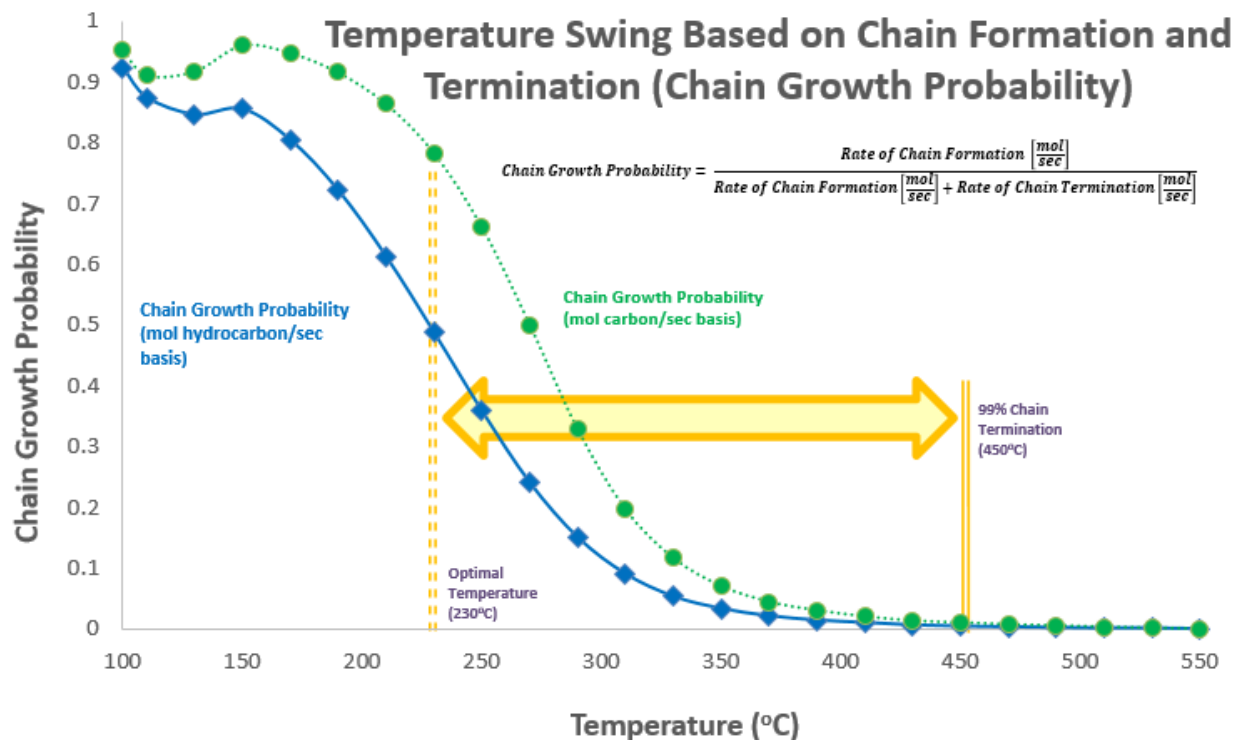
Figure 6.4. Graph of chain growth probability versus temperature. The chain formation rate is represented by moles of hydrocarbons formed per sec (blue) and moles of chain carbon content per sec (green). The rate of chain termination becomes 100 times that of chain formation at 450ºC. At this temperature, almost all chains on the catalysts surface will be terminated and desorb as hydrocarbons of the same length as when they were on the surface.

6.2. Time to Reach Max Coverage

The temperature swing reactor will run at a temperature that allows for maximum chain growth of a desired hydrocarbon chain on the catalyst surface. At a certain length of run time (starting from a clean surface), when the coverage of the hydrocarbon chain of desired length (n) has reached its maximum, the reactor will be spiked to the higher temperature range (450ºC) to release the chains as gaseous product. This will minimize the amount of paraffin wax (chains larger than the desired length) in the product stream.

The microkinetic model used to determine the magnitude of the temperature swing was used to approximate the time required to populate a catalysts surface with C_{2-9} hydrocarbon chains. The same reaction kinetics and reactor operating conditions from the previous analysis and a temperature of 220ºC was used for the time analysis. **Figure 6.5.** shows the coverage of C_{2-9} hydrocarbon chains over time starting with a clean catalyst surface. Due to the dependence of C_n

hydrocarbon coupling on the formation of C_{n+1} hydrocarbon chains, the time required for them to reach their maximum coverage (black circles) and steady-state increases with chain length.
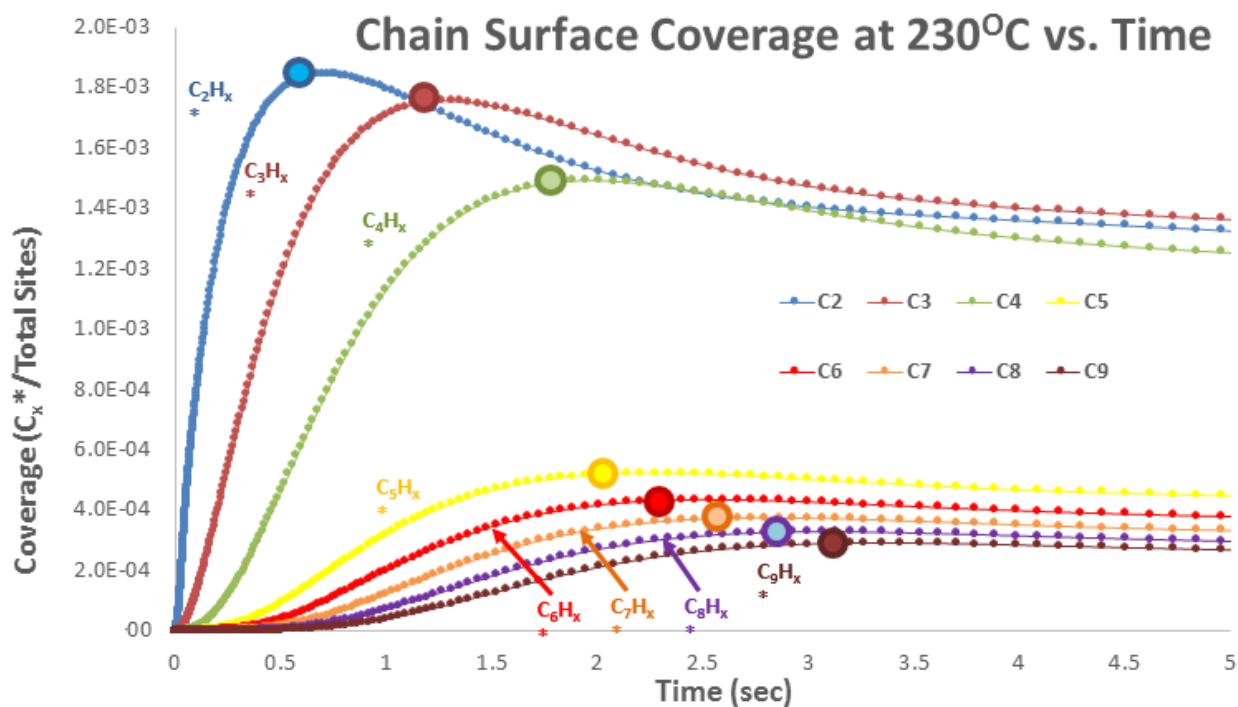
Figure 6.5. Graph showing the coverage C_{2-9} versus time at the optimal C_{2-9} coverage temperature of 230°C. Circles represent the time required for each species to reach maximum coverage. The larger hydrocarbon chains take longer time to reach maximum coverage before eventually reaching steady state. C_8 maximum coverage time was found at 3.0 seconds

Figure 6.6 shows how the maximum coverage time changes with chain length. For C_{2-4} hydrocarbon chains, a linear relationship forms for maximum coverage time vs chain length. This trend abruptly changes at C_4 where a new linear relationship is found for C_{4-9} hydrocarbon chains. Due to the close fit of the linear trend line for C_{4-9} hydrocarbon chains, the resulting equation could be used to estimate the maximum coverage time for $n \geq 4$ hydrocarbon chains assuming the linear relationship holds for hydrocarbon chains with $n > 9$.
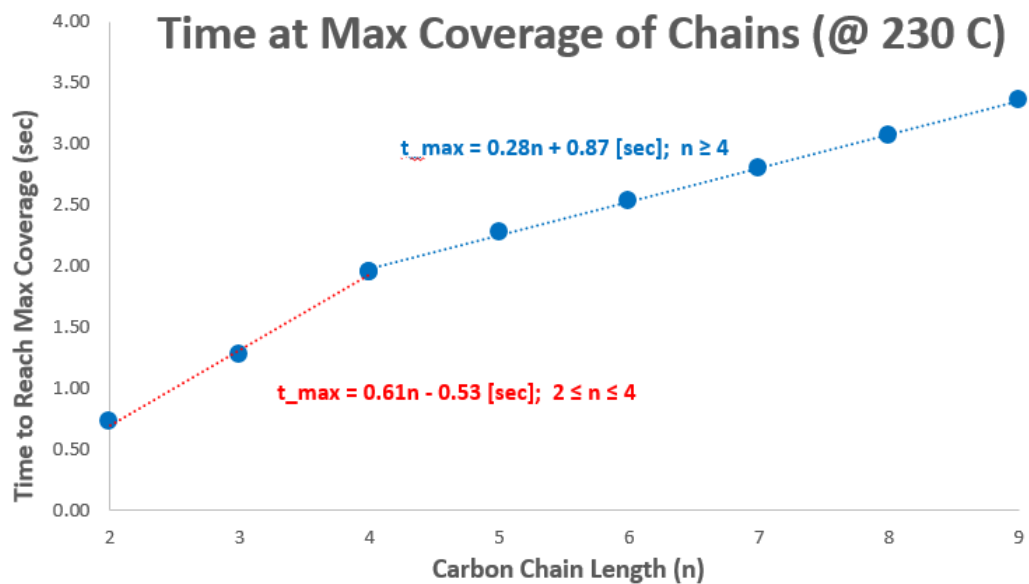
Figure 6.6. graph of the time required for chain length (n) hydrocarbons to reach maximum coverage at 230°C. The trend shown for C_{4+} could be extrapolated to find maximum coverage times for larger hydrocarbon products. Once again, C_8 is shown to reach a maximum coverage at around 3.0 seconds

When the temperature is decreased to 220°C (temperature where C_8 reaches is its maximum surface coverage) the time for the C_8 hydrocarbon chains to reach maximum coverage on the surface is found to be approximately 6.00 seconds as shown in **Figure 6.7**.
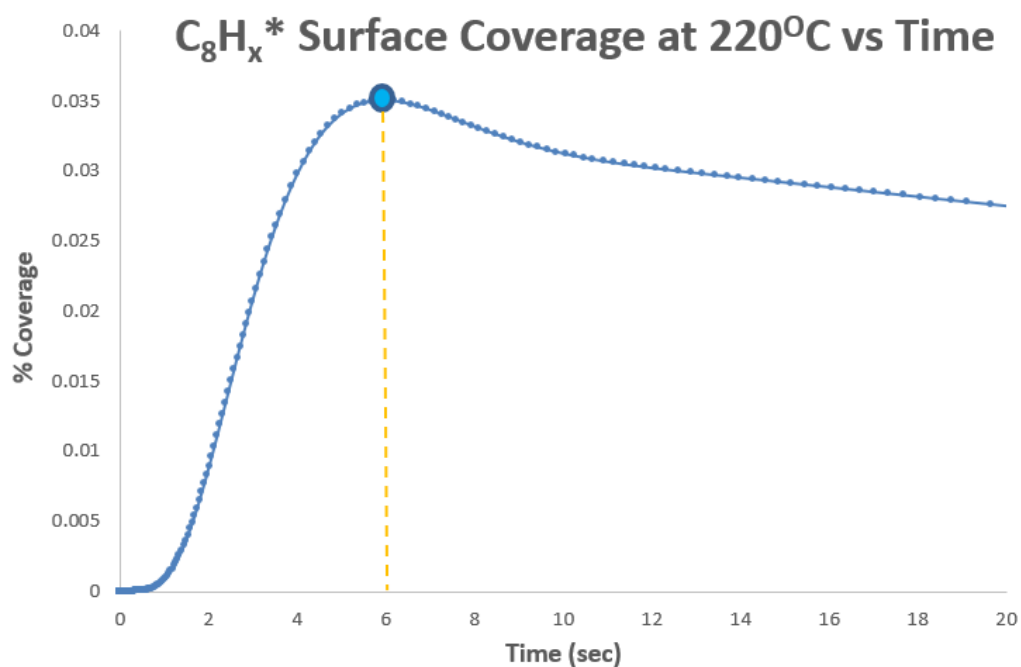
Figure 6.7. Graph of C_8 surface coverage over time starting with a clean Co surface where C_8 reaches a maximum coverage vs temperature (220°C). The circle represents the maximum coverage of C_8 reached at 6.0 seconds.

7. Conclusion

The primary objective of this study was to investigate the effect of catalyst surface structure on the rate-limiting reaction steps of FT chain growth relative to the commonly exposed hcp (001) facet. Past studies have looked at the effect of different surface structures such as steps and kinks on various FT reactions but very few studies have looked at how different surface facets influence FT reaction kinetics. The rate-limiting reactions steps determined in this study by performing a degree of rate control analysis on a microkinetic model previously established in the literature allowed for the complex FT reaction network to be narrowed down to two critical reaction steps: CH* coupling (CH* + CH*) and CH* hydrogenation (CH* + H*). This is a powerful tool to help determining critical reaction steps to help focus a detailed study on different catalyst structure for a complex reaction mechanism to a handful of reactions. A similar approach could also be used to identify descriptors for a complex reaction network for computational catalyst and alloy screening. These two reaction steps were then studied on four different low-index hcp surface facets of cobalt to investigate the effect of the facet structural properties on these reaction's formation barriers and reaction energies. NEB calculations involving the CH* coupling reaction showed that the surface facets (001) and (110) had negligible influence on the formation barrier even though the two surfaces are structurally dissimilar. This was not the case for the CH* hydrogenation reaction which showed a wide range of formation barrier energies over the four modeled surfaces (Co (001), Co (110), Co (111)A, and Co (101)B). Based on the results of this study, it appears that the catalyst facet in cobalt catalyzed FTS has little effect on the formation barrier of CH* coupling but a substantial influence on the formation barrier of CH* hydrogenation. It is possible that the structural influence of cobalt catalyst on FT chain formation is induced not by the alteration of CH* coupling kinetics but the hindrance of CH* hydrogenation that potentially leads to methane formation.

A secondary objective of this study was part of a collaborative effort between industry and academia to move the FTS process onto a micro reactor platform. A novel non-steady state temperature swing reactor has been designed and is currently under development. The goal of this reactor is to minimize the amount of large chain hydrocarbons (C_{8+}) produced from FTS by performing an acute temperature increase when the FT catalysts reaches maximum coverage of the desired chain. The time for maximum coverage to be reached for C_8 was calculated to be 6

seconds while the reactor is maintained at an optimal C_8 coverage temperature of 220°C. The higher temperature for the acute temperature swing was calculated to be 450°C when that rate of chain termination was calculated to occur 100 times faster than the chain formation rate. These conditions serve as a starting point for testing the temperature swing reactor when it reaches the testing phase. A comparison between theoretical and experimental results can be made at that time.

8. Recommendation for Future Work

Although the results presented here have demonstrated the effects of different low-index hcp surface facets on FT rate-limiting reaction steps, it could be further developed in a number of ways.

The DFT investigation performed in this study was done so under low coverage conditions (between 1/9 and 2/8 ML). A further investigation of the rate-limiting steps under higher coverage conditions (between 1/2 and 1 ML) would be beneficial for calculating reaction barriers and energies under more realistic reaction coverages. The population of surface species on a Co surface during FTS has been observed in some cases to mainly consist of CO* and H* surface adsorbates. The coverages of these species could also be included in later investigations of low-index hcp facets.

There are many possible hcp surface facets beyond those investigated in this study. It has been shown in the literature and this study that crucial FT reaction steps are profoundly affected by the surface structure of the catalyst. The two other low-index surfaces, (100)A and (100)B, should be investigated along with high-index surface facets such as (108) and (411) to expand the search for the cobalt hcp facet that maximizes the height of the CH* hydrogenation activation barrier and minimizes the CH* coupling activation barrier.

The surface facet with the highest activation barrier for CH* hydrogenation was found to be (101)B in this study (out of the six investigated surfaces). The next step would be to experimentally prove the findings in this study by developing different catalyst that maximize the surface density of the desired facets and then experimentally observing their effect on carbon species hydrogenation.

Appendix A.

A.1. Microkinetic Model Reaction

Table 4.1. List of reactions involved in the microkinetic model. Theta represents a free active site.

Rxn #	Reaction	Reaction Equation
1	CO (g) + theta <--> CO*	$k_{1f}P_{CO}\theta_* - k_{1r}\theta_{CO}$
2	CO* + theta <-> C* + O*	$k_{2f}\theta_{CO}\theta_* - k_{2r}\theta_C\theta_O$
3	CO* + H* <--> C* + OH*	$k_{3f}\theta_{CO}\theta_H - k_{3r}\theta_C\theta_{OH}$
4	H₂ (g) + 2-theta <--> 2-H*	$k_{4f}P_{H_2}\theta_*^2 - k_{4r}\theta_H^2$
5	H* + OH* <--> H₂O* + theta	$k_{5f}\theta_H\theta_{OH} - k_{5r}\theta_{H_2O}\theta_*$
6	H₂O* <--> H₂O (g) + theta	$k_{6f}\theta_{H_2O} - k_{6r}P_{H_2O}\theta_*$
7	O* + H* <--> OH* + theta	$k_{7f}\theta_O\theta_H - k_{7r}\theta_{OH}\theta_*$
8	CO* + O* <--> CO₂**	$k_{8f}\theta_{CO}\theta_O - k_{5r}\theta_{CO_2}$
9	CO₂** <--> CO₂ (g) + 2-theta	$k_{9f}\theta_{CO_2} - k_{9r}P_{CO_2}\theta_*^2$
10	CO* + H* <--> CH* + O*	$k_{10f}\theta_{CO}\theta_H - k_{10r}\theta_{CH}\theta_O$
11	C* + H* <--> CH* + theta	$k_{11f}\theta_C\theta_H - k_{11r}\theta_{CH}\theta_*$
12	CH* + H* <--> CH₂* + theta	$k_{12f}\theta_{CH}\theta_H - k_{12r}\theta_{CH_2}\theta_*$
13	CH₂* + H* <--> CH₃* + theta	$k_{13f}\theta_{CH_2}\theta_H - k_{13r}\theta_{CH_3}\theta_*$
14	CH₃* + H* <--> CH₄ (g) + 2-theta	$k_{14f}\theta_{CH_3}\theta_H - k_{12r}P_{CH_4}\theta_*^2$
15	CH₄ (g) + theta <--> CH₄*	$k_{15f}P_{CH_4}\theta_* - k_{15r}\theta_{CH_4}$
16	CH₃* + C* <--> CH₃C* + theta	$k_{16f}\theta_{CH_3}\theta_C - k_{16r}\theta_{CH_3C}\theta_*$
17	CH₃* + CH* <--> CH₃CH* + theta	$k_{17f}\theta_{CH_3}\theta_{CH} - k_{17r}\theta_{CH_3CH}\theta_*$
18	CH₃* + CH₂* <--> CH₃CH₂* + theta	$k_{18f}\theta_{CH_3}\theta_{CH_2} - k_{18r}\theta_{CH_3CH_2}\theta_*$
19	2-CH₃* <--> CH₃CH₃**	$k_{19f}\theta_{CH_3}^2 - k_{19r}\theta_{CH_3CH_3}$
20	CH₃CH₃** <--> C₂H₆ (g) + 2-theta	$k_{20f}\theta_{CH_3CH_3} - k_{20r}P_{C_2H_6}\theta_*^2$
21	CH₂* + C* <--> CH₂C**	$k_{21f}\theta_{CH_2}\theta_C - k_{21r}\theta_{CH_2C}$
22	CH₂* + CH* <--> CH₂CH**	$k_{22f}\theta_{CH_2}\theta_{CH} - k_{22r}\theta_{CH_2CH}$
23	2-CH₂* <--> CH₂CH₂**	$k_{23f}\theta_{CH_2}^2 - k_{23r}\theta_{CH_2CH_2}$
24	CH₂CH₂** <--> C₂H₄ (g) + 2-theta	$k_{24f}\theta_{CH_2CH_2} - k_{24r}P_{C_2H_4}\theta_*^2$
25	CH* + C* <--> CHC**	$k_{25f}\theta_{CH}\theta_C - k_{25r}\theta_{CHC}$
26	2-CH* <--> CHCH**	$k_{26f}\theta_{CH}^2 - k_{26r}\theta_{CHCH}$
27	CH₃C* + H* <--> CH₃CH* + theta	$k_{27f}\theta_{CH_3C}\theta_H - k_{27r}\theta_{CH_3CH}\theta_*$
28	CH₃CH* + H* <--> CH₃CH₂* + theta	$k_{28f}\theta_{CH_3CH}\theta_H - k_{28r}\theta_{CH_3CH_2}\theta_*$
29	CH₃CH₂* + H* <--> CH₃CH₃**	$k_{29f}\theta_{CH_3CH}\theta_H - k_{29r}\theta_{CH_3CH_3}$
30	CH₃CH₂* + 2-theta <--> CH₂CH₂** + H*	$k_{30f}\theta_{CH_3CH_2}\theta_*^2 - k_{30r}\theta_{CH_2CH_2}\theta_H$
31	CH₂C** + H* <--> CH₃C* + 2-theta	$k_{31f}\theta_{CH_2C}\theta_H - k_{31r}\theta_{CH_3C}\theta_*^2$
32	CH₂C** + H* <--> CH₂CH** + theta	$k_{32f}\theta_{CH_2C}\theta_H - k_{32r}\theta_{CH_2C}\theta_*$
33	CH₂CH** + H* <--> CH₂CH₂** + theta	$k_{33f}\theta_{CH_2CH}\theta_H - k_{33r}\theta_{CH_2CH_2}\theta_*$
34	CH₂CH** + H* <--> CH₃CH* + 2-theta	$k_{34f}\theta_{CH_2CH}\theta_H - k_{34r}\theta_{CH_3CH}\theta_*^2$
35	CHC** + H* <--> CH₂C** + theta	$k_{35f}\theta_{CHC}\theta_H - k_{35r}\theta_{CH_2C}\theta_*$
36	CHC** + H* <--> CHCH** + theta	$k_{36f}\theta_{CHC}\theta_H - k_{36r}\theta_{CH_2C}\theta_*$
37	CHCH** + H* <--> CH₂CH**	$k_{37f}\theta_{CHCH}\theta_H - k_{37r}\theta_{CH_2CH}$
38	CHCH** <--> C₂H₂ (g) + 2-theta	$k_{38f}\theta_{CHCH} - k_{38r}P_{C_2H_2}\theta_*^2$

A.2. Surface Species Reaction Rates

Overall rate equations for intermediate species on the surface in the microkinetic model. Each r_n term represents a reaction from the list in Appendix A.1 (n = Rxn #). Overall rates are in units of coverage per second.

$$\frac{d\theta_{CO}}{dt} = r_1 - r_2 - r_3 - r_8 - r_{10}$$

$$\frac{d\theta_H}{dt} = -r_3 + 2r_4 - r_5 - r_7 - r_{10} - r_{11} - r_{12} - r_{13} - r_{14} - r_{27} - r_{28} - r_{29} + r_{30} - r_{31} - r_{32} - r_{33} - r_{34} - r_{35} - r_{36} - r_{37}$$

$$\frac{d\theta_C}{dt} = r_2 + r_3 - r_{11} - r_{16} - r_{21} - r_{25}$$

$$\frac{d\theta_O}{dt} = r_2 - r_7 - r_8 + r_{10}$$

$$\frac{d\theta_{OH}}{dt} = r_3 - r_5 + r_7$$

$$\frac{d\theta_{H2O}}{dt} = r_5 - r_6$$

$$\frac{d\theta_{CO2}}{dt} = r_8 - r_9$$

$$\frac{d\theta_{CH}}{dt} = r_{10} + r_{11} - r_{12} - r_{17} - r_{22} - r_{25} - 2r_{26}$$

$$\frac{d\theta_{CH2}}{dt} = r_{12} - r_{13} - r_{18} - r_{21} - r_{22} - 2r_{23}$$

$$\frac{d\theta_{CH3}}{dt} = r_{13} - r_{14} - r_{16} - r_{17} - r_{18} - 2r_{19}$$

$$\frac{d\theta_{CH4}}{dt} = r_{15}$$

$$\frac{d\theta_{CH3C}}{dt} = r_{16} - r_{27} - r_{31}$$

$$\frac{d\theta_{CH3CH}}{dt} = r_{17} + r_{27} - r_{28} + r_{34}$$

$$\frac{d\theta_{CH3CH2}}{dt} = r_{18} + r_{28} - r_{29} - r_{30}$$

$$\frac{d\theta_{CH3CH3}}{dt} = r_{19} - r_{20} + r_{29}$$

$$\frac{d\theta_{CH2C}}{dt} = r_{21} - r_{31} - r_{32} + r_{35}$$

$$\frac{d\theta_{CH2CH}}{dt} = r_{22} + r_{32} - r_{33} - r_{34} + r_{37}$$

$$\frac{d\theta_{CH2CH2}}{dt} = r_{23} - r_{24} + r_{30} + r_{33}$$

$$\frac{d\theta_{CHC}}{dt} = r_{25} - r_{35} - r_{36}$$

$$\frac{d\theta_{CHCH}}{dt} = r_{26} + r_{36} - r_{37} - r_{38}$$

$$\frac{d\theta_{*}}{dt} = -r_{1} - r_{2} - 2r_{4} + r_{5} + r_{6} + r_{7} + 2r_{9} + r_{11} + r_{12} + r_{13} + 2r_{14} - r_{15} + r_{16} +$$
$$r_{17} + r_{18} + 2r_{20} + 2r_{24} + r_{27} + r_{28} - 2r_{30} + 2r_{31} + r_{32} + r_{33} + 2r_{34} + r_{35} + r_{36} + 2r_{38}$$

A.3. Gaseous Species Reaction Rates

Overall rate equations for gaseous species in the microkinetic model. Each r_n term represents a reaction from the list in Appendix A.1 (n = Rxn #). Other terms include gas hourly space velocity (τ), ideal gas constant (R), temperature (T), Avogadro's number (N_A), reactor volume (V_R), and partial pressure of reactant i ($P_{i,0}$) in and out (P_i)

$$\frac{dP_{CO}}{dt} = \frac{\tau}{RT}\left(P_{CO,0} - P_{CO}\right) + \frac{1}{N_A V_R}(-r_1)$$

$$\frac{dP_{H2}}{dt} = \frac{\tau}{RT}\left(P_{H2,0} - P_{H2}\right) + \frac{1}{N_A V_R}(-r_4)$$

$$\frac{dP_{CO2}}{dt} = \frac{\tau}{RT}\left(P_{CO2,0} - P_{CO2}\right) + \frac{1}{N_A V_R}(r_8)$$

$$\frac{dP_{H2O}}{dt} = \frac{\tau}{RT}\left(P_{H2O,0} - P_{H2O}\right) + \frac{1}{N_A V_R}(r_6)$$

$$\frac{dP_{CH4}}{dt} = \frac{\tau}{RT}\left(P_{CH4,0} - P_{CH4}\right) + \frac{1}{N_A V_R}(r_{14} - r_{15})$$

$$\frac{dP_{C2H6}}{dt} = \frac{\tau}{RT}\left(P_{C2H6,0} - P_{C2H6}\right) + \frac{1}{N_A V_R}(r_{20})$$

$$\frac{dP_{C2H4}}{dt} = \frac{\tau}{RT}\left(P_{C2H4,0} - P_{C2H4}\right) + \frac{1}{N_A V_R}(r_{24})$$

$$\frac{dP_{C2H2}}{dt} = \frac{\tau}{RT}\left(P_{C2H2,0} - P_{C2H2}\right) + \frac{1}{N_A V_R}(r_{38})$$

A.4. Degree of Rate Control Results at 229°C

Table 4.2. Degree of Rate Control results for C_2H_x, H_2O, CO_2, and CH_4 production sensitivity at 229°C. Highlighted values represent the rate-limiting reaction steps identified for the corresponding gaseous products. Values in the columns represent the magnitude of influence each reaction step has on the production rate of the products shown with value furthest from zero representing reaction steps with the most influence (negative or positive).

Reaction Step	$H_2O_{(g)}$	$CO_{2(g)}$	$CH_{4(g)}$	$C_2H_{2\text{-}6(g)}$
$CO_{(g)}$ + theta <--> CO*	-1.22×10^{-4}	-1.26×10^{-4}	1.27×10^{-4}	9.07×10^{-5}
CO* + theta <-> C* + O*	-2.75×10^{-6}	0.043	1.55×10^{-5}	3.13×10^{-5}
CO* + H* <--> C* + OH*	0.997	0.959	0.997	1.992
$H_{2(g)}$ + 2-theta <--> 2-H*	2.59×10^{-3}	-1.72×10^{-3}	2.62×10^{-3}	-1.71×10^{-3}
H* + OH* <--> H_2O* + theta	3.46×10^{-4}	-0.966	-3.82×10^{-7}	2.77×10^{-7}
H_2O* <--> $H_2O_{(g)}$ + theta	4.29×10^{-6}	-6.67×10^{-5}	2.28×10^{-6}	2.28×10^{-6}
O* + H* <--> OH* + theta	-3.63×10^{-4}	0.957	1.88×10^{-7}	-4.79×10^{-7}
CO* + O* <--> CO_2**	-1.53×10^{-5}	1.64×10^{-4}	2.77×10^{-8}	6.99×10^{-8}
CO_2** <--> $CO_{2(g)}$ + 2-theta	4.14×10^{-6}	1.35×10^{-4}	-9.99×10^{-8}	-6.72×10^{-8}
CO* + H* <--> CH* + O*	4.75×10^{-5}	1.06×10^{-4}	-2.34×10^{-8}	1.32×10^{-8}
C* + H* <--> CH* + theta	7.00×10^{-5}	-7.71×10^{-8}	-7.61×10^{-8}	-7.56×10^{-8}
CH* + H* <--> CH_2* + theta	-5.66×10^{-5}	1.88×10^{-4}	-7.97×10^{-6}	-1.897
CH_2* + H* <--> CH_3* + theta	-3.99×10^{-7}	-1.46×10^{-7}	-9.11×10^{-8}	-0.058
CH_3* + H* <--> $CH_{4(g)}$ + 2-theta	1.27×10^{-5}	-2.51×10^{-7}	-1.81×10^{-7}	-0.071
$CH_{4(g)}$ + theta <--> CH_4'	-5.26×10^{-6}	0	0	0
CH_3* + C* <--> CH_3C* + theta	-3.38×10^{-5}	-6.71×10^{-8}	-6.88×10^{-8}	-6.94×10^{-8}
CH_3* + CH* <--> CH_3CH* + theta	7.83×10^{-7}	-1.18×10^{-7}	-1.39×10^{-7}	0.024
CH_3* + CH_2* <--> CH_3CH_2* + theta	4.65×10^{-5}	-9.34×10^{-8}	-1.40×10^{-7}	0.047
2-CH_3* <--> CH_3CH_3**	1.59×10^{-6}	-8.28×10^{-8}	-7.94×10^{-8}	-1.93×10^{-3}
CH_3CH_3** <--> $C_2H_{6(g)}$ + 2-theta	1.57×10^{-4}	-1.25×10^{-7}	-1.27×10^{-7}	1.92×10^{-3}
CH_2* + C* <--> CH_2C**	-7.11×10^{-6}	-8.36×10^{-8}	-8.51×10^{-8}	-8.38×10^{-8}
CH_2* + CH* <--> CH_2CH**	-2.37×10^{-3}	3.58×10^{-8}	3.75×10^{-8}	7.37×10^{-5}
2-CH_2* <--> CH_2CH_2**	-1.12×10^{-4}	1.29×10^{-7}	-1.33×10^{-7}	5.41×10^{-3}
CH_2CH_2** <--> $C_2H_4(g)$ + 2-theta	1.01×10^{-5}	-8.94×10^{-8}	-8.56×10^{-8}	-8.92×10^{-8}
CH* + C* <--> CHC**	9.13×10^{-6}	-5.02×10^{-8}	-4.77×10^{-8}	-4.93×10^{-8}
2-CH* <--> CHCH**	1.40×10^{-6}	4.95×10^{-6}	4.01×10^{-6}	0.924
CH_3C* + H* <--> CH_3CH* + theta	7.31×10^{-5}	-1.69×10^{-7}	-1.69×10^{-7}	-1.69×10^{-7}
CH_3CH* + H* <--> CH_3CH_2* + theta	-5.28×10^{-6}	1.63×10^{-7}	1.60×10^{-7}	-1.63×10^{-7}
CH_3CH_2* + H* <--> CH_3CH_3**	4.25×10^{-5}	-1.26×10^{-7}	-1.29×10^{-7}	2.13×10^{-9}
CH_3CH_2* + 2-theta <--> CH_2CH_2** + H*	-1.97×10^{-3}	-1.18×10^{-7}	-1.15×10^{-7}	-1.19×10^{-7}
CH_2C** + H* <--> CH_3C* + 2-theta	-1.58×10^{-5}	-9.76×10^{-8}	-9.75×10^{-8}	-9.49×10^{-8}
CH_2C** + H* <--> CH_2CH** + theta	9.62×10^{-6}	-2.71×10^{-8}	-3.04×10^{-8}	-3.69×10^{-8}
CH_2CH** + H* <--> CH_2CH_2** + theta	-1.31×10^{-6}	-2.64×10^{-6}	-2.64×10^{-6}	-2.65×10^{-6}
CH_2CH** + H* <--> CH_3CH* + 2-theta	-7.71×10^{-6}	-2.74×10^{-6}	-2.74×10^{-6}	-2.75×10^{-6}
CHC** + H* <--> CH_2C** + theta	4.31×10^{-6}	-1.28×10^{-7}	-1.30×10^{-7}	-1.34×10^{-7}
CHC** + H* <--> CHCH** + theta	-4.63×10^{-5}	-1.04×10^{-7}	-1.00×10^{-7}	-9.88×10^{-8}
CHCH** + H* <--> CH_2CH**	1.89×10^{-5}	4.87×10^{-6}	4.87×10^{-6}	4.20×10^{-6}
CHCH** <--> $C_2H_{2(g)}$ + 2-theta	1.23×10^{-5}	-1.00×10^{-7}	-9.99×10^{-8}	6.06×10^{-7}
Sum	0.9978	0.9921	1	0.9656

A.5. CH* Adsorption Convergence Testing of Slab Models

Table 4.3. Table of k-points tested for each slab. Convergence was considered to be met when CH* adsorption differed by only 0.3 eV. The second k-point column shows the k-points used for rate-limiting reaction step testing

	k-points	CH* Ads (eV)	k-points	CH* Ads. (eV)	k-points	CH* Ads. (eV)
(001)	1x1x1	-5.9	3x3x1	-6.2	5x5x1	-6.2
(110)	1x1x1	-6.0	4x2x1	-6.6	8x4x1	-6.6
(100)A	1x1x1	-5.3	3x1x1	-5.7	7x3x1	-5.7
(100)B	1x1x1	-4.6	2x4x1	-5.6	3x8x1	-5.7
(111)A	1x1x1	-5.9	4x2x1	-6.4	6x4x1	-6.3
(111)B	1x1x1	-5.7	4x2x1	-6.1	6x4x1	-6.3
(101)A	1x1x1	-5.6	4x2x1	-6.0	7x3x1	-6.1
(101)B	1x1x1	-6.1	4x2x1	-6.4	6x3x1	-6.4

Table 4.4. Convergence testing results for the parameters shown (ENCUT, # atomic layers, # relaxed layers). The highlighted cells represent the parameters chosen for Co (001). All other slabs had similar parameters with

ENCUT	Tot. Energy (eV)	# Layers	CH* Ads. (eV)	Relaxed Layers	CH* Ads. (eV)
250	-253.9	4	-6.2	1	-6.0
350	-254.1	6	-6.2	2	-6.2
400	-253.7	8	-6.3	3	-6.3

A.6. Low-index Surface Facets
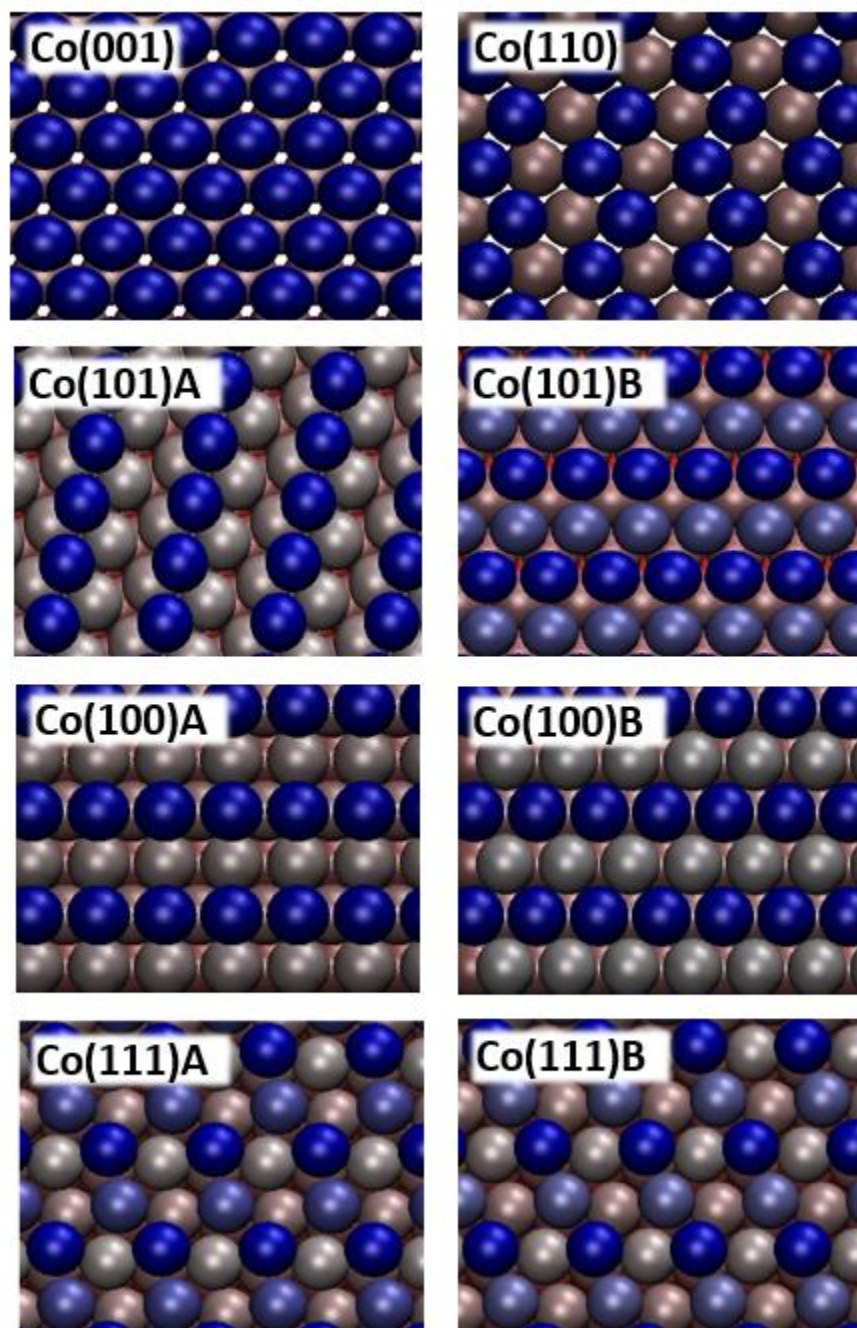
Figure 7.1. Eight low-index hcp surface facets. The atoms shown are most blue at the surface and change to a grey then to white color as they go further into the surface.

APPENDIX B.

B.1. Degree of Rate Control Results for CO_2 and CH_4 Production
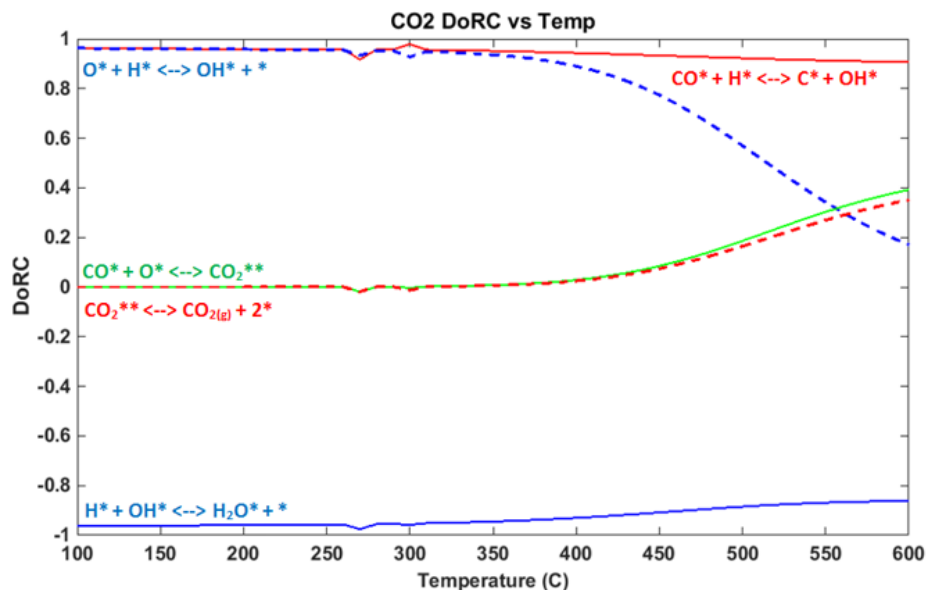
Figure 8.1. Degree of Rate Control Temperature analysis for CO_2 production. At lower temperatures ($< 400°C$) the rate-limiting reaction steps were found to hydrogen-assisted CO dissociation (enhances production), hydroxide formation (enhances production), and hydroxide hydrogenation to form water (hinders production).
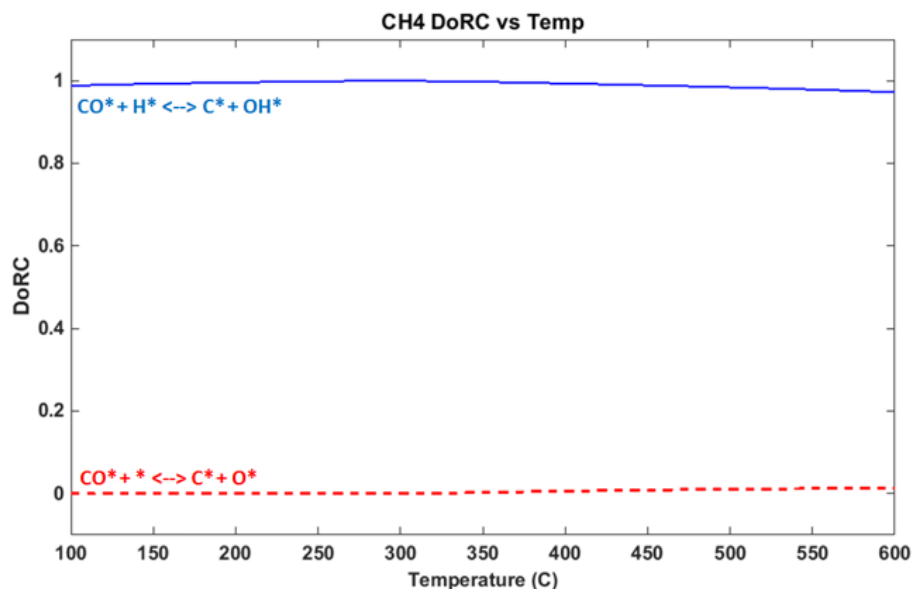
Figure 8.2. Degree of Rate Control Temperature analysis for CH_4 production. Only one rate-limiting reaction step was identified (hydrogen-assisted CO dissociation) that promotes CH_4 production.

B.2. Initial and Final States of CH* Coupling
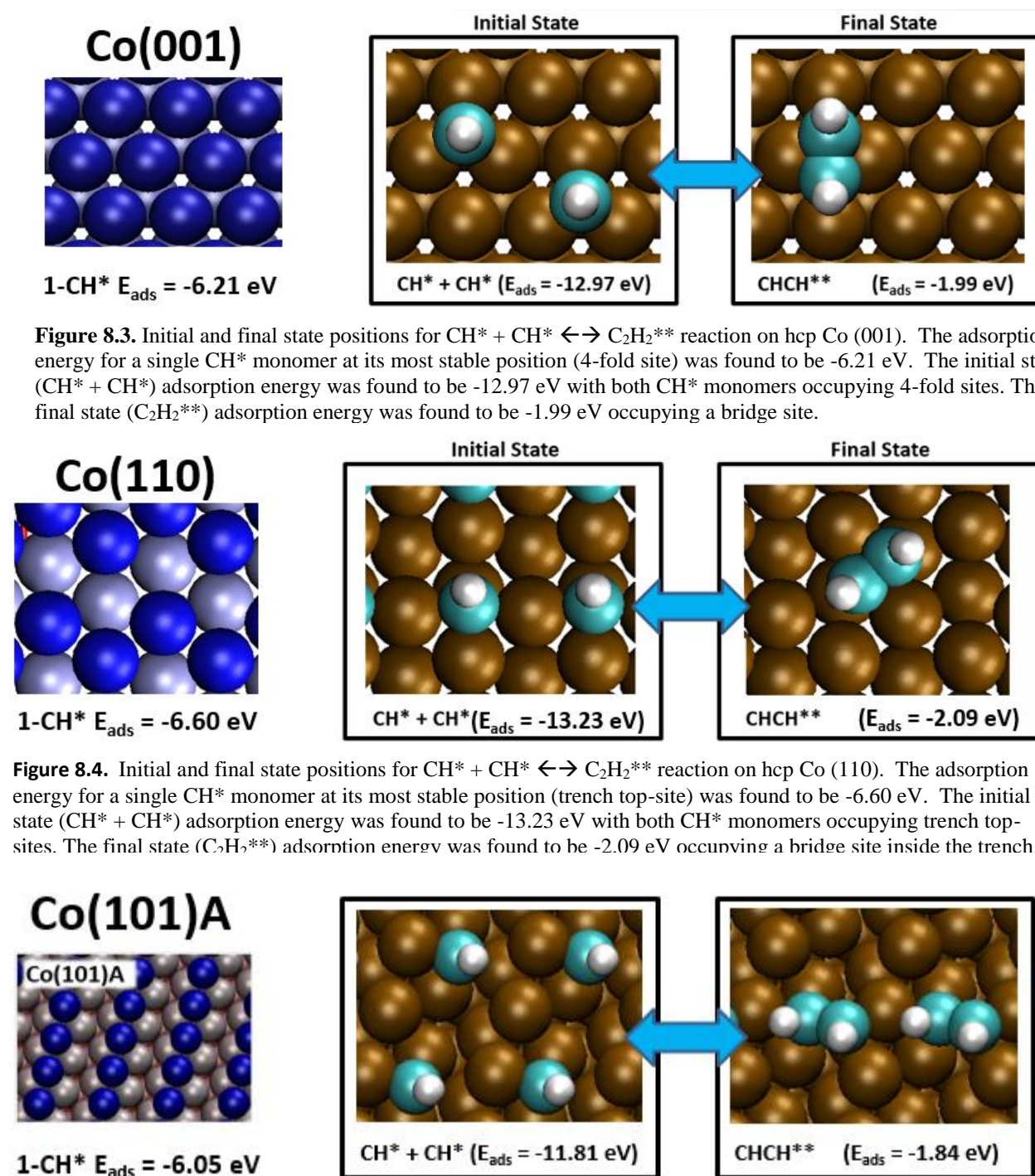
Figure 8.3. Initial and final state positions for CH* + CH* $\leftrightarrow$ C_2H_2** reaction on hcp Co (001). The adsorption energy for a single CH* monomer at its most stable position (4-fold site) was found to be -6.21 eV. The initial state (CH* + CH*) adsorption energy was found to be -12.97 eV with both CH* monomers occupying 4-fold sites. The final state (C_2H_2**) adsorption energy was found to be -1.99 eV occupying a bridge site.

Figure 8.4. Initial and final state positions for CH* + CH* $\leftrightarrow$ C_2H_2** reaction on hcp Co (110). The adsorption energy for a single CH* monomer at its most stable position (trench top-site) was found to be -6.60 eV. The initial state (CH* + CH*) adsorption energy was found to be -13.23 eV with both CH* monomers occupying trench top-sites. The final state (C_2H_2**) adsorption energy was found to be -2.09 eV occupying a bridge site inside the trench.

Figure 8.5. Initial and final state positions for CH* + CH* $\leftrightarrow$ C_2H_2** reaction on hcp Co (101)A. The adsorption energy for a single CH* monomer at its most stable position (trench bridge-site) was found to be -6.05 eV. The initial state (CH* + CH*) adsorption energy was found to be -11.81 eV with both CH* monomers occupying trench bridge-sites. The final state (C_2H_2**) adsorption energy was found to be -1.84 eV sitting perpendicular to the trench and slightly encroaching up the side of the wall.

Co(111)A

Co(111)A

1-CH* E$_{ads}$ = -6.33 eV

CH* + CH* (E$_{ads}$ = -12.75 eV)

CHCH** (E$_{ads}$ = -2.04 eV)
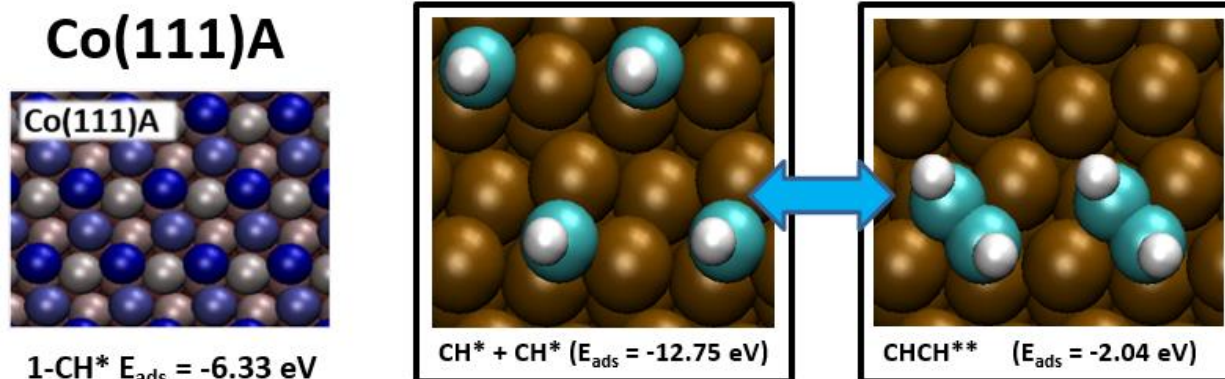
Figure 8.6. Initial and final state positions for CH* + CH* $\leftrightarrow$ C$_2$H$_2$** reaction on hcp Co (111)A. The adsorption energy for a single CH* monomer at its most stable position was found to be -6.33 eV. The initial state (CH* + CH*) adsorption energy was found to be -12.75 eV and the final state (C$_2$H$_2$**) adsorption energy was found to be -2.04 eV.

Co(101)B

Co(101)B

1-CH* E$_{ads}$ = -6.38 eV

CH* + CH* (E$_{ads}$ = -13.95 eV)

CHCH** (E$_{ads}$ = -2.55 eV)
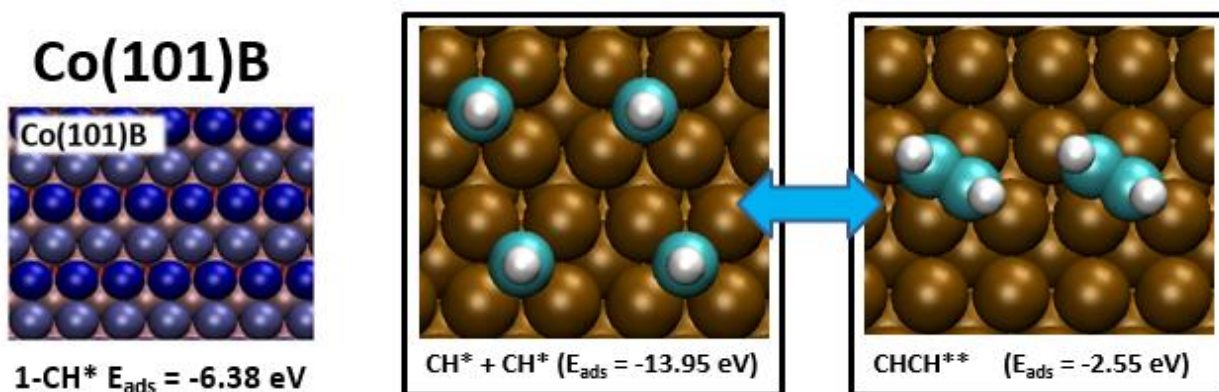
Figure 8.7. Initial and final state positions for CH* + CH* $\leftrightarrow$ C$_2$H$_2$** reaction on hcp Co (101)B. The adsorption energy for a single CH* monomer at its most stable position (trench bridge-site) was found to be -6.38 eV. The initial state (CH* + CH*) adsorption energy was found to be -13.95 eV with both CH* monomers occupying 5-fold sites. The final state (C$_2$H$_2$**) adsorption energy was found to be -2.55 eV occupying a 3-fold site.

Co(111)B

Co(111)B

1-CH* E$_{ads}$ = -6.34 eV

CH* + CH* (E$_{ads}$ = -12.86 eV)

CHCH** (E$_{ads}$ = -2.22 eV)
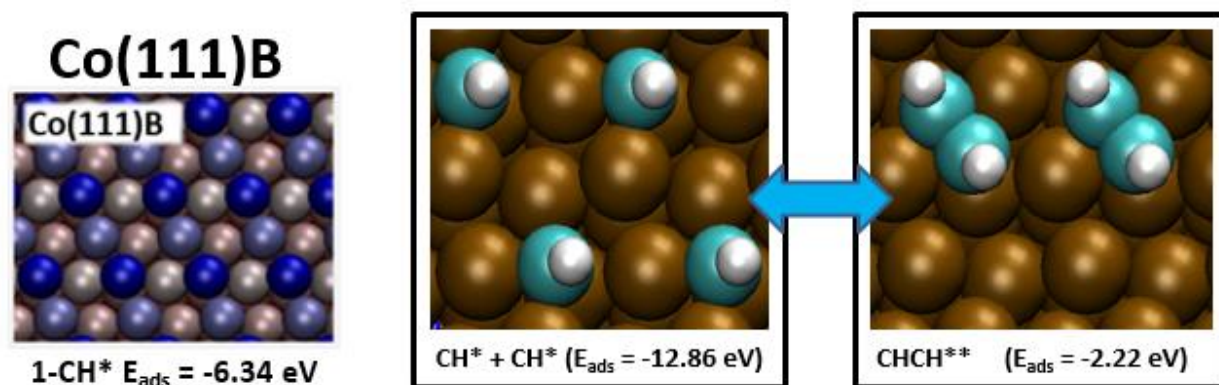
Figure 8.8. Initial and final state positions for CH* + CH* $\leftrightarrow$ C$_2$H$_2$** reaction on hcp Co (111)B. The adsorption energy for a single CH* monomer at its most stable position was found to be -6.34 eV. The initial state (CH* + CH*) adsorption energy was found to be -12.86 eV and the final state (C$_2$H$_2$**) adsorption energy was found to be -2.22 eV.

B.3. Initial and Final States of CH* Hydrogenation
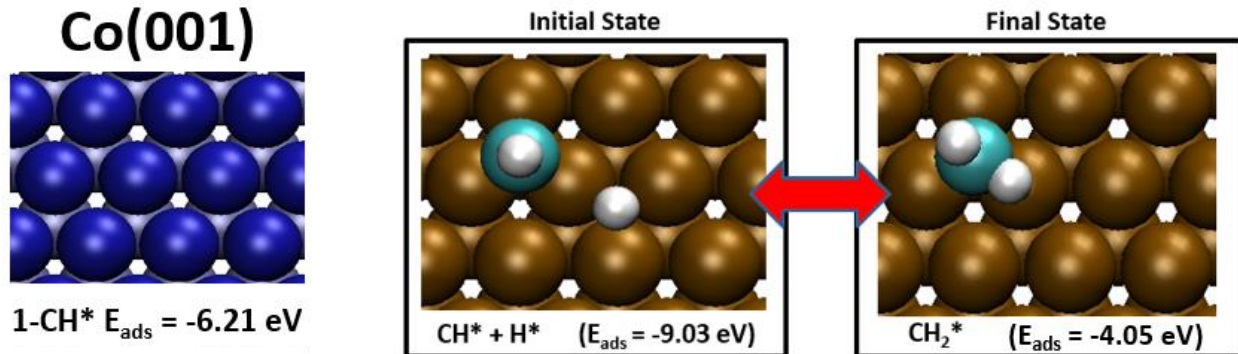
Figure 8.9. Initial and final state positions for CH* + H* $\longleftrightarrow$ CH$_2$* reaction on hcp Co (001). The initial state (CH* + H*) adsorption energy was found to be -9.03 eV with a CH* monomers occupying a 4-fold site and an H* monomer occupying a 3-fold site. The final state (CH$_2$*) adsorption energy was found to be -4.05 eV occupying a 4-fold site.
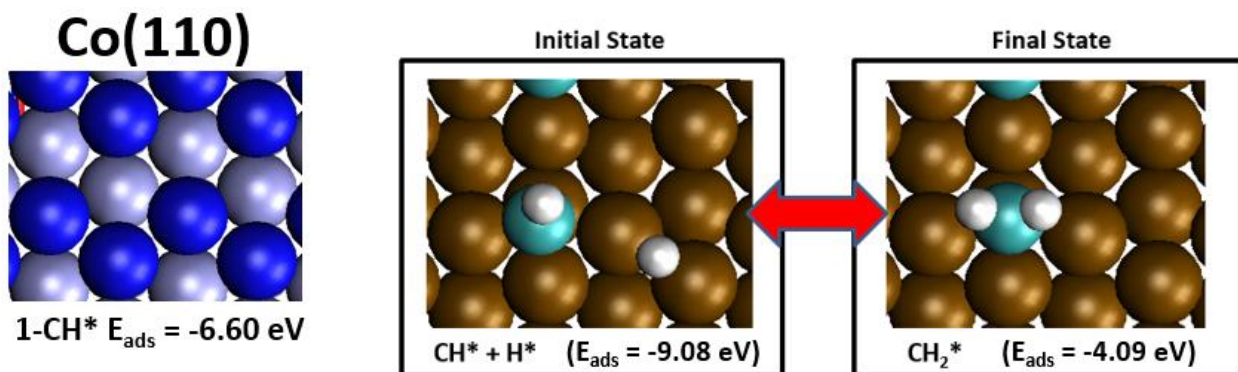
Figure 8.10. Initial and final state positions for CH* + H* $\longleftrightarrow$ CH$_2$* reaction on hcp Co (110). The initial state (CH* + H*) adsorption energy was found to be -9.08 eV with a CH* monomers occupying a trench top-site and an H* monomer occupying a wall bridge-site. The final state (CH$_2$*) adsorption energy was found to be -4.09 eV occupying a trench top-site.
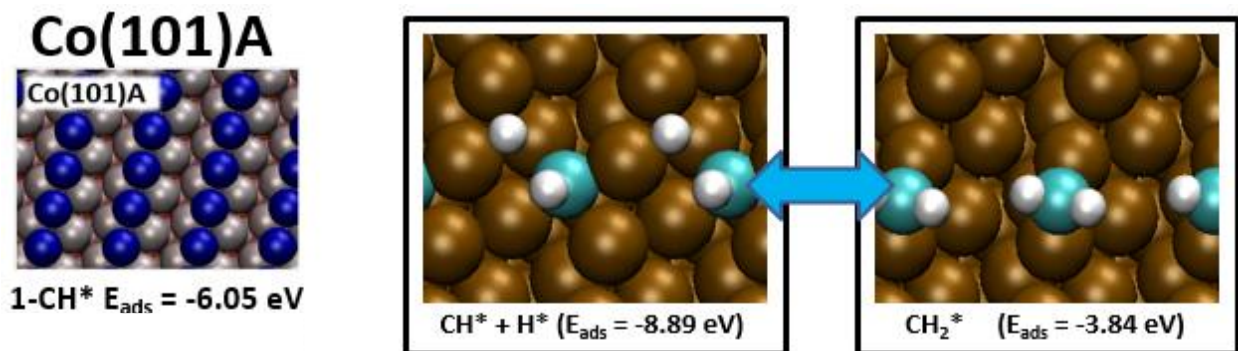
Figure 8.11. Initial and final state positions for CH* + H* $\longleftrightarrow$ CH$_2$* reaction on hcp Co (101)A.. The initial state (CH* + H*) adsorption energy was found to be -8.89 eV with a CH* monomers occupying a trench bridge-site and an H* monomer occupying an adjacent trench bridge-site. The final state (CH$_2$*) adsorption energy was found to be -3.84 eV occupying a wall bridge-site.
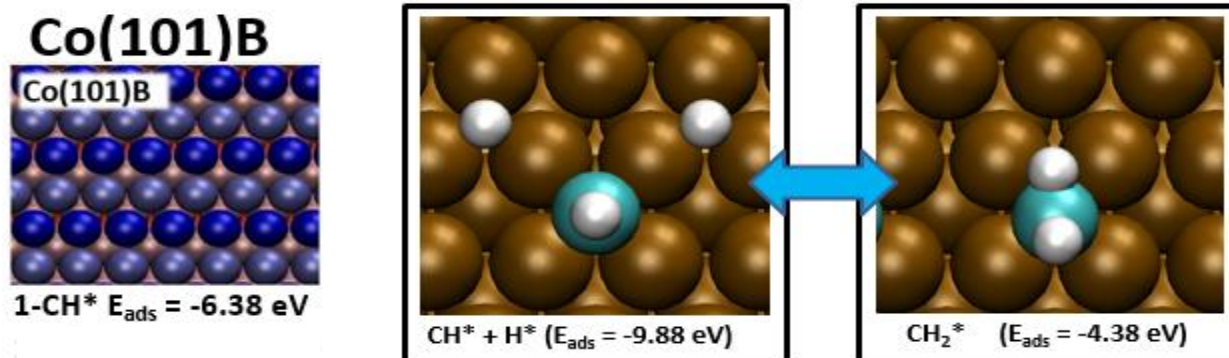
Figure 8.12. Initial and final state positions for CH* + H* ←→ CH$_2$* reaction on hcp Co (101)B. The initial state (CH* + H*) adsorption energy was found to be -9.88 eV with a CH* monomer occupying a 5-fold site and an H* monomer occupying a 3-fold site. The final state (CH$_2$*) adsorption energy was found to be -4.38 eV occupying a 5-fold site.
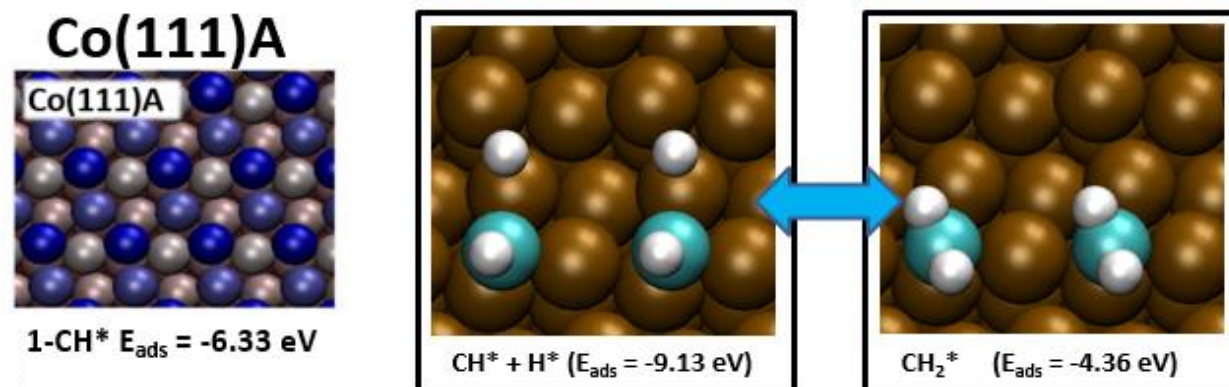
Figure 8.13. Initial and final state positions for CH* + H* ←→ CH$_2$* reaction on hcp Co (111)A. The initial state (CH* + H*) adsorption energy was found to be -9.13 eV with a CH* monomer occupying a trench top-site and an H* monomer occupying a wall bridge site. The final state (CH$_2$*) adsorption energy was found to be -4.36 eV occupying a trench top site.
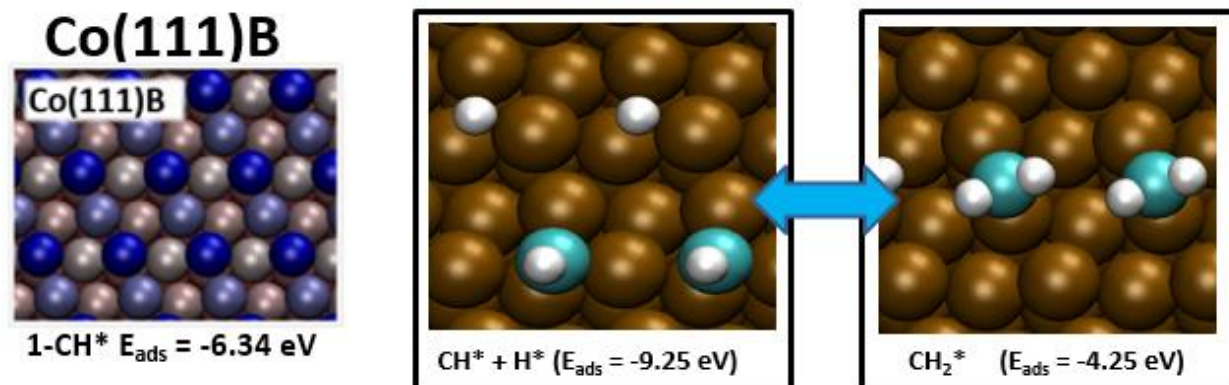
Figure 8.14. Initial and final state positions for CH* + H* ←→ CH$_2$* reaction on hcp Co (111)B. The initial state (CH* + H*) adsorption energy was found to be -9.25 eV with a CH* monomer occupying a trench top site and an H* monomer occupying the same type of site. The final state (CH$_2$*) adsorption energy was found to be -4.25 eV occupying a wall bridge site.

B.4. Calculated Adsorption Energies

Table 5.1. Adsorption energies for all adsorbates investigated in this study [eV]

Slab	CH*	H*	CH* + CH*	CH* + H*	CH$_2$*	C$_2$H$_2$**
(001)	-6.2	-2.8	-13.0	-9.0	-4.1	-2.0
(110)	-6.6	-2.4	-13.2	-9.1	-4.1	-2.1
(101)A	-6.1	-2.7	-11.8	-8.9	-3.8	-1.8
(101)B	-6.4	-3.4	-14.0	-9.9	-4.4	-2.6
(111)A	-6.3	-2.6	-12.8	-9.1	-4.4	-2.0
(111)B	-6.3	-2.8	-12.9	-9.3	-4.3	-2.2

B.5. Calculated Reaction Kinetics

Table 5.2. Formation activation barrier (Ea_f), decomposition activation barrier (Ea_d), and reaction energy (ΔE_r) for the CH* coupling and CH* hydrogenation reactions on the investigated slabs [eV].

Slab	CH* + CH* ←→ C$_2$H$_2$**			CH* + H* ←→ CH$_2$*		
	Ea$_f$	**Ea$_d$**	**ΔE$_r$**	**Ea$_f$**	**Ea$_d$**	**ΔE$_r$**
(001)	1.1	1.7	-0.6	0.3	0.2	-0.1
(110)	1.0	0.8	0.3	0.7	0.4	0.2
(101)B	1.3	0.7	0.5	1.0	0.2	0.8
(111)A	-	-	-	0.4	0.4	0.1

B.6. Activation Barrier Energy vs. Binding Energy
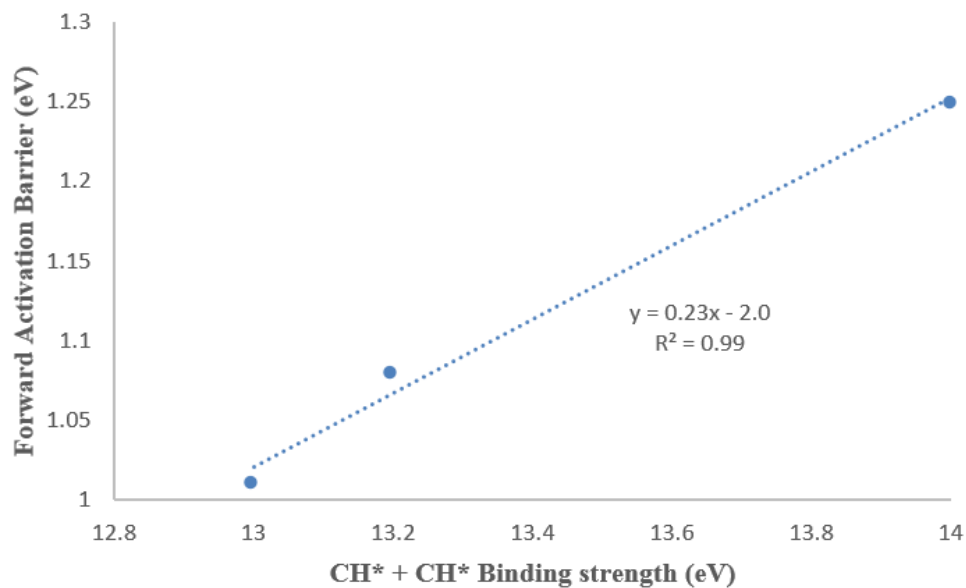
Figure 8.15. Graph of Formation Activation Barrier versus CH* + CH* binding energy

Appendix C. Temperature Swing Reactor Data

C.1. Microkinetic Model Details

Table 6.1. Reactor and model parameters fed into the microkinetic model for temperature swing investigation

Parameters		units
Reactor Inner Surface Area	130	cm^2
Reactor Volume	3.26	cm^3
Gas Hourly Space Velocity	28	hr^{-1}
H_2/CO Input Ratio	2	-
Total Input Pressure	20	bar
Temperature Swing	100 - 550	^{O}C
Active Site Density	10^{15}	sites/cm^2

C.2. List of Reactions for Temperature Swing Microkinetic Model

Table 6.2. List of reactions, Preexponential Factors, and Activation Energies used in the temperature swing reactor investigation. Reactions and kinetic data obtained from a study Kraft et al.[16]

Elementary step	Reaction	A_f	E_f	A_r	E_r
Adsorption–desorption					
1	$H_2 + 2^* \leftrightarrow 2\,H^*$	1.0×10^3	–	6.8×10^{12}	48.1
2	$CO + {}^* \leftrightarrow CO^*$	1.0×10^3	–	1.9×10^{16}	86.7
3	$C_2H_4 + 2^* \leftrightarrow C_2H_4^{**}$	1.3×10^7	32.2	1.0×10^{17}	155.0
4	$C_3H_6 + 2^* \leftrightarrow C_3H_6^{**}$	5.4×10^{10}	71.9	4.1×10^{13}	91.9
5–31	$C_nH_{2n} + 2^* \leftrightarrow C_nH_{2n}^{**}$	$3.7 \times 10^{17[b]}$	133.6	$1.9 \times 10^{13[c]}$	90.4
32	$H_2O + 2^* \leftrightarrow OH^* + H^*$	6.0×10^8	58.9	1.8×10^{13}	123.0
Monomer formation					
33	$CO^* + H^* \leftrightarrow HCO^* + {}^*$	8.4×10^{12}	128.1	1.9×10^{12}	54.1
34	$HCO^* + H^* \leftrightarrow HCOH^{**}$	6.1×10^{15}	84.3	8.1×10^8	121.8
35	$HCOH^{**} + 2^* \leftrightarrow CH^{***} + OH^*$	2.2×10^{13}	44.0	5.5×10^{10}	75.1
36	$CH^{***} + H^* \leftrightarrow CH_2^{**} + 2^*$	1.0×10^{13}	34.7	4.2×10^{10}	18.8
Chain growth					
37	$CH_2^{**} + CH_2^{**} \leftrightarrow C_2H_4^{**} + 2^*$	1.2×10^{14}	4.5	5.6×10^5	28.5
38	$C_2H_5^* + CH_2^{**} \leftrightarrow C_3H_7^* + 2^*$	3.0×10^{12}	39.5	1.5×10^{13}	107.0
39	$C_3H_7^* + CH_2^{**} \leftrightarrow C_4H_9^* + 2^*$	1.6×10^{14}	57.3	4.9×10^6	57.8
40–65	$C_nH_{2n+1}^* + CH_2^{**} \leftrightarrow C_{n+1}H_{2n+3}^* + 2^*$	$5.0 \times 10^{13[d]}$	53.1	6.8×10^{11}	163.0
Hydrogenation–H abstraction					
66	$CH_2^{**} + H^* \leftrightarrow CH_3^* + 2^*$	1.5×10^{14}	69.6	4.7×10^9	52.9
67	$C_2H_4^{**} + H^* \leftrightarrow C_2H_5^* + 2^*$	6.8×10^{16}	126.6	2.8×10^7	34.1
68	$C_3H_6^{**} + H^* \leftrightarrow C_3H_7^* + 2^*$	1.5×10^{13}	59.2	4.1×10^{10}	53.3
69–95	$C_nH_{2n}^{**} + H^* \leftrightarrow CnH_{2n+1}^* + 2^*$	1.1×10^{14}	66.8	1.9×10^{12}	68.2
96	$CH_3^* + H^* \rightarrow CH_4 + 2^*$	3.4×10^{17}	141.0		
97	$C_2H_5^* + H^* \rightarrow C_2H_6 + 2^*$	1.5×10^{14}	131.0		
98–125	$C_nH_{2n+1}^* + H^* \rightarrow C_nH_{2n+2} + 2^*$	1.1×10^{15}	138.8		
Water–gas shift					
126	$OH^* + OH^* \rightarrow H_2O + O^{**}$	9.3×10^{11}	135.3		
127	$CO^* + O^{**} \rightarrow CO_2 + 3^*$	8.7×10^8	18.2		
128	$H^* + O^{**} \rightarrow OH^* + 2^*$	2.2×10^{16}	86.2		

[a] The units of activation energies (E_f and E_r) and pre-exponential factors (A_f and A_r) are [kJmol^{-1}] and [Pa^{-n}s^{-1}], respectively; $n=1$ for A_f of adsorption reactions and 0 for A_f of all other reactions. [b] $A_{f,C4}$ in Equation (1) with $c=1.83$. [c] $A_{f,C4}$ in Equation (1) with $c=0.73$. [d] $A_{f,C4}$ in Equation (1) with $c=2.29$.

Appendix D.

D.1. Co FT Reactors from Literature

Table 7.1. Table showing reaction conditions, catalyst/support type, and reactor configuration for 18 different cobalt FT studies from the literature.

	catalyst	support	reactor type	GHSV [h^-1]	H2/CO	Pressure (bar)	Temp. (°C)	mass catalyst (g)	Ref.
1	12.7 wt% Co	SiO2	isothermal PBR with PF hydrodynamics	2016 - 21000	2	20	200	1.75	[75]
2	20 wt% Co, Co-B	Al2O3	fixed-bed microreactor	-	2	20	240	1	[76]
3	Co,CoPt	Al2O3	fixed-bed stainless steel reactor (9 mm i.d.)	12600	2	1	210	0.5	[77]
4	20 wt% Co	SiO2	fixed-bed reactor (I.D. = 12.7 mm)	21000	2	25	240	0.3	[13]
5	Co,CoPt	Al2O3	millifixed-bed stainless-steel tubular reactor (I.D. = 1.4 mm)	18304	2	20	220	0.5	[78]
6	Co	TiO2	16 reactor cat-alytic testing setup (Flowrence, Avantium).	-	2	20	220	0.1	[79]
7	25 wt% Co	Al2O3	1-L CSTR	5391	2.5	17.04	220	10	[80]
8	25 wt% Co	Al2O3	Plug Flow Fixed-Bed reactor	6300	2	82.4	220	3	[81]
9	25 wt% Co	Al2O3	1-L CSTR	2720	2	22	220	15	[61]
10	35 wt% Co	SBA-15 (SiO2)	fixed-bed reactor	-	2	1	190	-	[82]
11	Co	TiO2	fixed-bed reactor	2403	2	20	200	1	[83]
12	30 wt% Co	Cab-o-Sil Silica	fixed-bed reactor	-	2	1	190	-	[84]
13	15 wt% Co-(Cu,Ag,Au)	Al2O3	1-L CSTR (2 μm openning below liquid surface for wax removal)	3428	2	20.3	220	15	[85]
14	20 wt% Co	SiO2	semi-batch slurryphase reactor (V = 80 ml)	-	2	10	240	1	[86]
15	25 Co/Th/Mg	Al2O3, SiO2	fixed-bed microflow reactor (ID 9 mm) in downflow operation	1000	1	31	250	30	[87]
16	Co-Fe	SiO2	silicon-based microdevice (239 channels, 25 μm W, 100 μm D, 9 mm3 V	0.4 sccm	2	1	225	-	[88]
17	15 wt% Co	Al2O3	100 cm3 CSTR	11200	2	20	220	5	[89]
18	Co-Ca	TiO2	CSTR	5	2	10	230	2.5	[90]

D.2. Co FT Performance from Literature

Table 7.2. Table showing catalyst/support type and corresponding product selectivity (% wt. carbon), CO % conversion, CO_2 % carbon selectivity, and chain growth probability (α) for 13 different cobalt FT studies from the literature.

	catalyst	support	mass used (g)	CO % Conv.	C1 %	C(2-4)%	C(5-11)%	C(5+)%	CO2 (mol% of CO)	α	Ref.
1	12.7 wt% Co	SiO2	1.75	-	5.3	4.5	-	90.2	-	-	[75]
2	20 wt% Co 0.5 wt%B	Al2O3	1	93	-	-	-	-	-	0.71	[76]
3	CoPt	Al2O3	0.5	20.9	9.4	13.9	-	73.5	-	-	[77]
4	Co	SiO2	0.3	90	18	-	-	-	-	-	[13]
5	25 wt% Co	TiO2	0.1	-	7.8	-	-	86	-	-	[79]
6	25 wt% Co	Al2O3	10	20.0	12	-	-	40	-	-	[80]
7	25 wt% Co	Al2O3	3	42	10.5	-	-	88.8	4.2	0.88	[81]
8	25 wt% Co	Al2O3	15	49.4	7.9	-	-	83.4	0.45	-	[61]
9	35 wt% Co	SBA-15	-	4	13.3	-	-	71.8	-	0.79	[82]
10	15 wt% Co	Al2O3	15	47.76	8.9	-	-	80.6	0.82	-	[85]
11	15 wt% Co	Al2O3	5	50	11	10.3	-	78	0.2	0.88	[89]
12	Co-Ca	TiO2	2.5	74	4	-	-	89	-	-	[90]
13	10 wt% Co	SiO2	0.5	98	15	15	40	58	12	0.78	[91]

D.3. Fe FT Reactors from Literature

Table 7.3. Table showing reaction conditions, catalyst/support type, and reactor configuration for 17 different iron FT studies from the literature.

	catalyst	support	reactor type	GHSV [h^-1]	H2/CO	Press. (bar)	Temp. (°C)	mass cat. (g)	Ref.
1	100Fe		1L slurry-phase CSTR	1000	0.67	15	260	20	[92]
	100Fe	15Al2O3	1L slurry-phase CSTR	1000	0.67	15	260	20	
2	wFe-xZn-yK-zCu	SiO2	fixed-bed single pass flow tube(PFR hydro.)	1492	2	20	200	0.4	[33]
3	Fe	AC	fixed-bed down-flow	1681	0.9	20	260	1	[93]
4	Fe	graphene	steady flow reactor	1849	2	15	325	1	[94]
5	100 Fe	SiC	fixed-bed microreactor (165 mm L; 8.5 mm i.d.)	690	2	10	300	0.11	[95]
6	100 Fe	Al2O3	1 L slurry-phase CSTR	1000	0.67	15	290	20	[96]
7	Fe	Si	SS fixed-bed (i.d. 12 mm)	2000	2	15	260	3	[97]
8	Fe	SiO2	fixed-bed single pass flow tube (SS 316, 1 cm i.d)	2089	1	17	290	1.5	[98]
9	15% wt Fe	AC	fixed-bed	1839	0.9	20	310	1	[99]
10	Fe	Si,Al, Zn	PID MA10000 Micractivity Reactor	949	0.9	28	300	1	[100]
11	Fe	SiO2	239 Si channel microreactor (W: 25 μm Depth: 100 μm)	24 [mL/hr]	2	1	220	-	[88]
12	Fe	Al2O3	fixed-bed microreactor	60000	2	1	270	0.03	[101]
13	Fe	SiO2	fixed-bed microreactor (5 mm i.d.)	2000	1	31	250	5 mL	[87]
14	100Fe/5.6 4Cu/2La	SiO2	fixed-bed microreactor single-pass (S.S.316, 1.25 cm o.d. and 1 cm i.d.)	2089	1	17	290	1	[102]
15	Fe	Al2O3 - SiO2	fixed-bed microreactor	15000	1.5	1	250	0.2	[103]
16	Fe-Mn	Al2O3	SS fixed-bed microreactor (9 mm i.d.)	2700	1	15	340	1	[60]
17	Fe	SiO2	quartz microreactor (0.8 mm dia, 0.1 t, 100 mm L)	64.3 [mol/hr *g cat.]	2	1	250	0.2	[104]

D.4. Fe FT Performance from Literature

Table 7.4. Table showing catalyst/support type and corresponding product selectivity (% wt. carbon), CO % conversion, CO_2 % carbon selectivity, and chain growth probability (α) for 15 different iron FT studies from the literature.

	catalyst	support	mass used (g)	CO % Conv.	C1 %	C(2-4)%	C(5-11)%	C(5+)%	C(12+)%	CO2 (mol% of CO)	α	Ref.
1	100Fe		20	75.3	8.1	10.8	25.8	81.1	35.7	44.9		[92]
	100Fe	15% Al2O3	20	19	11.1	14.7	48.2	74.2	24.4	27.9		
2	Fe-Zn-K4-Cu2	SiO2	0.4	21	2	8.9		89.1		15.8		[33]
3	Fe	AC	1	29.4	18.4	51.1		30.6		30.1		[93]
4	Fe	graphene	1	51.5	1.5					2		[94]
5	100 Fe	SiC	0.11	74	15.9	62.3	19.5			24.7	0.6	[95]
6	100Fe/6.2 K/5.4Cu	14.4% Al2O3	20	91.4	4.5	5.4	23.2	90.2	26.4	43.8		[96]
7	Fe	Si	3	21.0	17.4	34.0		48.64		3.5		[97]
8	Fe/Cu	SiO2	1.5	44.2	12.4	18.9	13.8		8.2	38.2		[98]
	Fe/Cu/Ca	SiO2	1.5	74.2	5.6	8.6	11.6		16.4	45.3		
9	.15 wt Fe/.08Cu/ .09K	AC	1		7.2	39.6		51.6		48		[99]
10	Fe/Cu/K	Zn	1	33.7	8.5	26.3	18.5		13.9		0.9	[100]
11	Fe-Co	SiO2		62	3	97						[88]
12	100Fe/5.6 4Cu/2La	SiO2	1	64.1	16.6	35.2	29.4	48.2		36.3	0.7	[102]
13	0.06Fe	SiO2	0.2	54.1		57.5		20.7				[103]
14	Fe-Mn (50/50)	20% Al2O3	1	82.2	40.6	41.6		5.8				[60]
15	100Fe/0.3 Cu/0.8K (FB)	Al2O3		76.8	4.3	18.6	23.1		54			[105]
	100Fe/0.3 Cu/0.8K (SR)	Al2O4		30	6.2	15.6	14.5		63.7			

References

1.	J. Cheng, X. Q. Gong, P. Hu, C. M. Lok, P. Ellis and S. French, Journal of Catalysis **254** (2), 285-295 (2008).
2.	C. F. Huo, Y. W. Li, J. G. Wang and H. J. Jiao, Journal of Physical Chemistry C **112** (10), 3840-3848 (2008).
3.	D. C. D. P.L. Spath, 2003.
4.	L. Beans, edited by bakkenmap (ecowatch.com, ecowatch.com, 2014).
5.	J. Cheng, P. Hu, P. Ellis, S. French, G. Kelly and C. M. Lok, Journal of Catalysis **257** (1), 221-228 (2008).
6.	H. Schulz, Catalysis Today **214**, 140-151 (2013).
7.	M. C. Valero and P. Raybaud, Catalysis Letters **143** (1), 1-17 (2013).
8.	I. Lisiecki, M. Walls, D. Parker and M. P. Pileni, Langmuir **24** (8), 4295-4299 (2008).
9.	N. Fischer, E. van Steen and M. Claeys, Journal of Catalysis **299**, 67-80 (2013).
10.	R. A. van Santen, M. M. Ghouri, S. Shetty and E. M. H. Hensen, Catalysis Science & Technology **1** (6), 891-911 (2011).
11.	R. Salmon and A. Logan, (Ceres, 2013).
12.	H. Schulz, Applied Catalysis A: General **186** (1–2), 3-12 (1999).
13.	S. H. Kwack, M. J. Park, J. W. Bae, K. S. Ha and K. W. Jun, Reaction Kinetics Mechanisms and Catalysis **104** (2), 483-502 (2011).
14.	G. P. Van der Laan and A. Beenackers, Catalysis Reviews-Science and Engineering **41** (3-4), 255-318 (1999).
15.	S. Storsaeter, D. Chen and A. Holmen, Surface Science **600** (10), 2051-2063 (2006).
16.	P. Azadi, G. Brownbridge, I. Kemp, S. Mosbach, J. S. Dennis and M. Kraft, Chemcatchem **7** (1), 137-143 (2015).
17.	A. Y. Khodakov, B. Peregryn, A. S. Lermontov, J. S. Girardon and S. Pietrzyk, Catalysis Today **106** (1-4), 132-136 (2005).
18.	R. A. van Santen and A. J. Markvoort, Chemcatchem **5** (11), 3384-3397 (2013).
19.	M. Ojeda, R. Nabar, A. U. Nilekar, A. Ishikawa, M. Mavrikakis and E. Iglesia, Journal of Catalysis **272** (2), 287-297 (2010).
20.	O. R. Inderwildi, S. J. Jenkins and D. A. King, Journal of Physical Chemistry C **112** (5), 1305-1307 (2008).
21.	B. H. Davis, Catalysis Today **141** (1-2), 25-33 (2009).
22.	C.-F. Huo, Y.-W. Li, J. Wang and H. Jiao, Journal of Physical Chemistry C **112** (36), 14108-14116 (2008).
23.	J. Schweicher, A. Bundhoo and N. Kruse, Journal of the American Chemical Society **134** (39), 16135-16138 (2012).
24.	J. P. Perdew, K. Burke and M. Ernzerhof, in *Chemical Applications of Density-Functional Theory*, edited by B. B. Laird, R. B. Ross and T. Ziegler (Amer Chemical Soc, Washington, 1996), Vol. 629, pp. 453-462.
25.	N. S. Govender, F. G. Botes, M. H. J. M. de Croon and J. C. Schouten, Journal of Catalysis **312**, 98-107 (2014).
26.	R. A. van Santen, A. J. Markvoort, M. M. Ghouri, P. A. J. Hilbers and E. J. M. Hensen, Journal of Physical Chemistry C **117** (9), 4488-4504 (2013).
27.	M. K. Zhuo, K. F. Tan, A. Borgna and M. Saeys, Journal of Physical Chemistry C **113** (19), 8357-8365 (2009).
28.	R. C. Brady and R. Pettit, Journal of the American Chemical Society **103** (5), 1287-1289 (1981).
29.	F. Fischer, Tropsch, H., (Brennstoff-Chem, 1926), Vol. 7, pp. 97.

30.   M. A. Vannice, Journal of Catalysis **44** (1), 152-162 (1976).
31.   G. I. Lin, P. V. Samokhin, S. D. Kaloshkin and A. Y. Rozovskii, Kinet. Catal. **39** (4), 577-583 (1998).
32.   C. Zhang, G. Zhao, K. Liu, Y. Yang, H. Xiang and Y. Li, Journal of Molecular Catalysis a-Chemical **328** (1-2), 35-43 (2010).
33.   S. Z. Li, S. Krishnamoorthy, A. W. Li, G. D. Meitzner and E. Iglesia, Journal of Catalysis **206** (2), 202-217 (2002).
34.   G. Henriciolive and S. Olive, Angewandte Chemie-International Edition in English **15** (3), 136-141 (1976).
35.   T. J. Donnelly, I. C. Yates and C. N. Satterfield, Energy & Fuels **2** (6), 734-739 (1988).
36.   N. Fischer, B. Clapham, T. Feltes and M. Claeys, Acs Catalysis **5** (1), 113-121 (2015).
37.   Q. F. Ge and M. Neurock, Journal of Physical Chemistry B **110** (31), 15368-15380 (2006).
38.   J. X. Liu, H. Y. Su, D. P. Sun, B. Y. Zhang and W. X. Li, Journal of the American Chemical Society **135** (44), 16284-16287 (2013).
39.   R. A. B.W. Lee, A. Ignatiev, M. A. Van Hove, The American Physical Society **17** (4), 1510 - 1520 (1978).
40.   J. M. Zhang, D. D. Wang and K. W. Xu, Applied Surface Science **253** (4), 2018-2024 (2006).
41.   S.-L. Chin, A. Ionescu, R. M. Reeve, J. Cheng and C. H. W. Barnes, Surface Science **608**, 282-291 (2013).
42.   R. L. Toomes and D. A. King, Surface Science **349** (1), 1-18 (1996).
43.   E. Iglesia, Natural Gas Conversion Iv **107**, 153-162 (1997).
44.   W. Ma, G. Jacobs, D. E. Sparks, M. K. Gnanamani, V. R. R. Pendyala, C. H. Yen, J. L. S. Klettlinger, T. M. Tomsik and B. H. Davis, Fuel **90** (2), 756-765 (2011).
45.   P. a. K. Hohenburg, W., Phys. Rev. **136** (3B), 864-871 (1964).
46.   M. a. O. Born, R., Annalen der Phsik **389** (20), 457-484 (1927).
47.   W. a. S. Kohn, L. J., Phys. Rev. **140** (4A), 1133-1138 (1965).
48.   L. J. Sham, Philos. Trans. R. Soc. Lond. Ser. A-Math. Phys. Eng. Sci. **334** (1635), 481-490 (1991).
49.   J. P. Perdew, K. Burke and Y. Wang, Phys. Rev. B **54** (23), 16533-16539 (1996).
50.   J. P. Perdew and Y. Wang, Phys. Rev. B **45** (23), 13244-13249 (1992).
51.   Y. K. Zhang and W. T. Yang, Physical Review Letters **80** (4), 890-890 (1998).
52.   B. Hammer, L. B. Hansen and J. K. Norskov, Phys. Rev. B **59** (11), 7413-7421 (1999).
53.   G. Kresse and J. Furthmuller, Comput. Mater. Sci. **6** (1), 15-50 (1996).
54.   M. M. Georg Kresse, and Jurgen Furthmuller.
55.   G. Henkelman, B. P. Uberuaga and H. Jonsson, Journal of Chemical Physics **113** (22), 9901-9904 (2000).
56.   C. T. Campbell, Journal of Catalysis **204** (2), 520-524 (2001).
57.   W. J. M. v. W. Anna Granly Hansen, Per Stoltze, Topics in Catalysis **45** (1), 219-222 (2007).
58.   D. R. Alfonso, Journal of Physical Chemistry C **117** (40), 20562-20571 (2013).
59.   N. O. Elbashir and C. B. Roberts, Ind. Eng. Chem. Res. (44), 505-521 (2005).
60.   M. Feyzi, S. Vahid and A. Mirzaei, Advances in Physical Chemistry, 12 (2009).
61.   W. Ma, G. Jacobs, R. A. Keogh, D. B. Bukur and B. H. Davis, Applied Catalysis a-General **437**, 1-9 (2012).
62.   C. Stegelmann, A. Andreasen and C. T. Campbell, Journal of the American Chemical Society **131** (37), 13563-13563 (2009).
63.   K. F. Tan, J. Xu, J. Chang, A. Borgna and M. Saeys, Journal of Catalysis **274** (2), 121-129 (2010).
64.   X. Q. Gong, R. Raval and P. Hu, Journal of Chemical Physics **122** (2) (2005).
65.   X. Q. Gong, R. Raval and P. Hu, Surface Science **562** (1-3), 247-256 (2004).
66.   Y. Y. Qi, J. Yang, X. Z. Duan, Y. A. Zhu, D. Chen and A. Holmen, Catalysis Science & Technology **4** (10), 3534-3543 (2014).

67.   M. K. Zhuo, A. Borgna and M. Saeys, Journal of Catalysis **297**, 217-226 (2013).
68.   V. A. de la Pena O'Shea, S. Gonzalez, F. Illas and J. L. G. Fierro, Chemical Physics Letters **454** (4-6), 262-268 (2008).
69.   L. Joos, I. A. W. Filot, S. Cottenier, E. J. M. Hensen, M. Waroquier, V. Van Speybroeck and R. A. van Santen, Journal of Physical Chemistry C **118** (10), 5317-5327 (2014).
70.   D. J. Klinke and L. J. Broadbelt, Surface Science **429** (1-3), 169-177 (1999).
71.   S. Shetty, A. P. J. Jansen and R. A. van Santen, Journal of the American Chemical Society **131** (36), 12874-+ (2009).
72.   D. M. S. Curtarolo, W. Setyawan, R. Chepulskyy, G. Hart, O. Levy.
73.   C. Stegelmann, N. C. Schiodt, C. T. Campbell and P. Stoltze, Journal of Catalysis **221** (2), 630-649 (2004).
74.   T. E. Madey, W. H. Chen, H. Wang, P. Kaghazchi and T. Jacob, Chemical Society Reviews **37** (10), 2310-2327 (2008).
75.   S. Krishnamoorthy, M. Tu, M. P. Ojeda, D. Pinna and E. Iglesia, Journal of Catalysis **211** (2), 422-433 (2002).
76.   M. Saeys, K. F. Tan, J. Chang and A. Borgna, Industrial & Engineering Chemistry Research **49** (21), 11098-11100 (2010).
77.   W. Chu, P. A. Chernavskii, L. Gengembre, G. A. Pankina, P. Fongarland and A. Y. Khodakov, Journal of Catalysis **252** (2), 215-230 (2007).
78.   M. Sadeqzadeh, S. Chambrey, J. Hong, P. Fongarland, F. Luck, D. Curulla-Ferre, D. Schweich, J. Bousquet and A. Y. Khodakov, Industrial & Engineering Chemistry Research **53** (17), 6913-6922 (2014).
79.   T. O. Eschemann, J. H. Bitter and K. P. d. Jong, Catalysis Today **228**, 89-95 (2014).
80.   W. P. Ma, G. Jacobs, D. E. Sparks, R. L. Spicer, B. H. Davis, J. L. S. Klettlinger and C. H. Yen, Catalysis Today **228**, 158-166 (2014).
81.   G. Jacobs, K. Chaudhari, D. Sparks, Y. Q. Zhang, B. C. Shi, R. Spicer, T. K. Das, J. L. Li and B. H. Davis, Fuel **82** (10), 1251-1260 (2003).
82.   A. Y. Khodakov, R. Bechara and A. Griboval-Constant, Applied Catalysis a-General **254** (2), 273-288 (2003).
83.   Y. Yao, D. Hildebrandt, D. Glasser and X. Liu, Industrial & Engineering Chemistry Research **49** (21), 11061-11066 (2010).
84.   A. Y. Khodakov, J. S. Girardon, A. Griboval-Constant, A. S. Lermontov and P. A. Chernavskii, Natural Gas Conversion Vii **147**, 295-300 (2004).
85.   G. Jacobs, M. C. Ribeiro, W. Ma, Y. Ji, S. Khalid, P. T. A. Sumodjo and B. H. Davis, Applied Catalysis a-General **361** (1-2), 137-151 (2009).
86.   S. Sun, K. Fujimoto, Y. Zhang and N. Tsubaki, Catalysis Communications **4** (8), 361-364 (2003).
87.   M. F. M. Post, A. C. Vanthoog, J. K. Minderhoud and S. T. Sie, Aiche Journal **35** (7), 1107-1114 (1989).
88.   S. Zhao, V. S. Nagineni, N. V. Seetala and D. Kuila, Industrial & Engineering Chemistry Research **47** (5), 1684-1688 (2008).
89.   D. Pena, A. Griboval-Constant, C. Lancelot, M. Quijada, N. Visez, O. Stephan, V. Lecocq, F. Diehl and A. Y. Khodakov, Catalysis Today **228**, 65-76 (2014).
90.   K. Shimura, T. Miyazawa, T. Hanaoka and S. Hirata, Catalysis Today **232**, 2-10 (2014).
91.   S. Sartipi, H. Jansma, D. Bosma, B. Boshuizen, M. Makkee, J. Gascon and F. Kapteijn, Review of Scientific Instruments **84** (12), 11 (2013).
92.   H.-J. Wan, B.-S. Wu, C.-H. Zhang, H.-W. Xiang, Y.-W. Li, B.-F. Xu and F. Yi, Catalysis Communications **8** (10), 1538-1545 (2007).
93.   W. Ma, E. L. Kugler and D. B. Dadyburjor, Energy & Fuels **21** (4), 1832-1842 (2007).
94.   S. O. Moussa, L. S. Panchakarla, M. Q. Ho and M. S. El-Shall, Acs Catalysis **4** (2), 535-545 (2014).

95.   T. Herranz, S. Rojas, F. J. Perez-Alonso, M. Ojeda, P. Terreros and J. L. G. Fierro, Journal of Catalysis **243** (1), 199-211 (2006).
96.   H. Wan, B. Wu, H. Xiang and Y. Li, Acs Catalysis **2** (9), 1877-1883 (2012).
97.   J. Li, C. Zhang, X. Cheng, M. Qing, J. Xu, B. Wu, Y. Yang and Y. Li, Applied Catalysis a-General **464**, 10-19 (2013).
98.   A. N. Pour, S. M. K. Shahri, H. R. Bozorgzadeh, Y. Zamani, A. Tavasoli and M. A. Marvast, Applied Catalysis a-General **348** (2), 201-208 (2008).
99.   W. Ma, E. L. Kugler, J. Wright and D. B. Dadyburjor, Energy & Fuels **20** (6), 2299-2307 (2006).
100.   P. Sharma, T. Elder, L. H. Groom and J. J. Spivey, Topics in Catalysis **57** (6-9), 526-537 (2014).
101.   S. Ali, N. A. M. Zabidi and D. Subbarao, Chemistry Central Journal **5** (2011).
102.   A. N. Pour, M. R. Housaindokht, S. F. Tayyari and J. Zarkesh, Journal of Natural Gas Chemistry **19** (3), 284-292 (2010).
103.   T. Sara Faiz Hanna, N. A. M. Zabidi and D. Subbarao, Journal of Materials Science and Engineering **A1**, 9-15 (2011).
104.   S. Z. Li, G. D. Meitzner and E. Iglesia, Journal of Physical Chemistry B **105** (24), 5743-5750 (2001).
105.   D. B. Bukur, L. Nowicki and X. S. Lang, Catalysis Today **24** (1-2), 111-119 (1995).